DOE/ER/75789-2

Laser Enhanced Microwave Plasma Isotope Separation

Final Report

for Period September 30, 1992 - September 29, 1995

M. L. Brake and R. M. Gilgenbach

The University of Michigan
Dept. of Nuclear Engin. & Radiological Sciences
Ann Arbor, MI 48109-2104

June 1996

Prepared for

THE U.S. DEPARTMENT OF ENERGY
AGREEMENT NO. DE-FG02-92ER75789

DISCLAIMER

NOTICE

ABSTRACT

We examined an innovative method of isotope enrichment using laser enhanced microwave/electron cyclotron resonance (ECR) discharges. The experimental research was to focus on laser excitation of a low abundance isotope and then ionize and separate the isotope of low abundance using a microwave/ECR discharge at 2.45 GHz. A small compact electron cyclotron resonance ion source, which uses permanent magnets, was constructed during this project. The dye laser was purchased and later an excimer laser had to also be purchased because it turned out that the dye laser could not be pumped by our copper laser. It was intended that the dye laser be tuned to a wavelength of 670.8 nm, which would excite ^{6}Li which would then be preferentially ionized by the ECR source and collected with a charged grid. The degree of enrichment was to be determined using thermal ionization mass spectrometry. The final objective of this project was to assess the feasibility of this system to large-scale production of stable isotopes. However the funding of this project was interrupted and we were not able to achieve all of our goals.

DESCRIPTION OF PROGRESS

Our research plan (as described in the original research proposal) was broken up into three years. During the first year we had planned on modifying an existing microwave resonant cavity by adding rare earth magnets to provide an electron cyclotron resonance region as well as add a processing vacuum chamber. Instead, we decided to build a completely new ion source which will be described below.

The design of the ion source which we built to ionize samples of lithium is based upon a device of L. Mahoney and J. Asmussen.[1] The microwave cavity is designed to excited various electromagnetic modes at 2.45 GHz depending upon the length of the cavity and the position of the co-axial probe which couples the microwaves from the source to the cavity. The microwave resonance cavity ion source can produce vaporization, heating and ionization of lithium samples.

The advantages of the Mahoney source includes:

- smaller plasma volume - this means that the laser excitation volume to overall plasma volume will be much larger than in the previous system. This will improve the total efficiency of the system.

- this source is based upon an 8 inch conflat vacuum flange, making it very compatible with conventional vacuum systems. This is important for future adaptability of this system to a production setting.

- this ion source has a long working lifetime, requires little maintenance and produces high beam current densities (5 - 10 mA/cm^2). [1]

Our major modification has been to move the gear assembly which controls the sliding short to an off axis position. The means that two gears and a ball

---

[1] L. Mahoney and J. Asmussen, "A compact, resonant cavity, five centimeter, multicusp, ECR broad-beam ion source, Rev. Sci. Instrum. 61(1), January 1990, p. 285.

bearing assembly are now required instead of the one gear. This allowed for a hole to be drilled in the center of the sliding short and end wall of the cavity. We decided to shine the laser down the center axis of the cavity rather than at an oblique angle from below (as described in the original proposal). See Figure 1 for a schematic of the isotope enrichment system. The ion source was attached to the side of the vacuum chamber so that the abundant or dominant isotope and the buffer gas would exit the system via the vacuum pumps rather than onto the collection grid.

We assembled the vacuum chamber, pumps and vacuum components. We were able to obtain lithium plasmas, in a rare gas background, from lithium (either LiCl or Li_2Cl_3). Several experiments were performed on the lithium source and samples were taken from the collection grid. The Radiogenic Isotope Geochemistry Laboratory in the Geological Sciences Department was not able to calibrate their mass spectrometer for lithium, so we were left without a method to determine separation. Basic studies of the lithium source were the basis of two publications and the thesis of Cynthia Brooks (see attached).

We had planned to excite the lithium samples with a copper vapor pumped dye laser. The laser company was not able to get the needed wavelength out of the dye laser when pumped by the green laser. So we were forced into purchasing a XeCl laser which does pump the dye laser well. Unfortunately the laser company was very slow about resolving the problem and since the project was terminated early, we were not able to test out the laser system in conjunction with the lithium plasma.

The major accomplishments of this projects can be summarized as follows:

- We modified a permanent magnetic ECR ion source for suitability of lithium vaporization.
- We demonstrated that lithium could be vaporized from its solid state.

- We determined the operating conditions to maximize production of Li atoms (see attached publications).
- We collected many samples of lithium from the collection grid. Unfortunately the Geology Dept. was not able to give us any feedback on these samples.
- There were three students supported by this project; two graduate students and one undergraduate.
- Patent Disclosure forms were submitted June 3, 1994 with the UM Office of Technology Management. My understanding is that these papers have been closed out as we were not able to demonstrate our objective.
- The archival journal articles that resulted from this project (and are attached):
  "Two-Dimensional Imaging of Optical Emission in a Multicusp-ECR Microwave Resonant Cavity" by C. Brooks and M. Brake, IEEE Trans. on Plasma Sci. Vol. 24, No. 1., 8, Feb. 1996
  "Lithium-Argon Discharges in a Multicusp-ECR Microwave Resonant Cavity" by C. Brooks and M. Brake, IEEE Trans. on Plasma Sci., Vol. 23, No. 6., 1023, Dec. 1995.
- Cynthia Brooks wrote a Ph.D. dissertation describing the detailed discoveries of this project. The title is "An Electron Cyclotron Resonant, Microwave Resonant Cavity Lithium Plasma Source", attached.

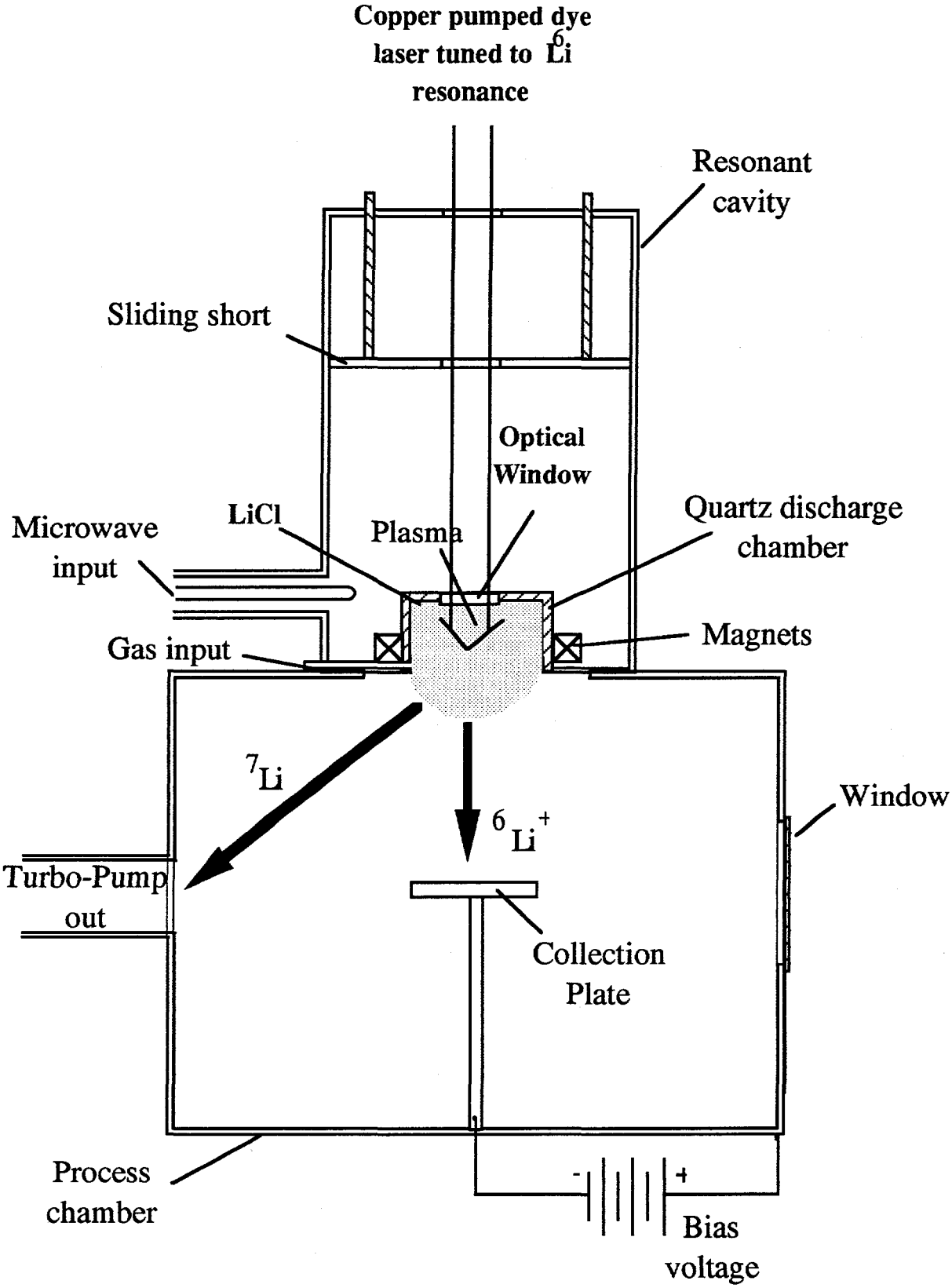

Figure 1. Schematic of the laser/ECR plasma isotope separation

ABSTRACT

AN ELECTRON CYCLOTRON RESONANT, MICROWAVE RESONANT CAVITY LITHIUM PLASMA SOURCE

by

Cynthia Bush Brooks

Chair: Associate Professor Mary L. Brake

A unique lithium plasma source featuring a microwave resonant cavity with an electron cyclotron resonant region has been constructed for use in laser-enhanced isotope separation experiments. Lithium-argon discharges have been created in the plasma source and properties of those discharges have been extensively studied. The discharge is maintained within a quartz cup at the base of a microwave resonant cavity operating at 2.45 GHz. The electron cyclotron resonant region is created by eight SmCo rare-earth magnets arranged in a multicusp configuration. Lithium is introduced to the system in the form of lithium chloride, a solid placed directly in the discharge region, which is then heated by a background argon discharge allowing dissociation of lithium. The dissociation is evidenced by the observation of strong Li-I lines in the discharge using optical emission spectroscopy. This unique method of creating a lithium plasma has the advantage of greater control of contaminants and longer source lifetime because the device does not contain an electrode. Additionally, the discharge can be maintained at pressures as low as 1 mTorr and input microwave powers of 100 Watts.

A number of diagnostics have been used to characterize the discharge. Double Langmuir probe studies indicate ion densities of 10^{10}-10^{11} cm^{-3} and electron temperatures of about 3 eV with operating pressures of 4-20 mTorr and input powers of 100-250 Watts. Optical emission spectroscopy indicates that the lithium concentration increases with decreasing argon flow and partial pressure. Single Langmuir probe measurements of the electron energy distribution function indicate that the electrons have a Druyvesteyn distribution at low operating pressures. Plasma density was found to decrease exponentially with downstream distance from the source. Peak saturation current densities of 1.2 mA/cm^2 were measured with a 7.5 cm diameter, negatively-biased, aluminum collector. A two-dimensional CCD array has been used to image the ECR region, providing a real-time diagnostic of the plasma emission within a wavelength region defined by low-bandpass filters. This newly-developed technique has been used for electromagnetic and uniformity of heating studies of the device.

AN ELECTRON CYCLOTRON RESONANT, MICROWAVE RESONANT CAVITY LITHIUM PLASMA SOURCE

by

Cynthia Bush Brooks

A dissertation submitted in partial fulfillment
of the requirements for the degree of
Doctor of Philosophy
(Nuclear Engineering)
in The University of Michigan
1995

Doctoral Committee:

Associate Professor Mary L. Brake, Chair
Professor Ward Getty
Professor Ronald Gilgenbach
Professor Y.Y. Lau

For Elizabeth and Madeleine,

my sunshine

ACKNOWLEDGMENTS

Financial support for this project was provided by the Department of Energy grant number # DE-FG02-92ER75789. The CCD camera was borrowed from the Solid State Electronics Lab at the University of Michigan. I also wish to acknowledge the fiscal support of an NSF-Graduate Engineering Education fellowship early in my career and a Rackham Predoctoral Fellowship for the final year of my studies.

Professor Mary Brake has been a vital source of support throughout my graduate career at the University of Michigan, providing technical as well as personal advice. For her assistance I am most grateful. Many thanks to Will McColl for his patient and detailed answers to my many questions. I particularly want to thank Melisa Buie, who has always been the best mentor and friend a person could ever hope to have.

Finally, I thank my family. I have been blessed with parents, Georgia and Jerry Bush, who never once doubted that I could achieve anything I set out to do. I am so very grateful for their constant faith and support. I thank my wonderful children, Elizabeth and Madeleine, for tolerating a cranky and often-distracted mother who has been a student their entire lives. Finally, I thank my husband, Donnie, for lemon-filled doughnuts, beer, never letting me quit and keeping me halfway sane.

TABLE OF CONTENTS

LIST OF FIGURES

Figure

LIST OF TABLES

Table

LIST OF APPENDICES

Appendix

CHAPTER 1

INTRODUCTION

1.1 Motivation

Isotope separation has many applications in basic research, industry and medicine. Traditional methods of producing isotopes are generally large-scale, inefficient or highly energy-intensive. The method commonly used in the past for large-scale isotope separation has been gaseous diffusion, a method which provided a very low enrichment ratio and required many steps to complete. Electromagnetic separation techniques such as the calutron provide larger enrichment ratios but are very energy-intensive and can process only a small amount of material. There is a need for smaller-scale, efficient isotope separation schemes so that isotopes can be produced on-site in an affordable manner. The plasma apparatus designed and tested in this work is part of a proposed small-scale, efficient isotope separation scheme.

The separation of Li-6 and Li-7 (which has a naturally occuring isotopic ratio of 7.4:92.6) has been chosen for preliminary studies for a number of reasons. Figure 1.1 is an energy level diagram for lithium illustrating the specific excitation to be employed.[Bri86] As seen in the diagram, the transition from the ground to the $2P\ ^2P$ is easily accessible with visible laser radiation such as that produced by a tunable dye laser. Fine structure splitting from the difference in nuclear mass of the two isotopes provides the means to selectively excite a particular species. For example, if it is desired

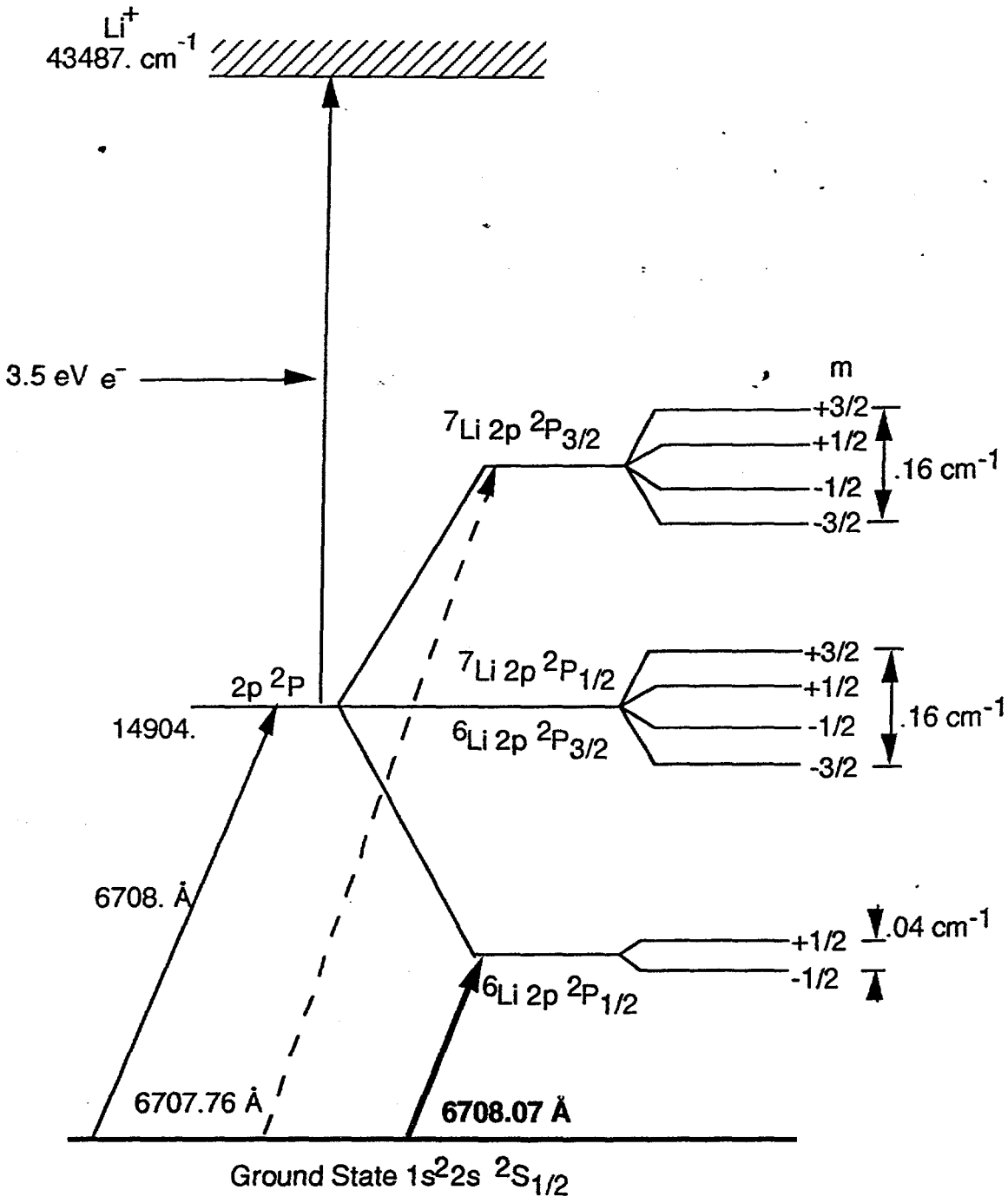

Figure 1.1. Energy level diagram of lithium featuring accessible visible transition to be used in laser isotope separation scheme.

to enrich Li-6, laser radiation at 6708.07 Å is chosen to excite Li-6 into a higher energy state. Once excited, electron collisions ionize the excited species.

In preparation for the isotopic enrichment studies, a lithium plasma source was designed and constructed. Scalability of plasma parameters with input power, gas pressure and flow rate, and lithium concentration must be fully understood prior to development of this apparatus as part of an isotope separation scheme. In addition to the use of well-established plasma diagnostic tools such as single and double Langmuir probes and optical emission spectroscopy, a new technique utilizing a CCD camera was developed to study two-dimensional plasma emission uniformity in the ECR region. The construction and development of this new lithium ion source as well as its measured operating parameters are presented in this dissertation.

1.2 Review of microwave plasma sources

Microwave plasma sources in general, and resonant cavity sources in particular, have a variety of industrial and research applications. Microwave sources have been used for materials processing[Hop90], as ion sources[Mah89,Jia94], as a pump source for lasers[Mou85] and in high-intensity lighting[But95], to name only a few applications. The increase in confinement provided by the addition of an electron cyclotron resonant (ECR) region allows the operation of the source at low pressures which results in a discharge for which electrons are in a collisionless regime.[Moi92] Lowering the discharge pressure is advantageous for laser isotope separation to reduce charge exchange losses from collisions between ions and neutrals of different species.[Gro91] An additional feature of microwave sources is that they are

electrodeless, allowing for a longer source lifetime even in the presence of reactive gases.[Off91]

Plasma isotope separation schemes of lithium and other medium-weight materials have also been proposed by a number of authors, most of whom suggest the use of a dc discharge.[Gro91,Atu93,Xiw92,Suz94] None of these suggest the use of radio frequency or microwave discharges in their isotope separation schemes.

In addition to isotope separation, lithium plasma sources also have a variety of applications in nuclear fusion research. As a source of ions or neutrals for beams, they are utilized in diagnostics and fueling of magnetic confinement fusion.[Fie92,Wad92,Wut94,Zha94] High purity lithium-ion beams are used as a driver for inertial confinement fusion.[Str93] The lithium plasma source presented in this dissertation is unique in that a lithium-containing solid is placed directly in the discharge chamber and a background inert-gas plasma is used to heat the solid and dissociate the lithium. Other lithium ion sources have used a separate oven to heat lithium to a vapor state[Fie92, Wad92, Wut94] or passed a current through a lithium-containing solid.[Zha94] The method presented here has the advantages of simplicity and low contamination of unwanted species.

1.3 Laser-enhanced plasma isotope enrichment

In the past 15 to 20 years, many plasma-based methods for isotope separation have been proposed and studied which overcome some of the drawbacks of traditional isotope separation schemes.[Gro91] The method proposed here will be a unique combination of laser isotope separation used in conjunction with an ECR microwave resonant cavity plasma source. Laser isotope separation is based upon using laser radiation chosen at a particular

wavelength to selectively excite a particular isotope to a higher state while not affecting the unwanted isotopes. The excited species is then preferentially ionized, either through continued excitation with a second tuned laser beam or through collisions with free electrons in a plasma. Figure 1.2 contains a schematic of the proposed separation scheme utilizing the lithium plasma source discussed in this work.

Some limitations and difficulties are encountered with this method. Charge exchange reactions between the desired ionized species and neutral species in the plasma can greatly reduce the efficiency of the method.[Ari82] This problem can be reduced by keeping the collisional mean free path small in comparison to the size of the discharge chamber[Kar82], a condition which can be successfully achieved in the plasma source presented in this work. Several extraction methods for the ionized lithium have been proposed and tested by Arisawa, et al.[Ari82] They found electrostatic extraction with a biased electrode in a laser-excited dc discharge to be partially successful, but this method has limited efficiency because of positive sheath formation at the electrode. Arisawa and others[Haz80] recommend a crossed electrostatic and magnetic field, with the field strength and electrode spacing chosen in relation to the ion cyclotron radius of the desired species. Note that there have not been any published accounts of examining laser enhanced plasma isotope separation using an electrodeless discharge such as a microwave cavity.

1.4 Theoretical estimate of separation ratio

A rough estimate of the isotope enrichment expected from this scheme can be made based upon a statistical calculation. A number of assumptions are made in this calculation. First is that the electrons are in a Maxwellian distribution. This is unlikely to be true for the discharge under consideration,

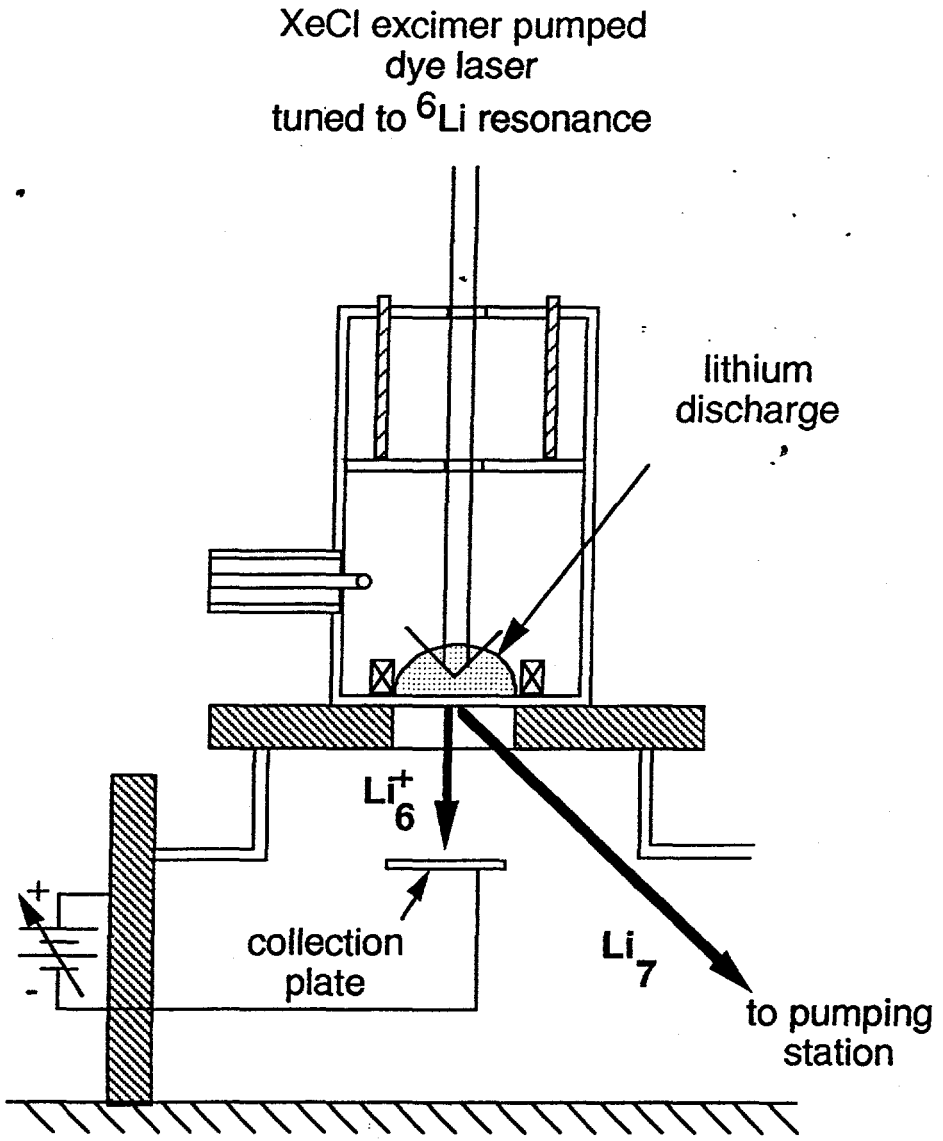

Figure 1.2. Experimental configuration of the laser-enhanced microwave plasma isotope separation technique.

but a similar analysis could be made given any measured distribution function. The ionization fraction of the discharge is assumed small, so that the ionization percentage of different isotopes is roughly the same. This

assumption is easily met in microwave discharges, which have an ionization fraction of a few tenths of a percent. A low plasma density is assumed such that the ratio of ionization of different isotopes is equal to the collected ratio. The truth of this assumption would depend heavily on the collection scheme involved. Finally, it is assumed that all collisions result in the electrons slowing to energies below the ionization potential of either isotope, a safe assumption in a low temperature plasma.

Consider a discharge for which the plasma has a Maxwellian electron density distribution as a function of energy E given by

$$n_e(E) = \frac{N}{k_B T_e} e^{-E/k_B T_e}, \tag{1.1}$$

where k_B is Boltzmann's constant, T_e is the electron temperature and N is the total number of electrons. Then the number of electrons with energy above the ionization potential E_i of a particular isotope i is given by

$$n_e(>E_i) = \int_{E_i}^{\infty} n_e(E)\, dE = N e^{-E_i/k_B T_e} \tag{1.2}$$

Assume that the material in question has only two isotopic species, A and B, whose fractional abundance's are given by N_A and N_B. The density of ions of isotopes A and B (n_{A+},n_{B+}) are given by

$$n_{A+} = g_A N_A n_e(>E_A) \tag{1.3}$$

$$n_{B+} = g_B N_B n_e(>E_B)$$

where g_i represents the fraction of available electrons which will ionize each species, assumed to be all of the electrons above the ionization energy of that species (i.e., g=1). The fraction of ions belonging to species A is given by the ratio

$$F_{A+} = \frac{n_{A+}}{n_{A+} + n_{B+}} = \frac{A\, e^{-E_A/k_B T_e}}{A\, e^{-E_A/k_B T_e} + (1-A)\, e^{-E_B/k_B T_e}}. \tag{1.4}$$

The standard definition of the enrichment $\mathcal{E}$ is [Gro91]

$$\mathcal{E} = \frac{y_i}{q_i} \tag{1.5}$$

where y_i is the fraction of the i^{th} isotope in the product and q_i is the fraction of i^{th} isotope in the feed gas. Assuming that the same proportion of ions of each species is collected, the enrichment of A is given by

$$\mathcal{E}_A = \frac{\mathcal{F}_{A+}}{A} = \frac{e^{-E_A/k_B T_e}}{A\, e^{-E_A/k_B T_e} + (1-A)\, e^{-E_B/k_B T_e}}. \tag{1.6}$$

For the isotope of interest, Li-6, the energy required for ionization is $E_A = 3.54$ eV when the isotope is excited to the $2P\ ^2P$ state (recall Figure 1.1). The abundant isotope, Li-7, is assumed to remain in the ground state so that $E_B = 5.39$ eV. For Li-6:Li-7 the naturally occurring proportions[Yam79] are 7.4:92.6, so A is 7.4 %. For a plasma with electron temperature $T_e = 3$ eV, the fractional ionization is

$$\mathcal{F}_{Li\text{-}6+} = \left[\frac{7.42(0.307)}{7.42(0.307) + 92.58(0.166)}\right] = 13\% \tag{1.7}$$

Assuming that all Li-6 ions created could be then collected, the final product would have a Li-6:Li-7 ratio of 13:87. The enrichment, as defined above, is then $\mathcal{E}_{Li\text{-}6} = \frac{13}{7.4} = 1.7$.

If this number seems modest, it should be pointed out that this is a simple scheme involving only one laser for excitation of the desired species. The energy required to ionize Li-6 could be decreased considerably with the addition of another laser beam designed to raise the desired species to an even higher energy state. This in turn would greatly increase the fractional ionization, $\mathcal{F}_{Li\text{-}6}$. The electron energy distribution function can be manipulated as well, particularly in these ECR-microwave discharges. It will

be shown later in this dissertation that the electrons obey a Druyvesteyn distribution function which is depleted in high energy electrons as compared with a Maxwellian distribution. This will further increase the enrichment ratio because fewer ground state Li-7 atoms will be ionized.

1.5 Outline of dissertation

This dissertation includes the construction of a lithium plasma source to be used in future laser isotope separation studies. Design and construction of the plasma source are presented in detail in Chapter 2 of this work. To understand the operating characteristics of the source and to optimize the source for these isotope enrichment studies, a number of plasma diagnostics have been employed to fully characterize the discharge.

Chapter 3 presents a method and results from double Langmuir probe studies. The initial studies of argon discharges were made to obtain an estimate of electron temperature and ion densities under different operating pressures and input powers of the source. Optical emission spectroscopy studies of argon-lithium chloride and argon-lithium carbonate discharges are presented in Chapter 4. Chapter 5 contains electron energy distribution function measurements under a variety of operating conditions. These EEDF measurements can be used to optimize plasma conditions for isotope separation. Chapter 6 presents a novel method for studying the uniformity of the ECR region of the cavity discharge. A two-dimensional CCD camera is used to image the optical emission from the discharge in the ECR region. Finally, Chapter 7 contains conclusions from these experiments. The dissertation closes with suggestions for further studies of the plasma source and applications of the source to isotope separation and other research projects.

CHAPTER 2

CONSTRUCTION OF THE PLASMA SOURCE

The discharge used for these experiments is produced with an electron cyclotron resonant (ECR) microwave plasma source. The resonant cavity is very similar in design to one first developed and presented by Mahoney and Asmussen[Mah89,Mah90] in 1989, with some alterations of the gas flow system and modifications to allow a laser beam to cross the discharge region. The source consists of four main components: (1) the microwave resonant cavity, (2) the baseplate and magnet keeper, (3) the gas handling and vacuum system, and (4) the microwave input circuit. This chapter gives a detailed description of these components and how they are assembled.

2.1 Microwave resonant cavity

The microwave resonant cavity is designed around a brass cylinder of inner diameter 8.9 cm (3.5") and outer diameter 9.5 cm (3.75"), a standard size for brass tubing. The tube is enclosed on both ends by baseplates described in the next section. In the middle there is a brass sliding short which may be moved to effectively tune the cavity by adjusting its length. A diagram of the cavity is shown in Figure 2.1. The cavity length may be adjusted from 8 to 15 cm. The cavity is designed to operate at 2.45 GHz, a standard microwave frequency for which components are readily available. The Mahoney source was modified to allow passage of a laser beam down the axis of the cavity by the addition of a 1 cm diameter hole at its center. A

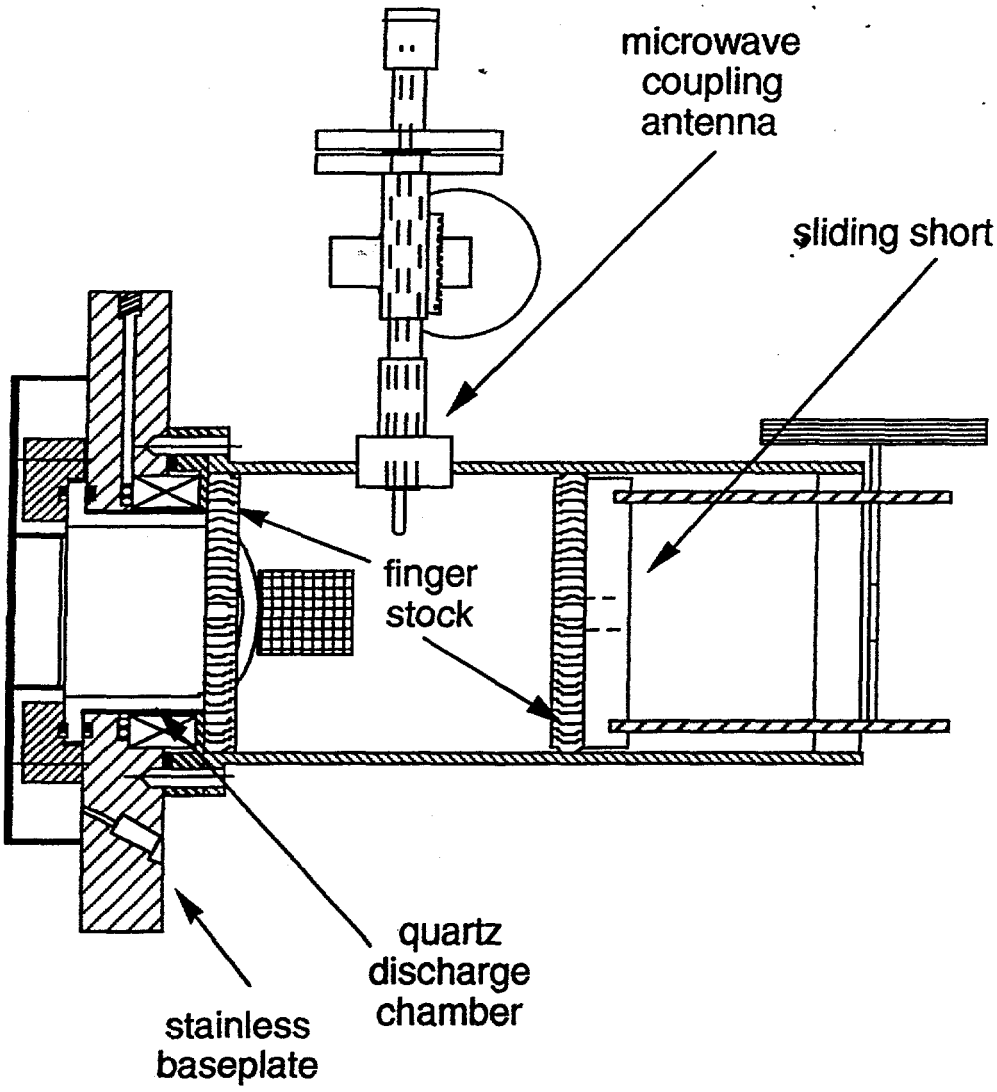

Figure 2.1. The microwave resonant cavity showing brass cavity region and stainless steel baseplate.

simple set of gears is used to raise and lower the sliding short. Silver finger stock circumscribing the endplates is used to provide good electrical contact between the ends and the sides of the cavity.

Microwave radiation is introduced into the cavity through a microwave coupling antenna located in the side of the cavity perpendicular to the axis. The coupling antenna is a 50 Ω coaxial line, which is a standard impedance for microwave transmission lines. To achieve this line impedance, the outer conductor is constructed from 1.3 cm (1/2") outer diameter brass tubing with inner diameter 1.1 cm and the inner conductor from 0.48 cm (3/16") outer diameter brass cylindrical stock. On the opposite end of the antenna, the coaxial line is threaded to allow attachment to a UG-21D/U plug clamp type connector. This transition allows the antenna to be mated to flexible coaxial cable through a type "N" connector. The coupling antenna may extend a distance of 0 cm to 4.4 cm into the cavity to enable matching of the impedance of the cavity with the lossy plasma to the input line and thus reduce reflection of the microwave input signal.

2.2 Baseplate and magnet keeper

The baseplate performs many functions in the system and acts as a transition between the microwave cavity and vacuum vessel. Figure 2.2 shows the detail of the cavity baseplate. The baseplate is constructed from a standard, 20 cm (8"), stainless-steel, copper-gasket-sealed, high-vacuum flange. On the vacuum side of the flange are the quartz discharge chamber, the compression cylinder and the gas distribution cylinder. A plasma discharge is produced inside a quartz chamber which is vacuum sealed with Viton o-rings between the baseplate and an additional compression cylinder.

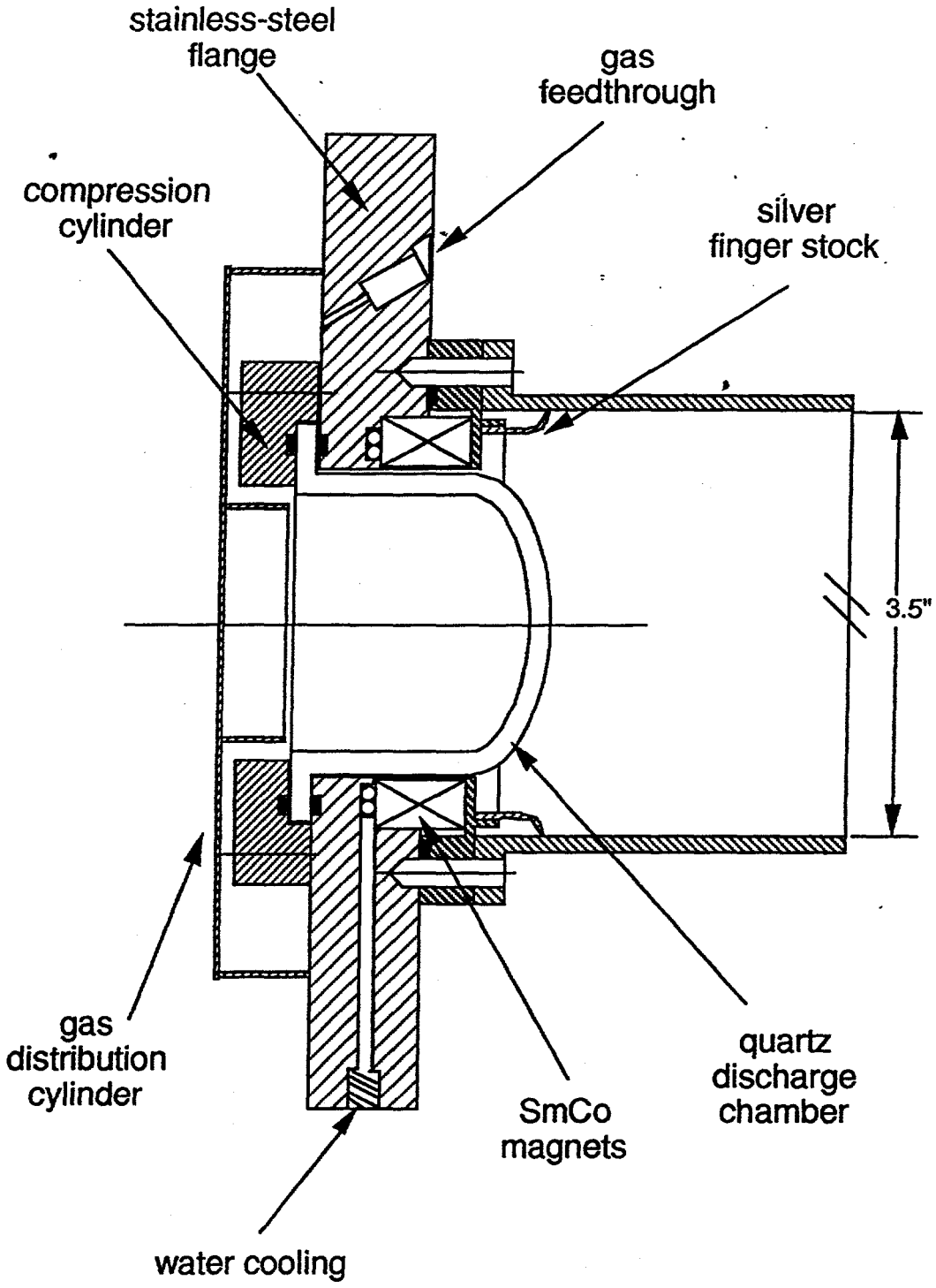

Figure 2.2. The baseplate of the microwave resonant cavity. The baseplate is constructed from a 20 cm, stainless-steel, knife-edge flange available commercially.

Below the quartz cap is a cylinder through which the buffer gas for the experiments is uniformly introduced into the quartz cap.

On the atmospheric side of the baseplate is a channel which holds the magnets and magnet keeper. Located below the magnets is a set of water cooling lines to regulate the temperature of the magnets during operation of the experiment. The magnets are enclosed on the top by a brass cap which also forms the bottom of the resonant cavity. Again, silver finger stock is used to provide good electrical contact with the resonant cavity side walls. Careful placement of the cavity along the axis of the assembly allows the magnets to be located less than 0.5 cm from the inside edge of the quartz cap. The entire resonant cavity is then bolted onto the baseplate.

The magnet keeper is used to hold the eight samarium cobalt (SmCo) magnets (with dimensions of 1.9 cm x 1.3 cm x 0.95 cm) in a cylindrical geometry as sketched in Figure 2.3. It is constructed of soft iron and has three separate pieces. The top and bottom circular pieces have eight rectangular openings to hold the magnets in the correct geometry. The center piece is a simple ring to space the top and bottom of the keeper. The magnets are placed with alternating poles facing inward to form an octapole geometry. Figure 2.3 also shows the 875 gauss region of the magnetic field which corresponds to electron-cyclotron resonance for 2.45 GHz electromagnetic radiation. This region was measured with a Bell 610 Gaussmeter. The maximum magnetic field on the face of each of the eight magnets, as measured by the Gaussmeter, is 3.9 ± 0.1 kGauss.

2.3 The vacuum system

To accurately control the composition of the plasma from which the ion beam is extracted, the plasma region is evacuated to below 5×10^{-7} Torr and

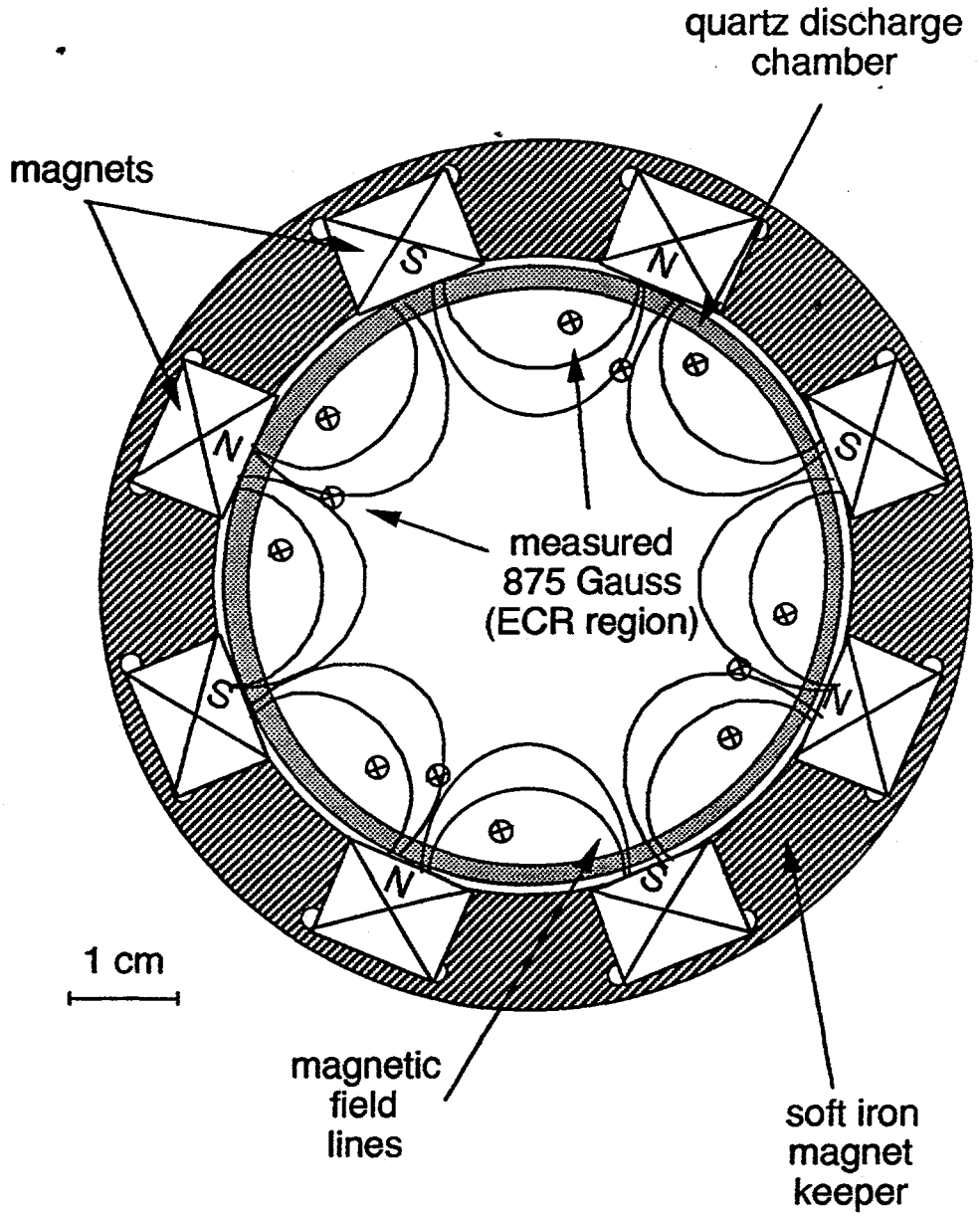

Figure 2.3. Magnets and magnet keeper showing the 875 Gauss region where electron-cyclotron resonance for 2.45 GHz occurs.

back-filled with a buffer gas, typically argon. The flange which functions as the baseplate of the cavity assembly is bolted to one port of a standard 15 cm six-way cross which serves as a vacuum vessel for the experiments, as is seen in Figure 2.4. Glass windows are located on two of the six ports to allow viewing of the plasma for spectroscopic diagnostics. One port is used for other diagnostic tools such as probes and another port is reserved for vacuum gauges. A MKS Baratron capacitance manometer with the range 0.1 to 100 mTorr is used to monitor the pressure during operation and an ionization gauge monitors the system base pressure. Two thermocouple gauges, one near the other gauges in the high-vacuum region and another in the roughed-out region between the turbopump and the mechanical pump, complete the vacuum gauges on the system. All of the vacuum gauges are controlled by a Varian Multi-Gauge controller.

The discharge pressure is maintained by adjusting a butterfly valve on the lowest port of the vacuum chamber. Below the 10 cm Huntington butterfly valve is a 27 cm long extension which leads to the pumping station. The pumping station, manufactured by Varian, is composed of a model V-250 250 l/s turbomolecular pump backed by a model SD90 4.3 m^3/hr mechanical roughing pump. The flow rate of the buffer gas, typically between 1-4 sccm, is controlled by a Matheson W003 flow regulator.

2.4 Microwave power circuit

A diagram of the microwave circuit is shown in Figure 2.5. Microwave power is supplied to the cavity by a Micro-Now model 420B1 continuous-wave power supply. This model is capable of providing power from 0 to 500 W at a fixed frequency of 2.45 GHz. The power is directed through a three-port VTE Microwave model CT-3695-N circulator terminated at the third port with a

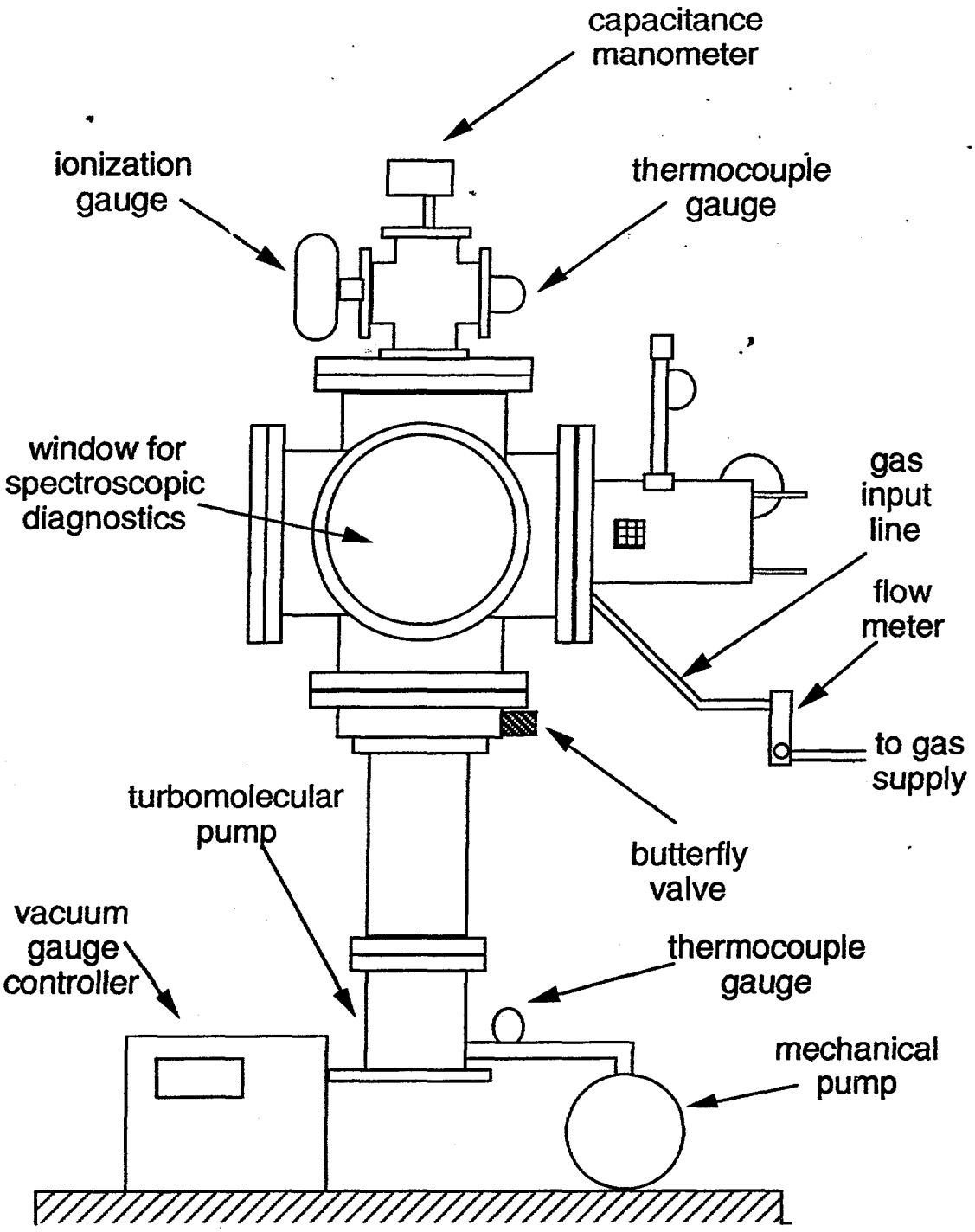

Figure 2.4. Microwave resonant cavity vacuum system setup. All of the vacuum gauges are controlled and read by a multigauge unit.

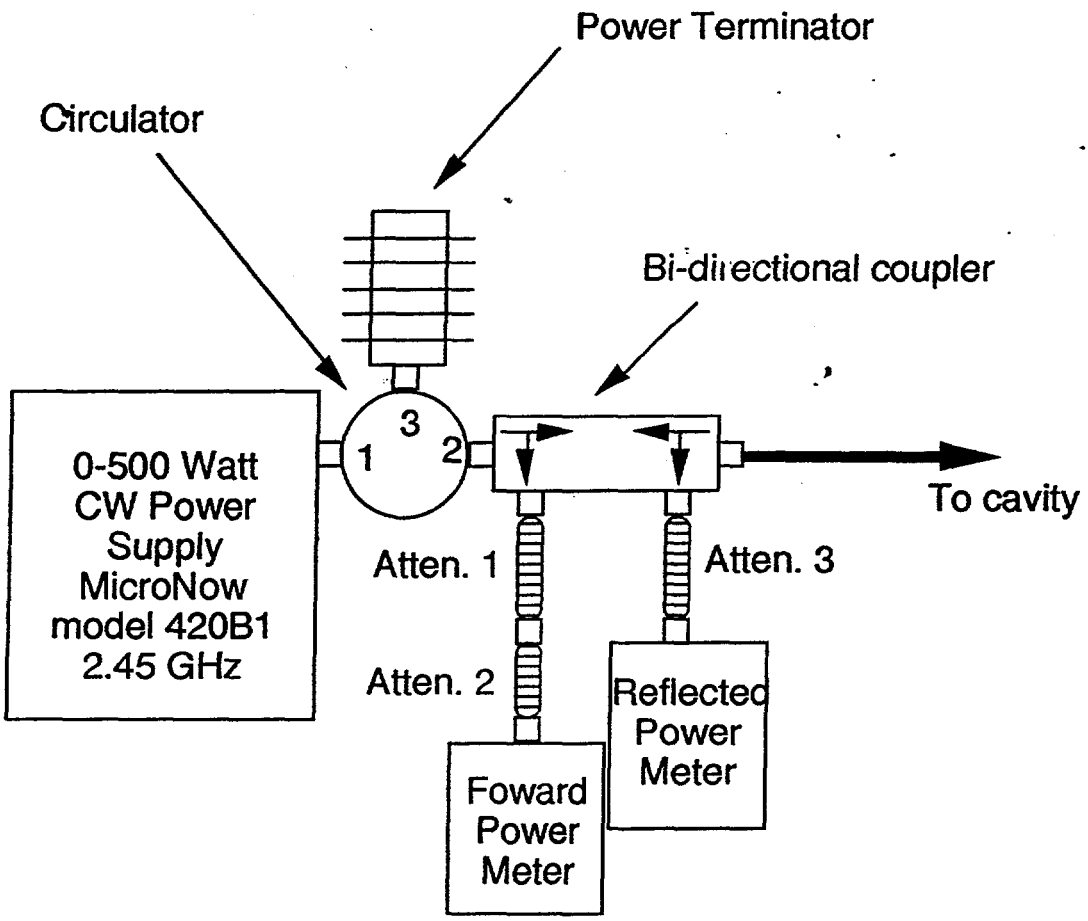

Figure 2.5. The circuit diagram for the continuous wave microwave experiment.

Bird Electronic model 8401 high power terminator. At the second port, a bi-directional coaxial coupler, Narda model 3022, is used to measure the forward and reflected power to and from the cavity. Two Hewlett-Packard model 432A power meters, coupled with a Struthers Electronics model GIL-360A

thermistor and a Hewlett-Packard model 478A thermistor, are used to make the power measurements. To protect the thermistors, attenuators are included in the power measurement circuit. Table 2.1 gives attenuation values for the components used in the microwave circuit. These values were measured using a Hewlett-Packard sweep generator and circuit analyzer.

Table 2.1. Attenuation of components in microwave circuit.

Component	Attenuation at 2.45 GHz
Attenuator 1	-21.1 dB
Attenuator 2	-29.9 dB
Attenuator 3	-31.1 dB
Bi-directional Transmitted	-0.2 dB
Bi-directional Forward	-20.1 dB
Bi-directional Reflected	-20.7 dB
Circulator Port 1 to 2	-0.0 dB
Circulator Port 2 to 3	-0.1 dB

2.5 Initial plasma operation

Initial testing and operation of the source was performed with argon discharges at pressures ranging from 5 to 20 mTorr. Details of the discharge characteristics are given in Chapter 3. Some attention needs to be given to the method for obtaining a discharge in this cavity. Because of its small size, this particular cavity supports only two vacuum modes, the TE_{111} mode at a height of 10.5 cm and the TE_{011} mode at a height of 6.1 cm. Details of the mode derivation are given in Appendix A. Because of the location of the input antenna at 6.3 cm above the baseplate, operation in the TE_{011} mode is not practical. The discharge, however, will not ignite near the vacuum operating mode (TE_{111}) as is the case for similar cavities.[McC93b] The method used to ignite a discharge in the cavity follows.

To break down the gas the cavity is tuned "short," near the TE_{011} mode. Because of the input antenna location, the cavity height should not be decreased below 7.0 cm to prevent arcing between the antenna and sliding short. After the discharge has been initiated, the cavity is lengthened and tuned to minimize reflected power. Both the cavity length and input probe depth must be adjusted to insure proper tuning. Table 2.2 gives cavity length and probe depth for lighting and operating conditions.

Table 2.2. Cavity length and probe depth for ignition and tuning of an 8 mTorr argon discharge.

	Cavity Length	Probe Depth
Breakdown	8.2 cm	7.0 cm
Tuned	10.2 cm	7.3 cm

CHAPTER 3

LANGMUIR PROBE I: CHARACTERIZATION OF THE SOURCE

The ECR microwave resonant cavity was initially operated with argon-only discharges. To obtain the general discharge characteristics of the plasma, double Langmuir probe experiments were performed for a variety of operating powers and pressures. From the Langmuir probe measurements, electron temperature and ion density can be determined, and with the assumption of charge neutrality, electron density as well. In this chapter, the basic discharge characteristics as measured with a swept, floating, double Langmuir probe will be presented.

3.1 Double Langmuir probe theory

The floating double probe method for measuring electron temperatures and plasma densities was first proposed by Johnson and Malter in 1950.[Joh50] The method was originally proposed for use in decaying plasmas as an alternative to the single probe method. Because the plasma potential is a function of time in a decaying plasma, it is difficult to maintain a constant probe-plasma potential difference. With the floating probe method, the entire probe circuit is isolated from ground and floats at the plasma potential. The floating probe method is also convenient for electrodeless discharges such as the one produced in a microwave resonant cavity because they do not require a grounded reference point against which the potential difference is applied. The floating probe has the added advantage of

perturbing the plasma much less than the single probe because it never draws more than the "ion saturation" current.

Two important plasma parameters can be derived from the voltage-current characteristic of a floating probe: the electron temperature, T_e, and the ion density, n_i. Under the quasineutrality assumption, the electron density is assumed to be equal to the ion density. Double Langmuir probe theory has been discussed in many papers and texts[Joh50,Che65,Swi69] and thus details of derivations will not be included in this work. Beginning with the assumption that the system is floating and forms a closed current loop, an equation for the electron temperature can be found in terms of the effective "ion saturation" current for each probe (I_{s1} and I_{s2}) and the slope of the voltage-current curve at the origin, $\left[\frac{dI}{dV}\right]_{V=0}$. The electron temperature is given by[Che65]

$$T_e\,[eV] = \frac{I_{s1} \cdot I_{s2}}{\left[\frac{dI}{dV}\right]_{V=0}\left(I_{s1} + I_{s2}\right)} . \qquad (3.1)$$

Figure 3.1 shows a typical double Langmuir voltage-current characteristic as measured by this probe and illustrates the quantities used in equation 3.1. Johnson and Malter[Joh50] propose two methods for determining the effective saturation current. One method is to determine the point at which the "knee" occurs in the voltage-current characteristic and using the current value at that point. A second method, which was used in this experiment, uses the current value at the intersection of a tangent line to the curve at the origin and a tangent to the curve in the ion-saturation region.

The Bohm sheath criterion is applied to determine the ion density. From this criterion the ion current flux is given by

$$J_i = 0.61\, e\, n_i \sqrt{\frac{k_B T_e}{m_i}}, \qquad (3.2)$$

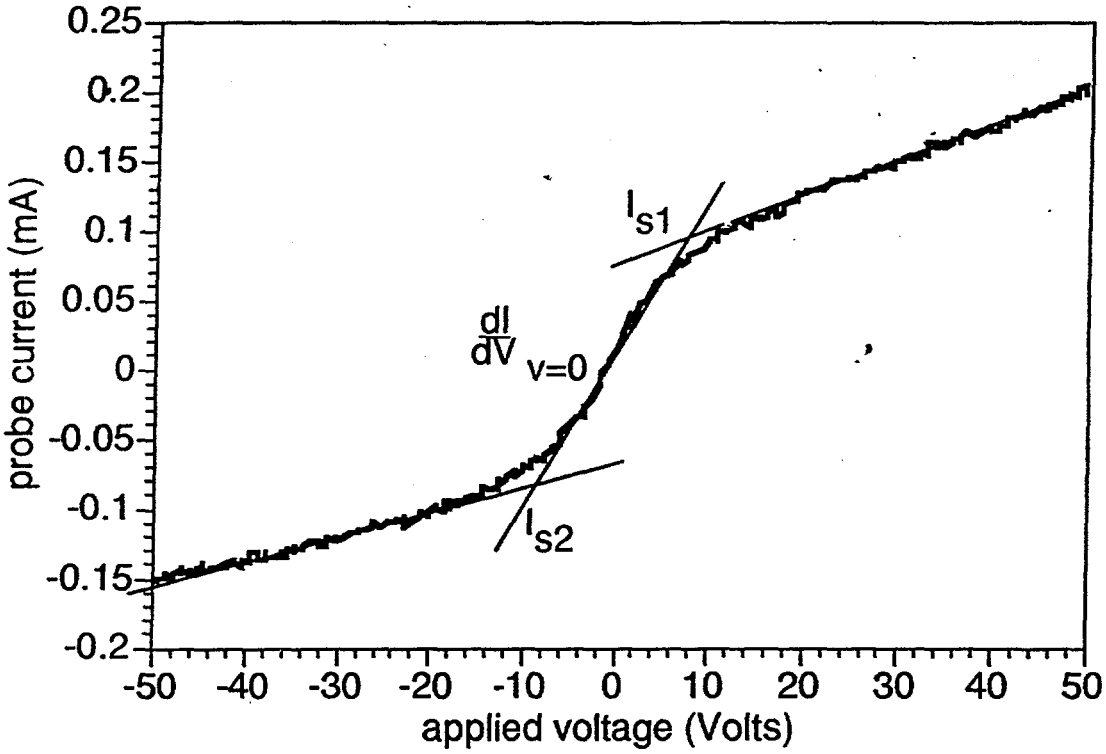

Figure 3.1. Typical double Langmuir probe curve for a 4 mTorr argon discharge showing the values used in determining electron temperature and ion density. The saturation regions and the transition region are fit to a line.

where e is the charge of an electron, n_i is the ion density is particles/m^3, k_B is Boltzmann's constant, and m_i is the ion mass. If A_p is the area of the probe collecting current, then (3.2) can be rewritten

$$n_i = \frac{I_s}{0.61\, e\, A_p}\sqrt{\frac{m_i}{k_B T_e}}. \qquad (3.3)$$

The saturation current, I_s, was taken as the average of I_{s1} and I_{s2}. Ideally, $I_s = I_{s1} = I_{s2}$ for probes of equal area, and the values were close in these experiments.

An important plasma parameter which can be inferred from the electron temperature and plasma density is the electron Debye length. The Debye length is a measure of the shielding distance about a test charge or sheath thickness near a plane held at constant potential (see also section 4.5.1). The Debye length of a plasma is given by[Che84]

$$\lambda_D = \sqrt{\frac{\varepsilon_0 k_B T_e}{ne^2}} = 740\sqrt{\frac{T_e}{n}}\,[\text{cm}] \qquad (3.4)$$

where T_e is the electron temperature in electron volts and n is the plasma density in cm^{-3}.

As with any measurement tool, double probe theory makes assumptions about the nature of the discharge being measured. The first assumption is that the electron energy distribution of the plasma can be described by a Maxwellian distribution.[Che65] The electron energy distribution function (EEDF) for discharges in a similar ECR-resonant cavity source have been measured by Hopwood, et al.[Hop90] and found to be non-Maxwellian. Hopwood found the EEDF to be between a Maxwellian and a Druyvesteyn distribution with no high-energy tail for the electrons collected downstream of the cavity at discharge pressures below 5 mTorr. Further details and measurements of the exact EEDF are given in Chapter 5 of this dissertation. Despite this difficulty, standard Langmuir probe theory has been used in this experiment. The theory is not easily adapted to a general electron energy distribution, but the Maxwellian assumption gives reasonable order-of-magnitude estimates of charged particle density and remains a

useful tool for predicting the source's operating characteristics. Another assumption is that the electron Debye length of the plasma is smaller than the probe radius. That condition is met by this experiment ($\lambda_D \approx 0.007$ cm, $r_p = 0.02$ cm).

3.2 Experimental technique

The Langmuir probe is illustrated in Figure 3.2 as is its location relative to the plasma. The collector of the double Langmuir probe is composed of tungsten wire of diameter 0.041 cm. One wire is fed through each opening of double bore alumina tubing with outside diameter 0.32 cm and inner diameter 0.10 cm. This probe tip extends 0.65 cm from the alumina tubing and the two wires are 0.15 cm apart. The exposed area of one probe tip, A_p in equation 3.3, is 0.084 cm^3. The alumina tubing is centered on a 1.91 cm (3/4") tube of stainless steel by a small, stainless steel holder. An electrical vacuum feedthrough at the outside end of the tube provides the electrical connection to the Langmuir probe circuit. The probe is fed into the vacuum chamber through a 1.91 cm (3/4") stainless steel, slip-seal coupling which has been welded onto a standard 20.3 cm (8") stainless steel flange, allowing linear motion along the axis of the cavity.

The probe is biased through an isolation transformer to provide electrical isolation of the probe tip. Power is provided at 60 Hz through a rheostat which can be varied from 0 to 120 volts AC. The probe voltage is measured using a voltage divider on the grounded side of the transformer and the probe current is measured with a Pearson model 110A current meter. Both the voltage and current measurements were collected and digitized on a storage oscilloscope. The circuit used was identical to that described previously by McColl, Brooks, and Brake[McC93a] and is shown in Figure 3.3.

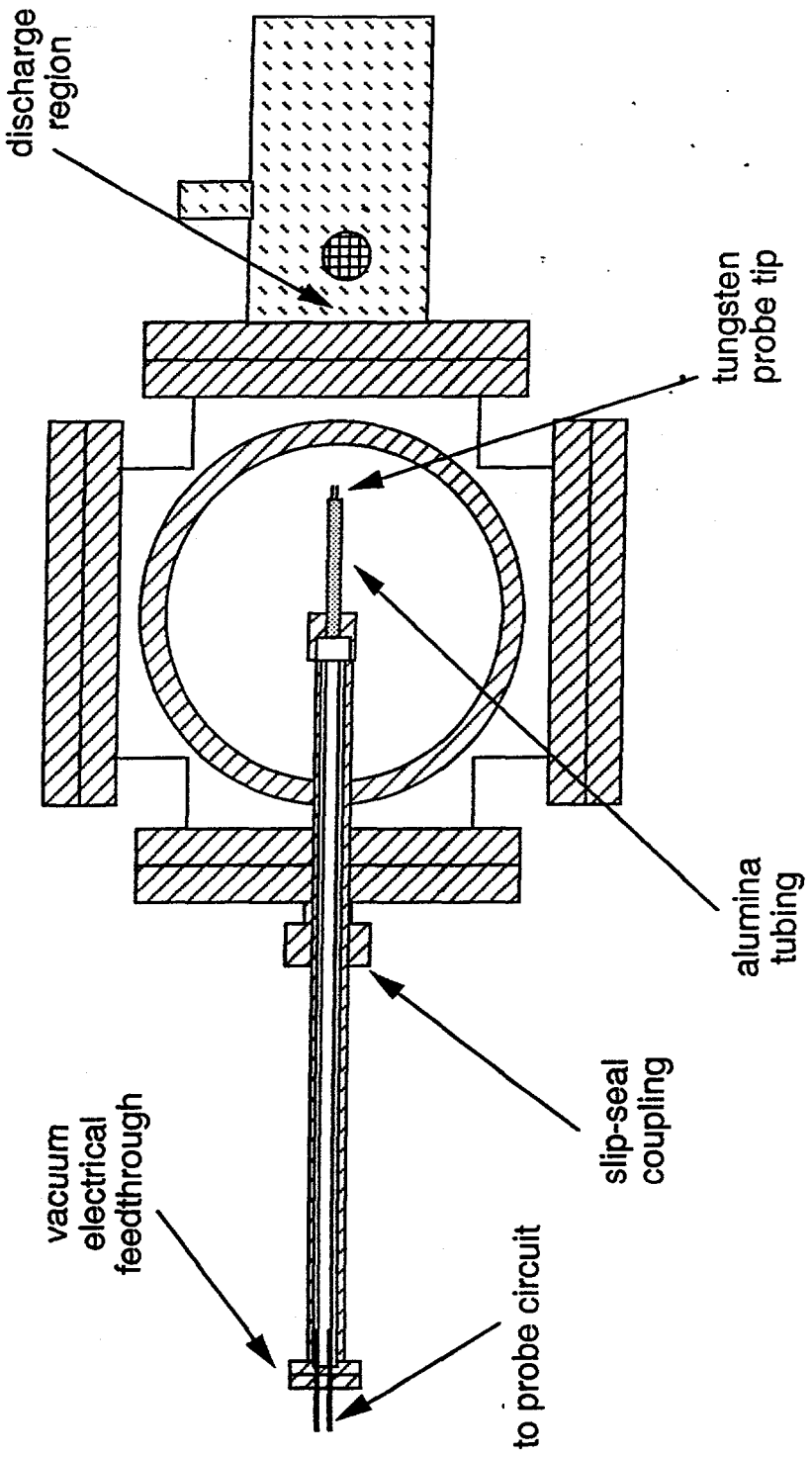

Figure 3.2. Langmuir probe feedthrough shown relative to microwave resonant cavity.

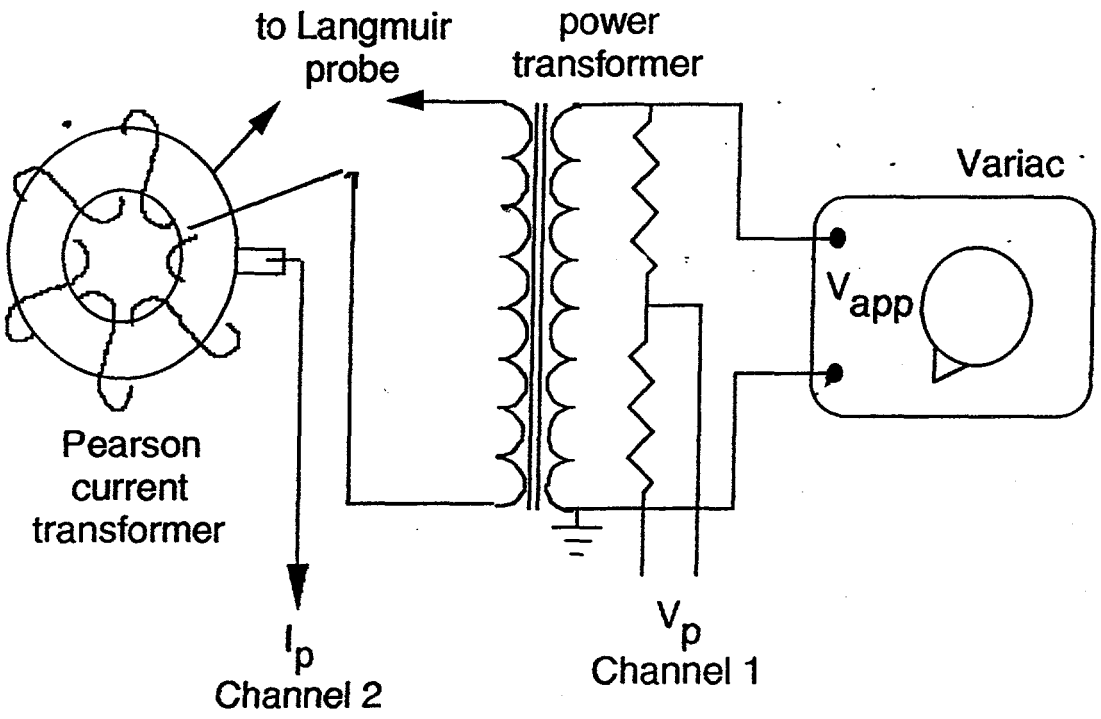

Figure 3.3. Circuit used for acquisition of Langmuir probe trace.

The digitized probe voltage and current data are transferred to a personal computer through a GPIB connection. Linear regression in a spreadsheet program is used to find the lines shown in Figure 3.1, and the intersection of the lines in the "ion saturation" region and the transition region provided the values for I_{s1} and I_{s2}. The slope of the line passing through the origin provides $\left[\frac{dI}{dV}\right]_{V=0}$.

3.3 Experimental results

Using the technique described above, the ion density and electron temperature of an argon-only discharge were measured for discharges in the

range of 4 to 20 mTorr and input powers of 90 to 250 Watts. Figure 3.4 is a plot of ion density for various pressures at a distance of 3.5 cm downstream from the base of the cavity. For a low input power of 105 Watts, the ion density ranged from 3×10^{10} cm^{-3} for an argon partial pressure of 4 mTorr to 7×10^{10} cm^{-3} for a pressure of 20 mTorr. This corresponds to a fractional ionization of 0.01% to 0.02% for 20 mTorr and 4 mTorr, respectively. At a higher input power of 235-245 Watts, the ion density increased to $5 \times 10^{10} cm^{-3}$ for 4 mTorr and 1.7×10^{11} cm^{-3} for 20 mTorr. The fractional ionization at this higher input power level is 0.02% to 0.04%, again for 20 mTorr and 4 mTorr. The ionization fraction increases with decreasing pressure as more energy/atom is coupled to the electrons. Further downstream, at 5.4 cm, the ion density decreases by a factor of about 2.5, as shown in Figure 3.5. More detailed measurements of the density as a function of downstream distance will be given in Chapter 5.

The electron temperature is plotted in Figure 3.6 as a function of input power as measured by the probe at 3.5 cm downstream. The electron temperature remained constant at 3.3 ± 0.2 eV for input powers of 100 to 250 Watts and pressures from 7 to 20 mTorr. The electron temperature can remain constant with increasing input power because the plasma volume or ionization will increase to keep the power density constant.[Pas91] At the lowest pressure measured, 4 mTorr, a slight increase in electron temperature was observed. The electron temperature increased moderately, from 3.3 ± 0.2 eV to 3.9 ± 0.2 eV, as the input power was raised from 100 to 250 Watts. The electron Debye length is plotted as a function of discharge pressure in Figure 3.7. The Debye length decreases with increasing discharge pressure as expected because of increasing ion density.

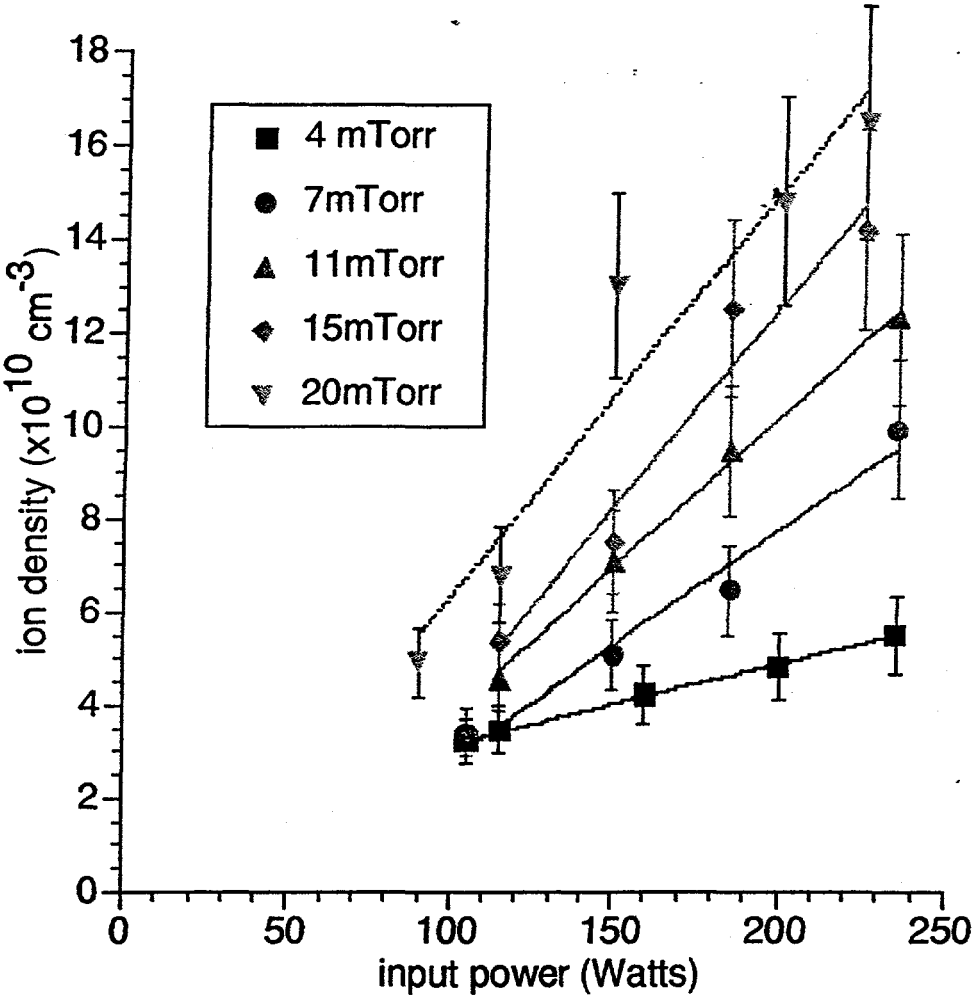

Figure 3.4. Ion density of an argon discharge as a function of input power for pressures ranging from 4-20 mTorr at a distance of 3.5 cm downstream.

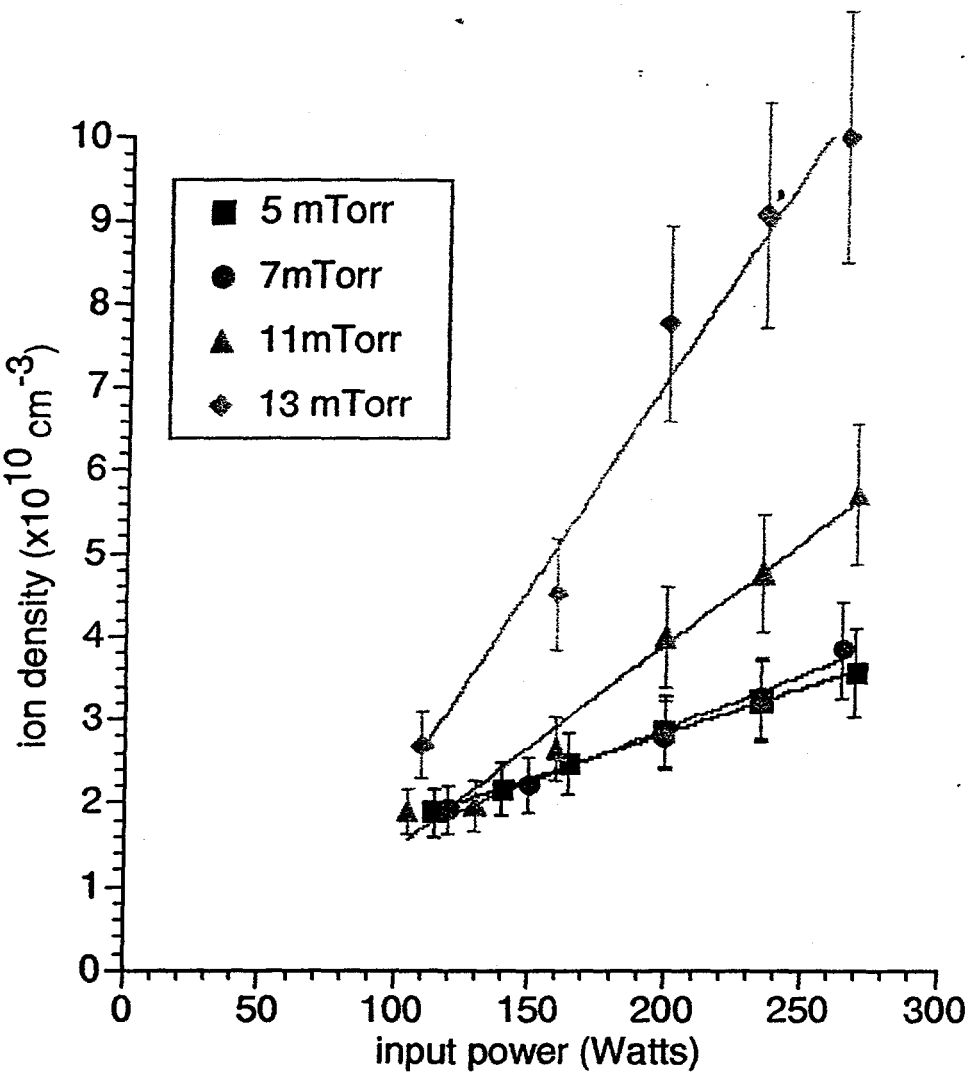

Figure 3.5. Ion density for an argon discharge as a function of input power for pressures ranging from 5-13 mTorr at a distance of 5.4 cm downstream.

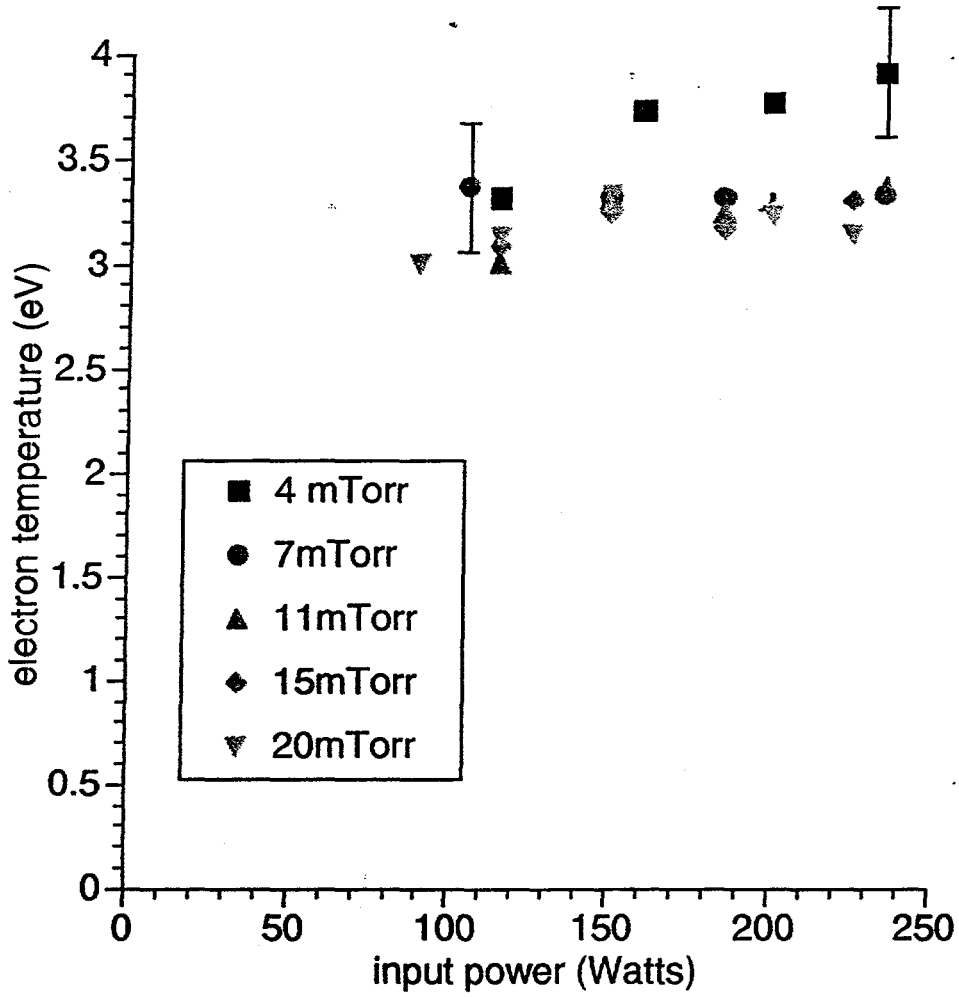

Figure 3.6. Electron temperature of an argon discharge as a function of input power for pressures ranging from 4-20 mTorr at a distance of 3.5 cm downstream.

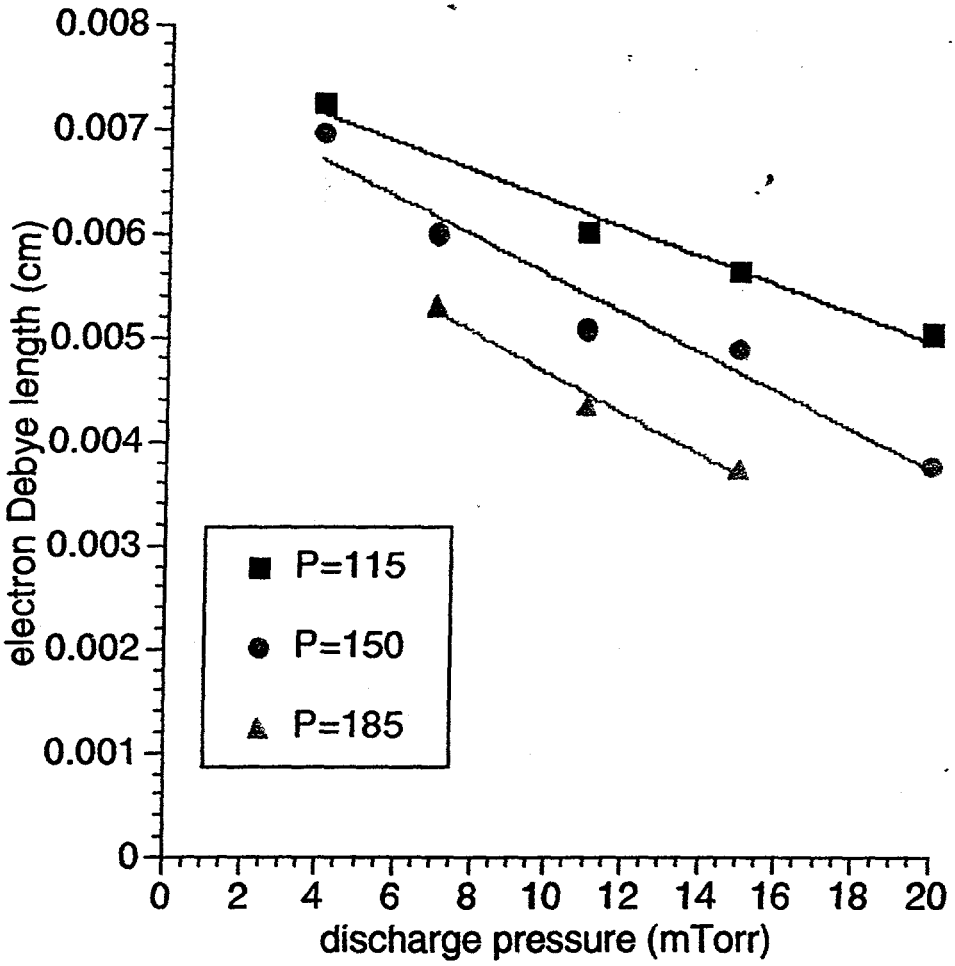

Figure 3.7. Electron Debye length as a function of discharge pressure for several input powers. Values are from Langmuir probe measurements 3.5 cm downstream of the cavity.

CHAPTER 4

OPERATION AS A LITHIUM PLASMA SOURCE

Following the argon-only experiments, lithium was introduced into the discharge through two different lithium-containing compounds: lithium chloride (LiCl) and lithium carbonate (Li_2CO_3). The primary diagnostic used to study the lithium-argon discharges was optical emission spectroscopy. The double Langmuir probe was used to some extent, but became quickly contaminated in the presence of LiCl in the discharge. This chapter will include a discussion of the effects of the lithium compounds on the discharge parameters and resonant cavity behavior.

4.1 Experimental method for lithium discharges

Two different lithium-containing compounds were used to introduce lithium into the discharge. Table 4.1 summarizes some of the physical properties of these compounds. The lithium compounds were introduced to the system by placing the solid material directly into the quartz cup. Argon gas was then leaked into the system to a partial pressure of 20 mTorr and a discharge ignited with the argon gas. Lower initial discharge pressures were attempted, but it was found that an argon pressure of at least 20 mTorr was needed to ignite a discharge with solids placed in the quartz cup.

This method of introducing lithium into the system has proven adequate for the experiments presented in this work. The method of placing a lithium-containing solid directly in the discharge cup was chosen because of

its success with copper chloride discharges in a microwave resonant cavity.[McC93b] In those experiments, the use of an external heater was unsuccessful because of condensation along the path from the heater to the discharge chamber.

Table 4.1. Properties of lithium containing compounds[CRC81]

	LiCl	Li_2CO_3
Molecular Weight	42.39	73.89
Crystalline Form	white, cubic	white, monoclinic
Density (gm/cm^3)	2.068	2.11
Melting Point (°C)	605	723
Boiling Point (°C)	1325-1360	1310 decomposes
Solubility	63.7 g/ 100cc in water; 25.10g/ 100cc in alcohol	1.54 g/100 cc in water; insoluble in alcohol and acetone
% lithium, by weight	16.4 %	18.8 %

The method of placing the solid in the discharge directly has several disadvantages. First, and foremost, it is difficult to provide a constant amount of lithium vapor into the system, as will be shown in the following

section of this chapter. The amount of lithium dissociated and contained in the discharge is not easily measured and depends on background argon discharge parameters. Secondly, vacuum must be broken to place the lithium onto the glass cup. Because the lithium compounds (particularly LiCl) absorb much water vapor from the air, the chamber must be allowed to pump down overnight to achieve a reasonable base pressure.

4.2 Spectroscopic measurements

Figure 4.1 is a sketch of the optical emission spectroscopy experimental setup. Spectra were taken using an Acton Research Corporation model VM-510 one meter vacuum monochrometer. The exit slit was fitted with a Tracor-Northern TN-6100 gated, intensified, 1024 channel diode array detector. By using a fiber optic link, light from different regions of the discharge could be imaged onto the entrance slit of the spectrograph.

Figures 4.2 to 4.6 contain optical emission spectra from 3950 Å to 8100 Å. The spectra were taken of an argon/LiCl discharge with argon partial pressure of 8 mTorr and input power of 185 Watts. These spectra were compared with known atomic[Rea80] and molecular[Pea41] transitions. Most of the known neutral argon transitions are identified as well as many argon ion transition regions where neutral argon transitions are weak (see Figure 4.2(b)). Neutral lithium lines are seen at 4602.8 Å, 6103.6 Å, and 6707.8 Å, but no evidence of ionized lithium was observed. No molecular bands corresponding to LiCl were noted, nor were any chlorine transitions seen. The chlorine freed in the discharge most likely reacted with the quartz discharge cup as evidenced by etching of the cup. The mercury transitions identified on the spectra are from the room lights.

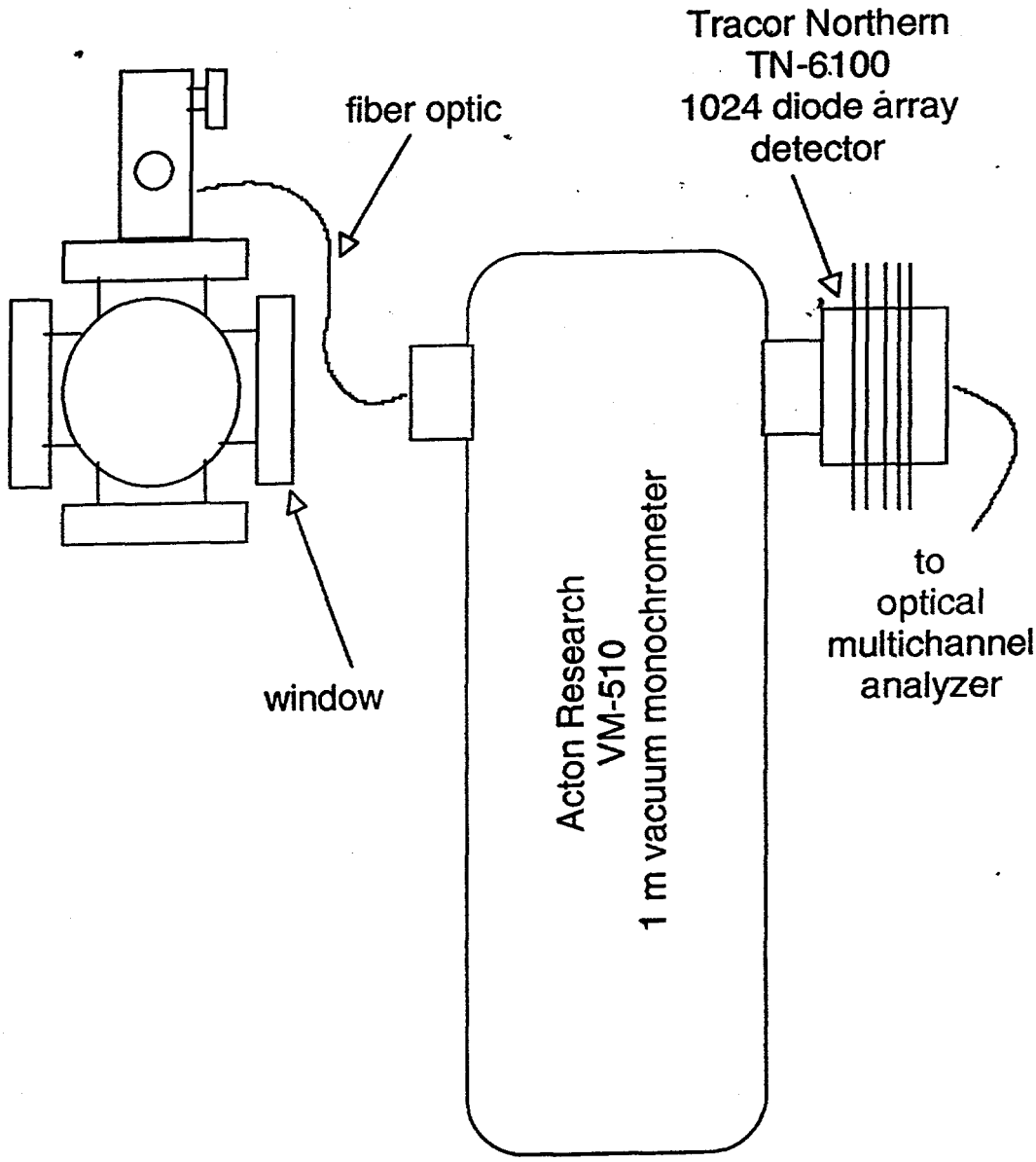

Figure 4.1. Optical emission spectroscopy experimental setup. Light was gathered either through a window downstream from the cavity or by fiber optic directed toward a window in the cavity itself.

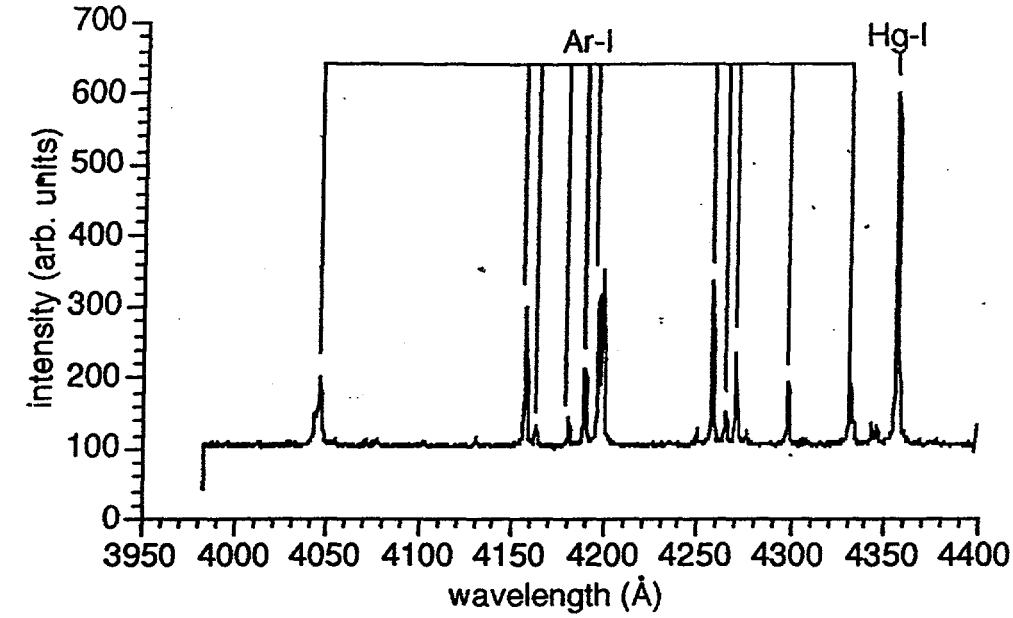

(a)

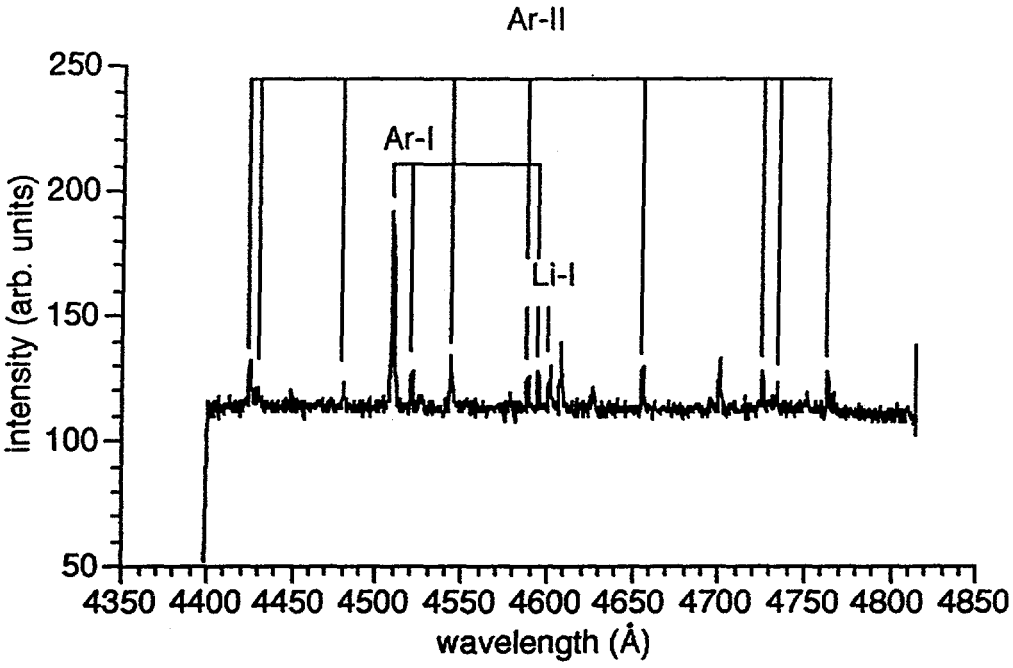

(b)

Figure 4.2. Optical emission spectra of an argon/LiCl discharge at 8 mTorr and 185 Watts. (a) 3975 Å - 4400 Å. (b) 4400 Å - 4825 Å.

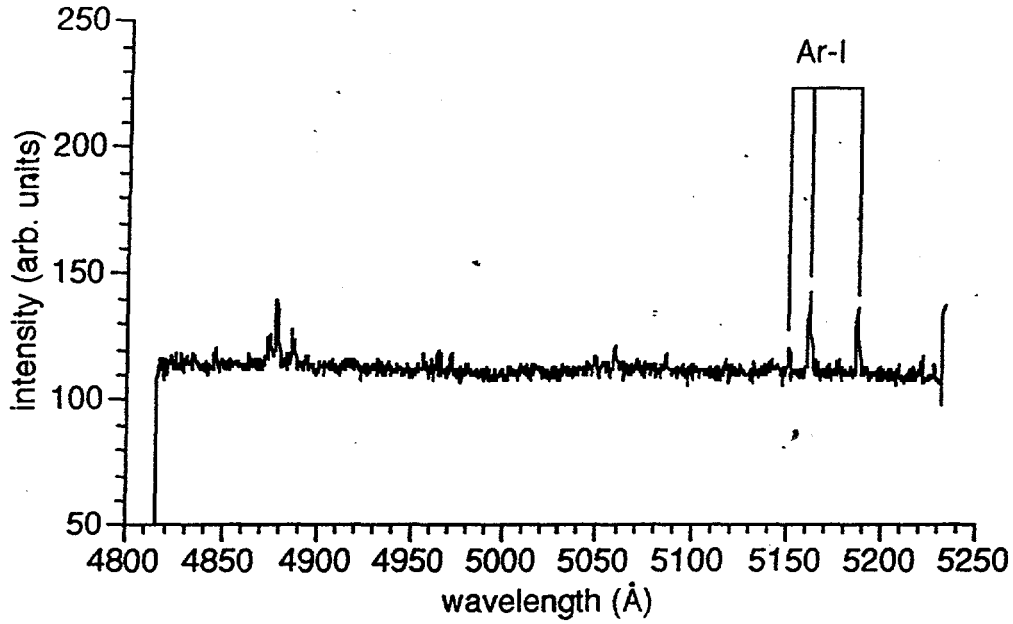

(a)

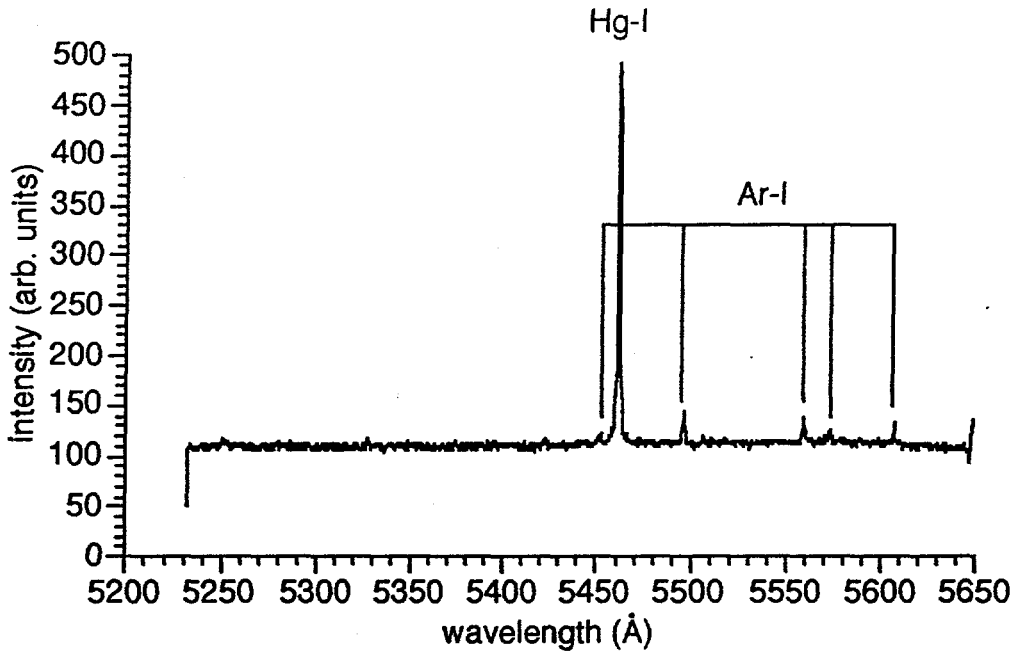

(b)

Figure 4.3. Optical emission spectra of an argon/LiCl discharge at 8 mTorr and 185 Watts. (a) 4815 Å - 5230 Å. (b) 5230 Å - 5650 Å.

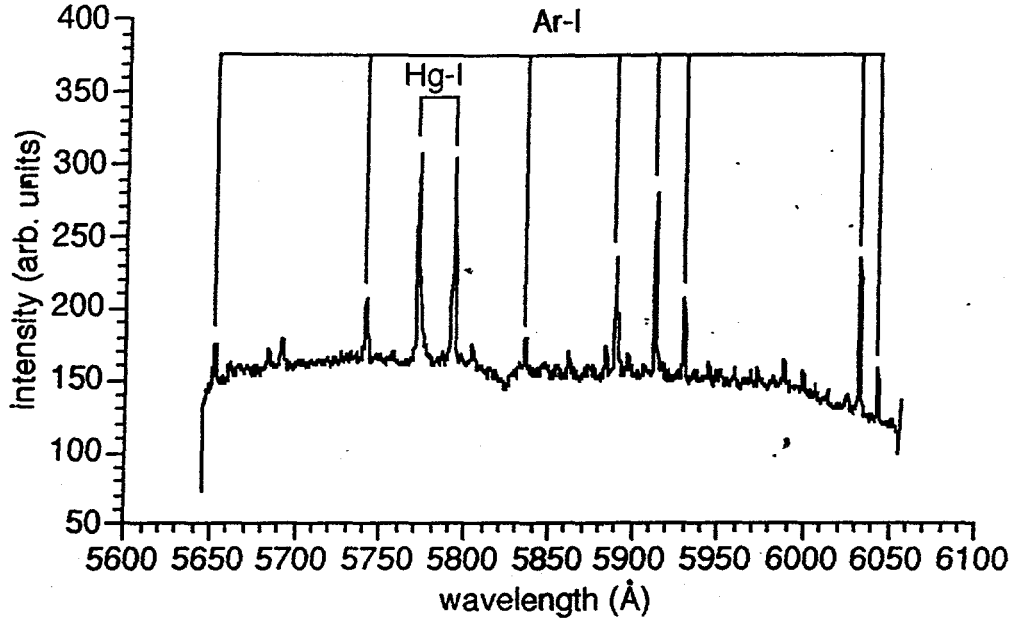

(a)

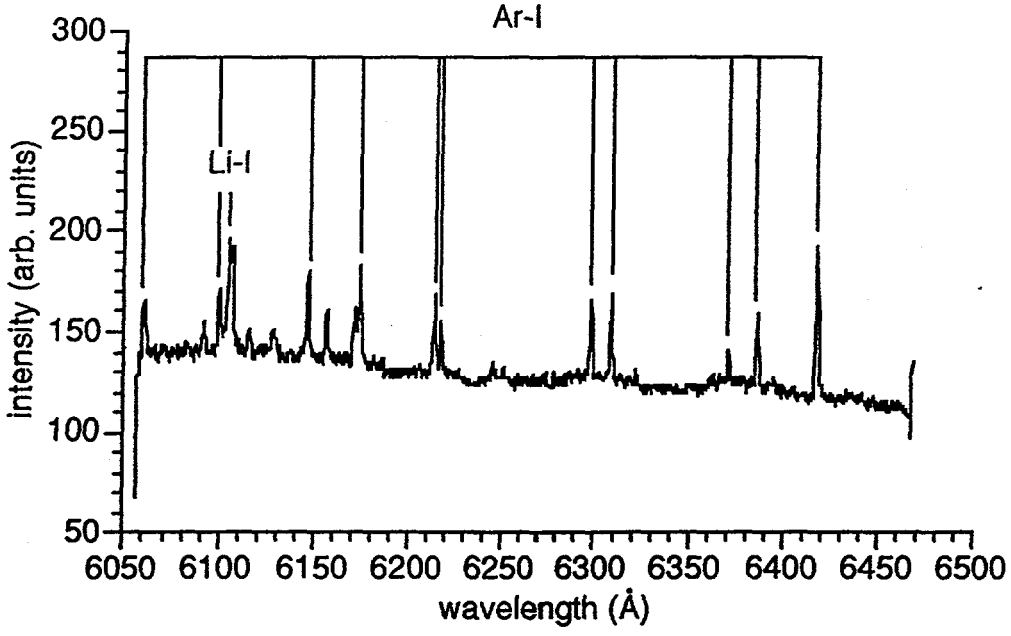

(b)

Figure 4.4. Optical emission spectra of an argon/LiCl discharge at 8 mTorr and 185 Watts. (a) 5650 Å - 6050 Å. (b) 6050 Å - 6470 Å.

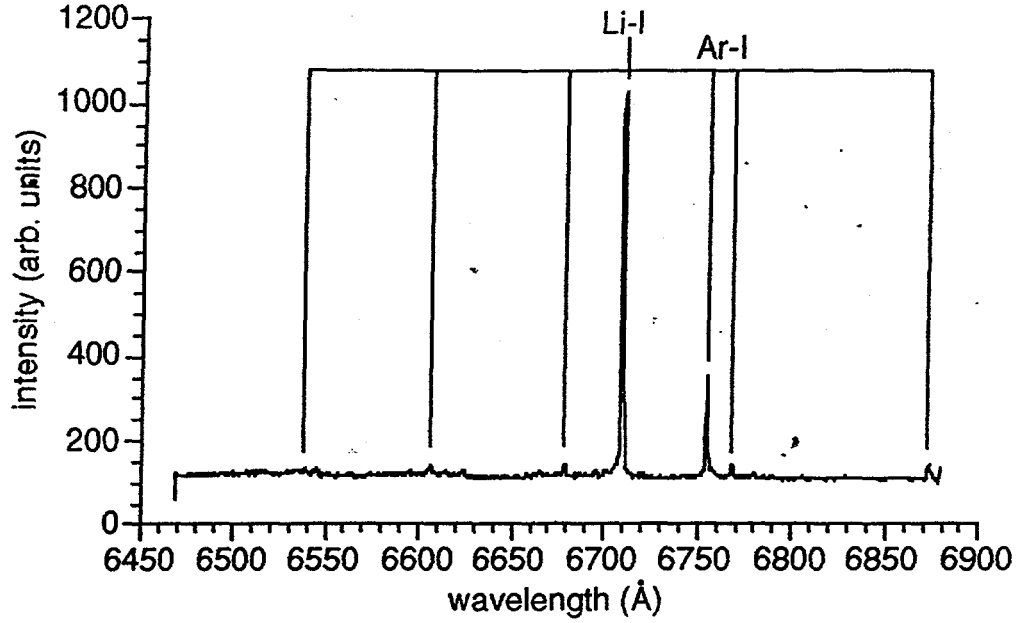

(a)

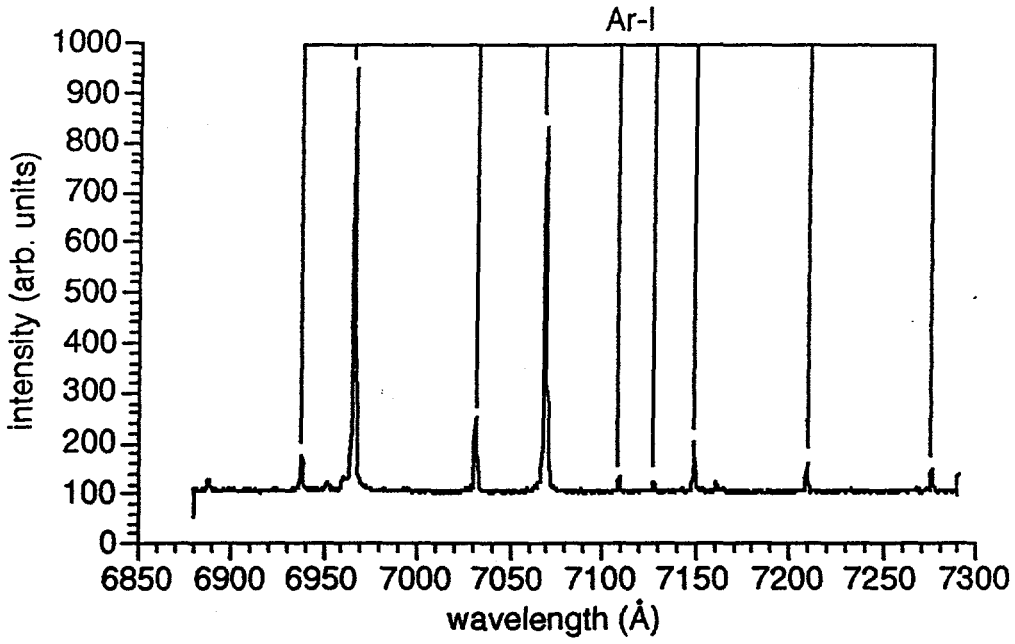

(b)

Figure 4.5. Optical emission spectra of an argon/LiCl discharge at 8 mTorr and 185 Watts. (a) 6470 Å - 6880 Å. (b) 6880 Å - 7290 Å.

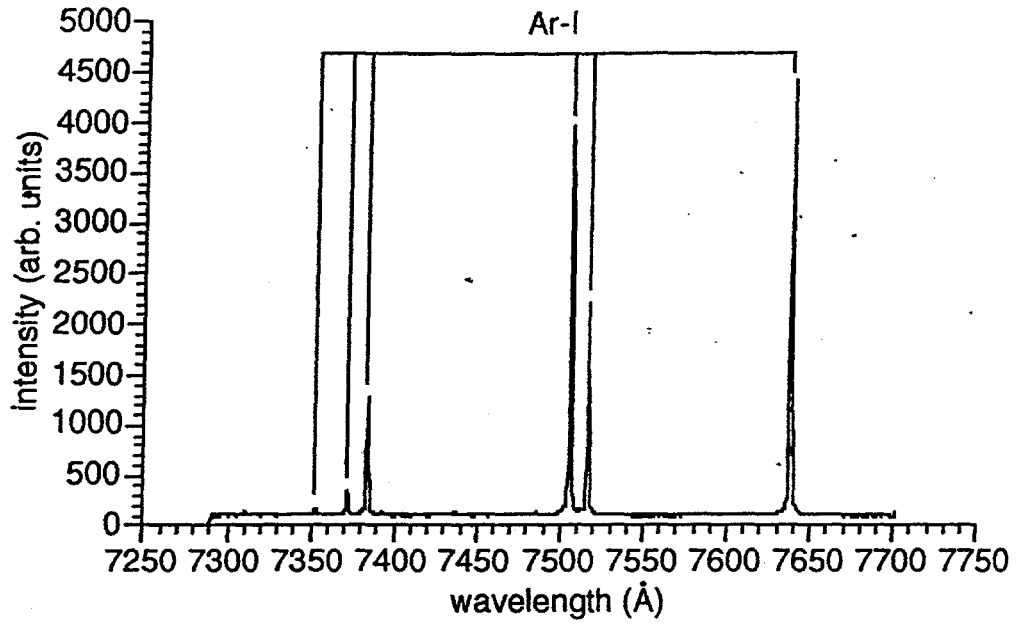

(a)

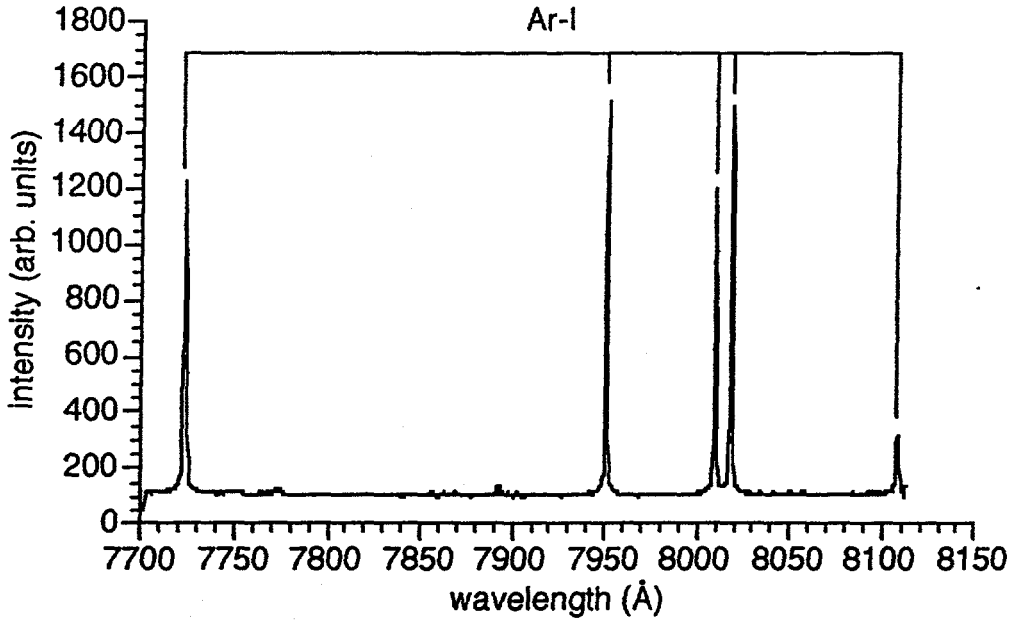

(b)

Figure 4.6. Optical emission spectra of an argon/LiCl discharge at 8 mTorr and 185 Watts. (a) 7290 Å - 7700 Å. (b) 7700 Å - 8110 Å.

4.3 Boltzmann temperatures

For an optically thin plasma in local thermodynamic equilibrium (LTE), the Boltzmann formula holds and can be used to determine the electron temperature of the plasma. For cases in which LTE does not hold, the Boltzmann temperature is the bound electron temperature, known as the electronic temperature, which can indicate a lower bound of the electron temperature. Many texts derive the excitation temperature (see for example [Loc68,Mar68]), so only an outline of its derivation will be given here. In thermodynamic equilibrium, the fraction n_i of atoms in the i^{th} quantum state with energy E_i is governed by the Boltzmann distribution:

$$\frac{n_i}{n} = \frac{g_i}{Z(T)} \exp\left(-E_i/k_B T\right) \tag{4.1}$$

where g_i is the degeneracy of the i^{th} level. The partition function Z(T) is given by the sum

$$Z(T) = \sum_i g_i \exp\left(-E_i/k_B T\right) \tag{4.2}$$

The intensity of a thermally excited spectral line is given by

$$I = \frac{1}{4\pi} A_{ki}\, n_k\, h\nu_{ki} L = \frac{1}{4\pi} A_{ki} \frac{g_k}{Z} n h\nu_{ki} L \exp(-E_k/k_B T) \tag{4.3}$$

where A_{ki}, the Einstein coefficient for spontaneous emission, is the probability per second that an atom in state i will spontaneously emit a quantum $h\nu_{ki}$ and be de-excited to state k, where h is Plank's constant. In equation 4.3, L is the optical path length; ν_{ki} is the frequency of light emitted; n_k is the number of atoms in state k; and g_k is the degeneracy of that state. Equation 3.6 can be rearranged to give

$$\ln\left(\frac{I_{ki}\lambda_{ki}}{g_k A_{ki}}\right) = \ln\left(\frac{hcN_o L}{4\pi Z}\right) - \frac{E_k}{k_B T} \tag{4.4}$$

where E_k is the energy of the upper energy level. I_{ki} is the intensity and λ_{ki} the wavelength of light associated with the transition from state k to state i. From this arrangement it is seen that a plot of E_k vs. $\ln\left(\frac{I_{ki}\lambda_{ki}}{g_k A_{ki}}\right)$ results in a line whose negative inverse slope is the bound electronic temperature. Griem has developed a formula by which one can determine if the electronic temperature approximates the free electron temperature.[Gri64] The condition is given by

$$n_e \geq 7 \times 10^{18} \frac{z^7}{n^{17/2}} \left(\frac{k_B T}{z^2 E_H}\right)^{1/2} [cm^{-3}]. \qquad (4.5)$$

For neutrals, the charge state $z = 1$, n=3, and $E_H = 13.6$ eV. For an argon discharge at 3 eV, the electron density must exceed 3×10^{14} cm^{-3}. This density is not reached in the discharge studied, so all temperatures measured by this method will be bound *electronic* temperatures as opposed to electron temperatures. However these values can give a lower bound on T_e as will be shown.

Figure 4.7(a) is a typical spectrum from which Boltzmann electronic temperatures were calculated. Table 4.2 contains the energy levels, Einstein coefficients and degeneracy of the lines used for Boltzmann calculations. The detector response as a function of wavelength is plotted in Figure 4.7(b), along with the known spectrum of an Optronic Laboratories Standard of Spectral Irradiance. The dashed line indicates is the actual spectral irradiance of the calibrated lamp. All spectra used for electronic temperature calculations were calibrated against the known lamp spectrum.

Figure 4.8 is an atomic Boltzmann plot of the spectrum in Figure 4.7. A least squares linear curve fit of the data results in a slope of -1.2 eV^{-1}. This corresponds to an electronic temperature of 9800 K (0.85 eV). Application of equation 4.5 indicates that the electron density needs to be greater than

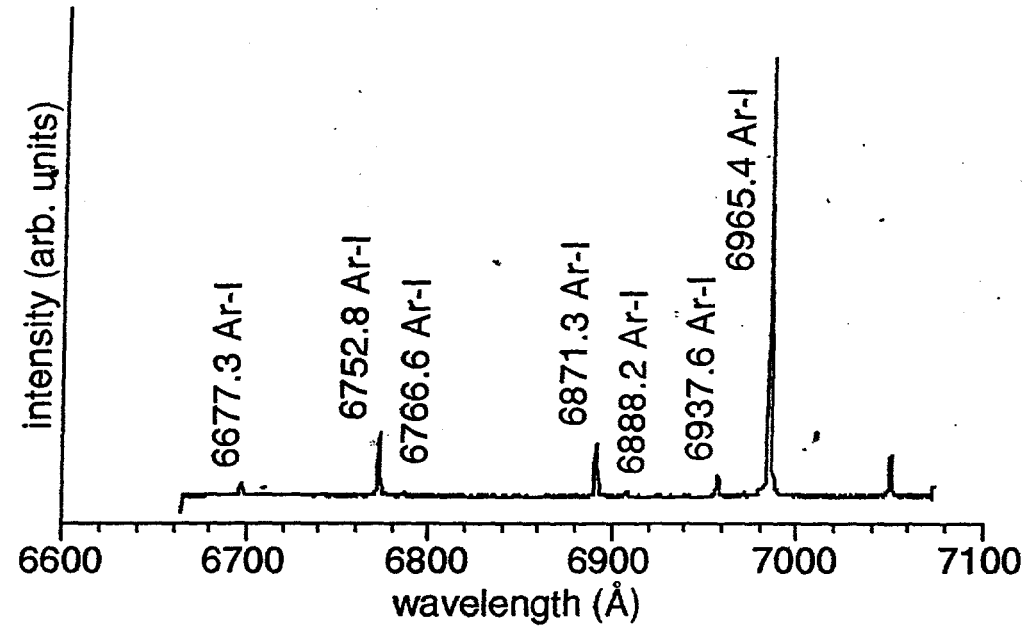

(a)

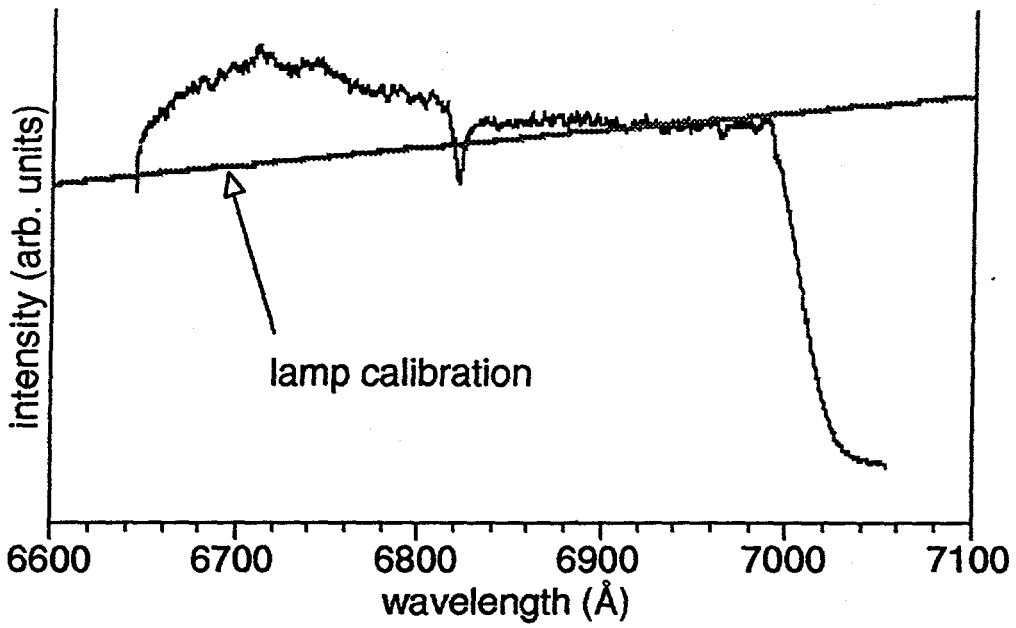

(b)

Figure 4.7. (a) Argon spectrum showing wavelengths of lines used in atomic Boltzmann electron temperature measurements. (b) Spectrum of calibrated lamp source.

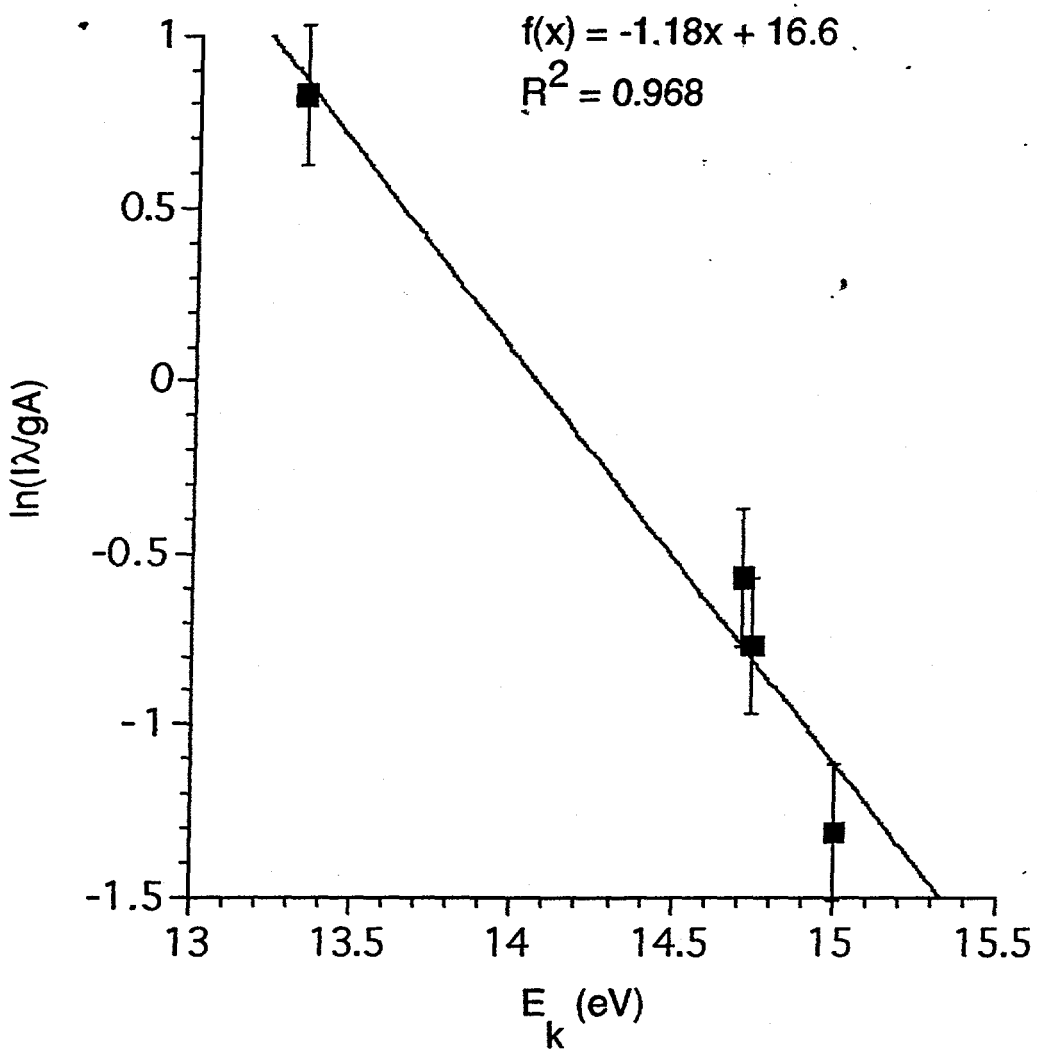

Figure 4.8. Atomic Boltzmann plot of argon emission showing linear fit. This curve indicates a bound electronic temperature of 9800 K (0.85 eV).

Table 4.2. Transition probabilities for argon neutral lines[Wie80]

Wavelength (Å)	E_k (cm^{-1})	E_k (eV)	g_i	g_k	A_{ki} (10^8 s^{-1})
6677.3	108723	13.48	3	1	0.00241
6752.8	118907	14.74	3	5	0.0201
6766.3	121012	15.00	5	3	0.0042
6871.3	118651	14.71	3	3	0.0290
6888.2	120601	14.95	3	5	0.0026
6937.7	118512	14.69	3	1	0.0321
6951.5	120619	14.96	5	5	0.0023
6965.4	107496	13.33	5	3	0.067

~10^{15} cm^{-3} for the electronic temperature to approximate the free electron temperature. Langmuir probe studies indicate a maximum density of about 2×10^{11} cm^{-3}. So in this case, the electronic temperature merely provides a lower bound for the electron temperature, which was found to be 3-4 eV through Langmuir probe. Figure 4.9 is a plot of electronic temperature as a function of input power for an 11 mTorr discharge. These data indicate a slightly higher electronic temperature for argon-only discharges than for discharges which contain lithium carbonate. This may be explained by collisional losses to the heavier component and energy needed to dissociate the Li_2CO_3.

4.4 Behavior of discharge with lithium compounds

As evidenced by the spectra, the microwave discharge is a very effective tool for vaporizing and dissociating these lithium-containing compounds. Figures

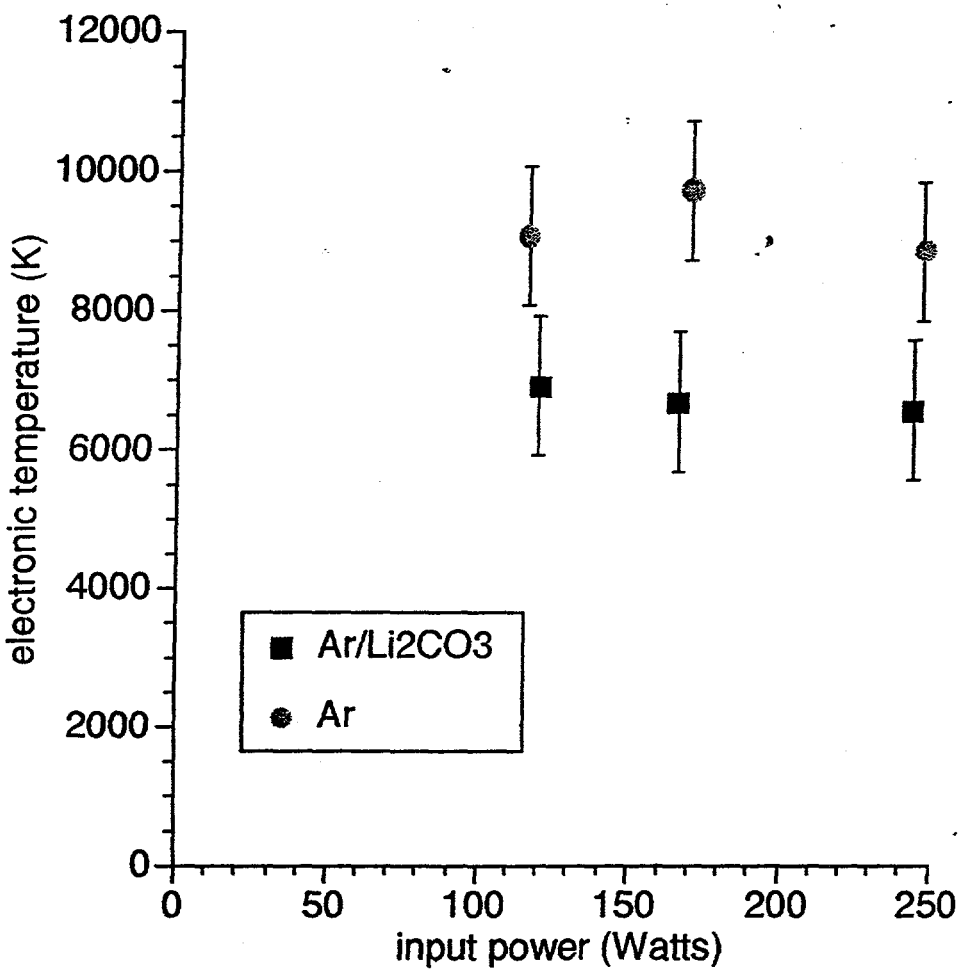

Figure 4.9. Electronic temperature as measured by atomic Boltzmann plots as a function of input power for a discharge of argon partial pressure 11 mTorr. Circles correspond to an argon-only discharge; squares correspond to an Ar-Li_2CO_3 discharge.

4.10 and 4.11 contain spectra of argon/LiCl and argon/Li_2CO_3 discharges, respectively. These spectra were each taken soon after placing 30 mg of the lithium-containing compound into the discharge chamber. (The quartz cup was cleaned with methanol and argon-only discharges between experiments with different compounds.) It was found that LiCl consistently gave a much higher Li-I signal than did Li_2CO_3. The LiCl, however, was used up much more quickly than Li_2CO_3, as seen in Figures 4.12 and 4.13.

Figure 4.12 shows Li-I intensity at 6707.8 Å as a function of time after plasma start-up for an argon/LiCl discharge at 8 mTorr and 185 Watts input power. Figure 4.13 is a similar plot for an argon/Li_2CO_3 discharge at 13 mTorr and 170 Watts. Note that these spectra were taken with the same optical system so that the intensities can be directly compared. As seen in the plots, the Li-I intensity increases gradually after the discharge is ignited and as the compound is heated, vaporized and finally decomposed. LiCl released more lithium into the discharge, more quickly, than did Li_2CO_3. The lithium intensity, however, begins to decrease again after a few minutes of run time. Li_2CO_3 released less lithium, but at a more constant rate.

Because it released more lithium into the system, LiCl was chosen as the compound to continue the lithium plasma studies. It was found that after several months of running lithium discharges, the cavity discharge chamber became conditioned and a more constant amount of lithium could be maintained in the discharge at constant power and pressure. The amount of lithium did decrease with time between "refueling" and was monitored with optical emission spectroscopy.

Figures 4.14 and 4.15 contain plots of the Li-I at 6707.8 Å to Ar-I at 6752.8 Å intensity ratio as a function of discharge pressure. Figure 4.14 (a) is a sample spectrum from which the ratio data was taken for a low lithium

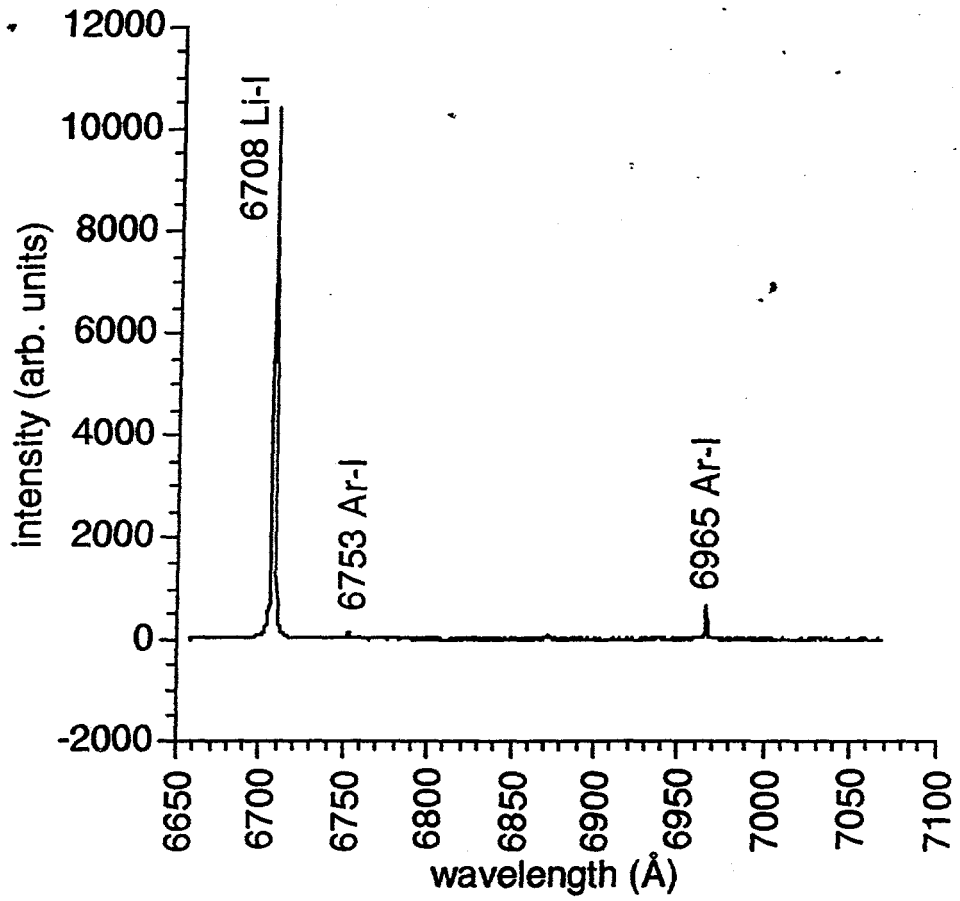

Figure 4.10. Spectrum of an argon/LiCl discharge at 10 mTorr argon partial pressure and 155 Watts input power. 30 mg LiCl was contained in the discharge chamber.

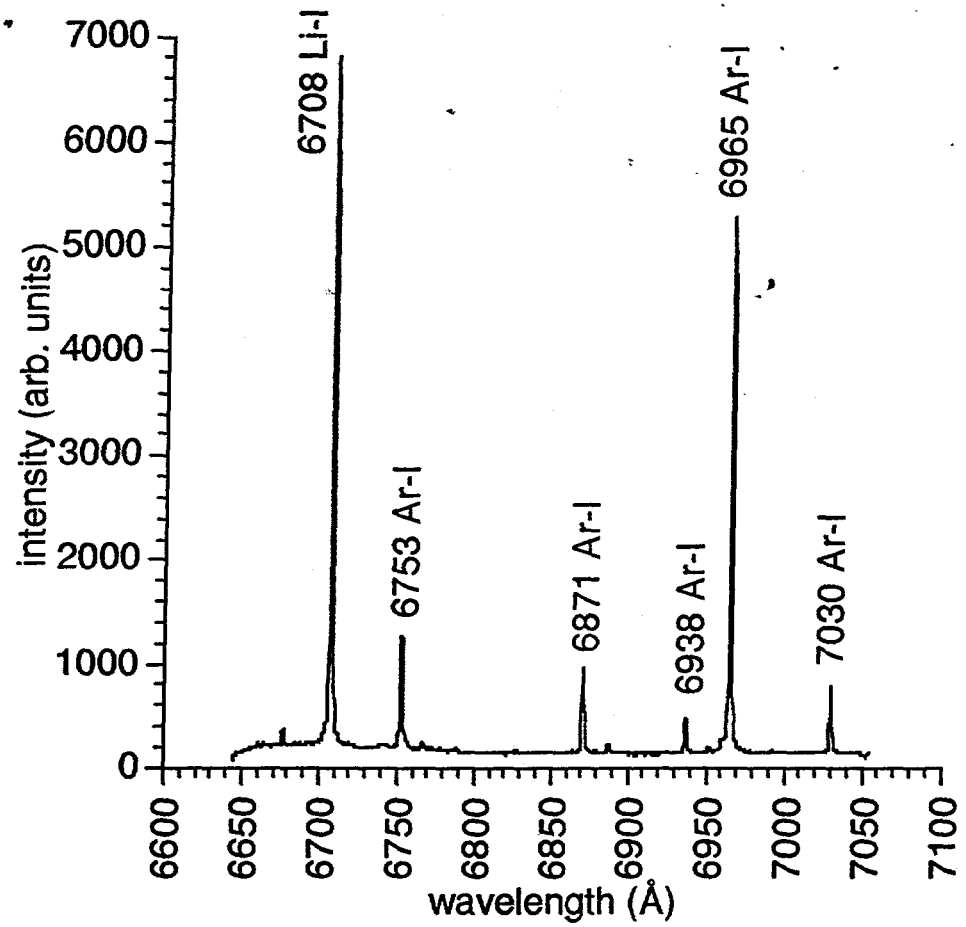

Figure 4.11. Spectrum of an argon Li_2CO_3 discharge at 9 mTorr argon partial pressure and 143 Watts input power. 30 mg Li_2CO_3 was contained in the discharge chamber.

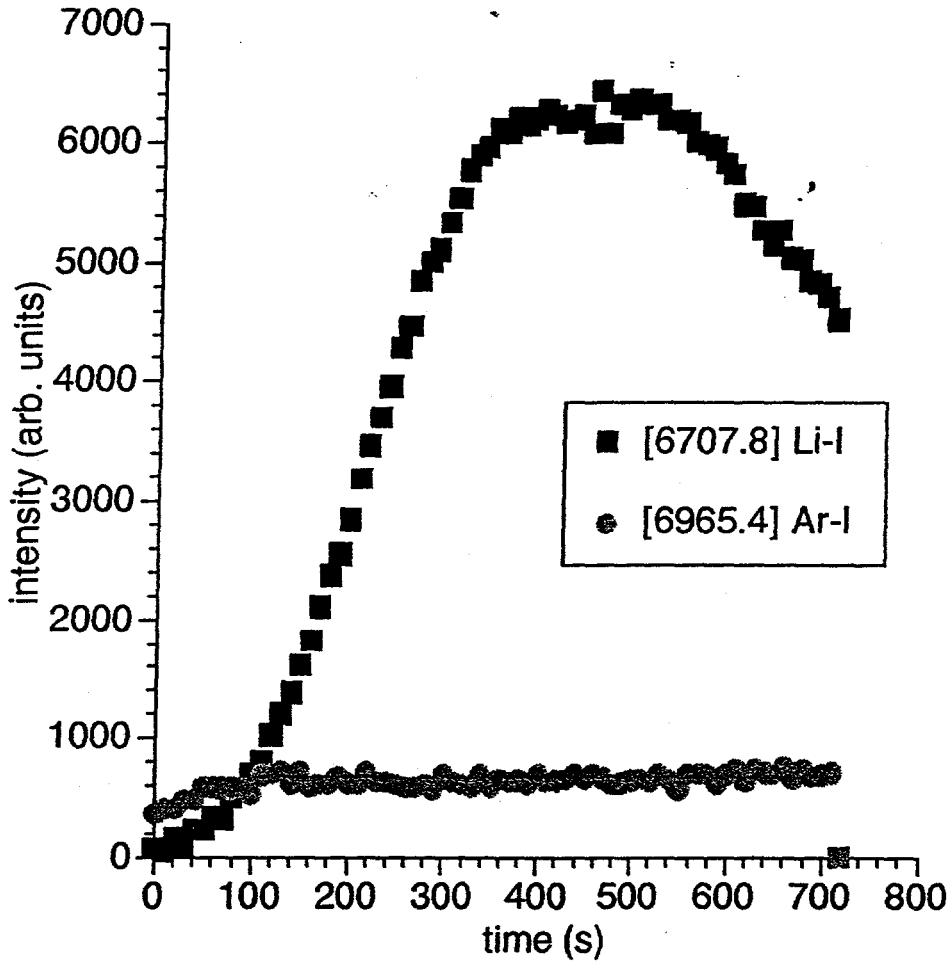

Figure 4.12. Neutral lithium intensity at 6707.8 Å and neutral argon intensity at 6965.4 Å as a function of time since discharge start-up for an argon/LiCl plasma. Discharge pressure is 8 mTorr and input power is 185 Watts.

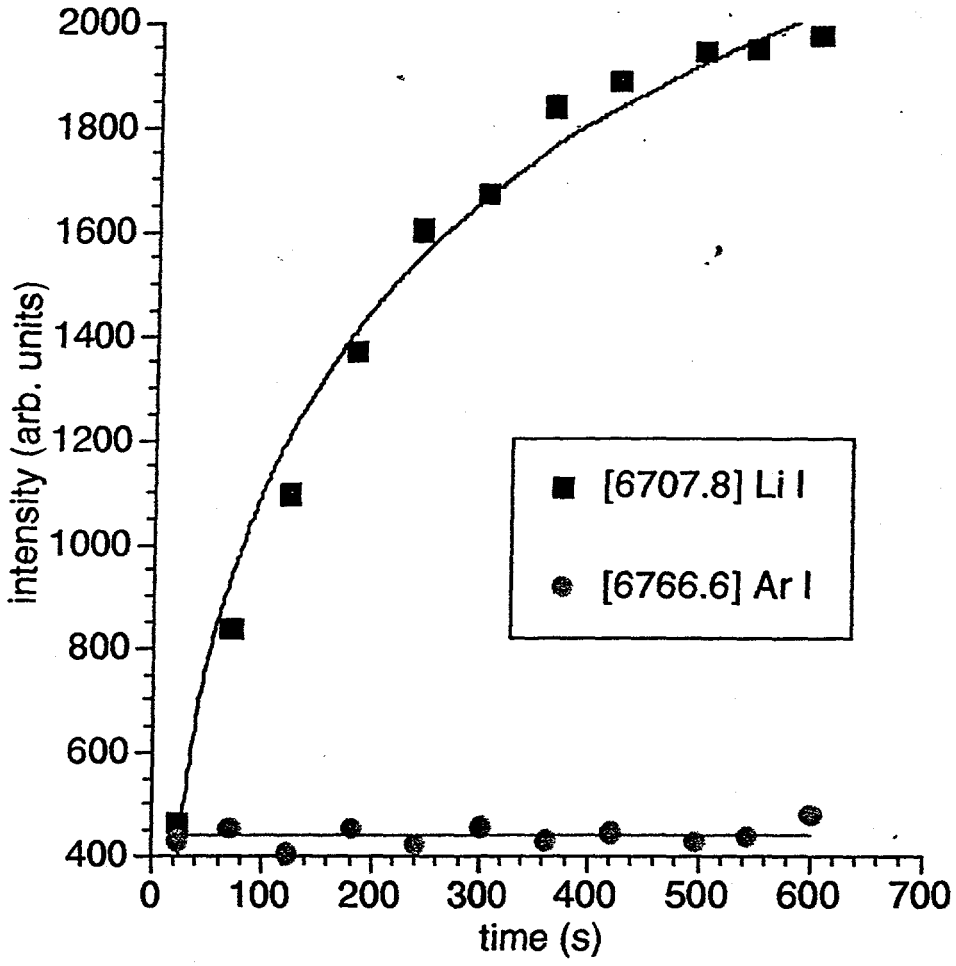

Figure 4.13. Neutral lithium intensity at 6707.8 Å and neutral argon intensity at 6766.6 Å as a function of time since discharge start-up for an argon/Li_2CO_3 plasma. Discharge pressure is 13 mTorr and input power is 170 Watts.

discharge. It is estimated that less than one milligram of LiCl remains in the discharge chamber after ten hours of run time, based on measurements of the solid matter remaining in the quartz cup. Figure 4.15 (a) is a spectrum of an argon/LiCl discharge immediately after refueling with approximately 10 mg LiCl. As surmised from the vertical scale, the lithium emission increases dramatically (over a factor of 500) with the addition of more LiCl. Figures 4.14 (b) and 4.15 (b) indicate that the proportion of lithium increases with decreasing discharge pressure for both the low-LiCl and high-LiCl case. This is not surprising because the discharge pressure is controlled by raising or lowering the argon flow into the chamber.

4.5 Biased collector plate

Biased collector plate measurements were taken for discharge pressures ranging from 1.5 mTorr to 25 mTorr and input powers of 89 Watts to 147 Watts. A sketch of the experimental configuration is given in Figure 4.16. A circular aluminum plate of diameter 7.5 cm replaced the Langmuir probe tip of the probe feedthrough system (see section 3.2). The plate was biased with respect to the vacuum vessel using an Hewlett-Packard model HP6218B 60 V/200 mA dc voltage supply. The current collected by the plate was measured using a battery-operated Triplett model 355C digital multimeter. Figure 4.17 shows a typical voltage-current characteristic for the biased collector plate measurements. The ion saturation region is reached at an applied voltage of about -15 V.

Figures 4.18 to 4.20 are plots of ion saturation current as a function of discharge pressure for different downstream positions. Each of these measurements were taken with a plate bias of -40 V, a value well within the ion saturation region. Below 15 mTorr, the current collected decreases with

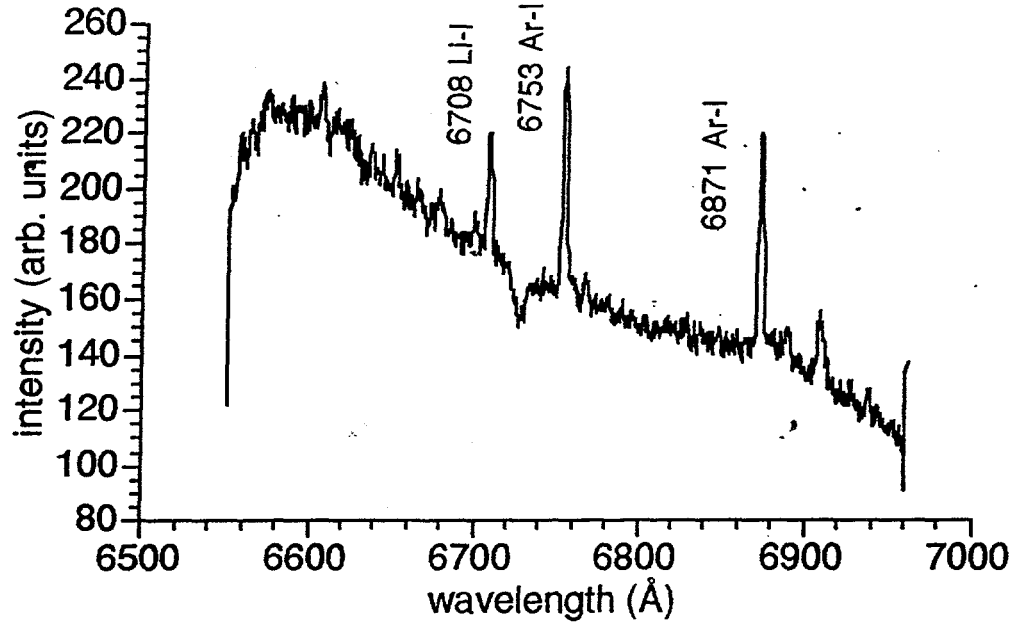

(a)

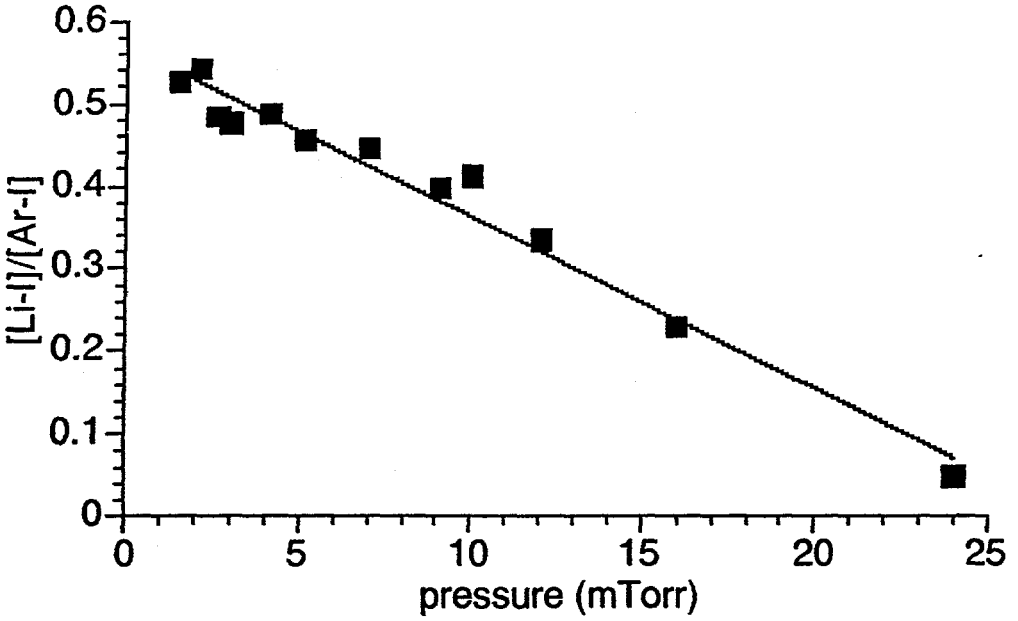

(b)

Figure 4.14. (a) Argon/LiCl spectrum of 7 mTorr discharge at 147 Watts input power. Less than 1 mg LiCl remains in the system at the time of this spectrum. (b) Lithium/argon line intensity ratio as a function of pressure for above conditions.

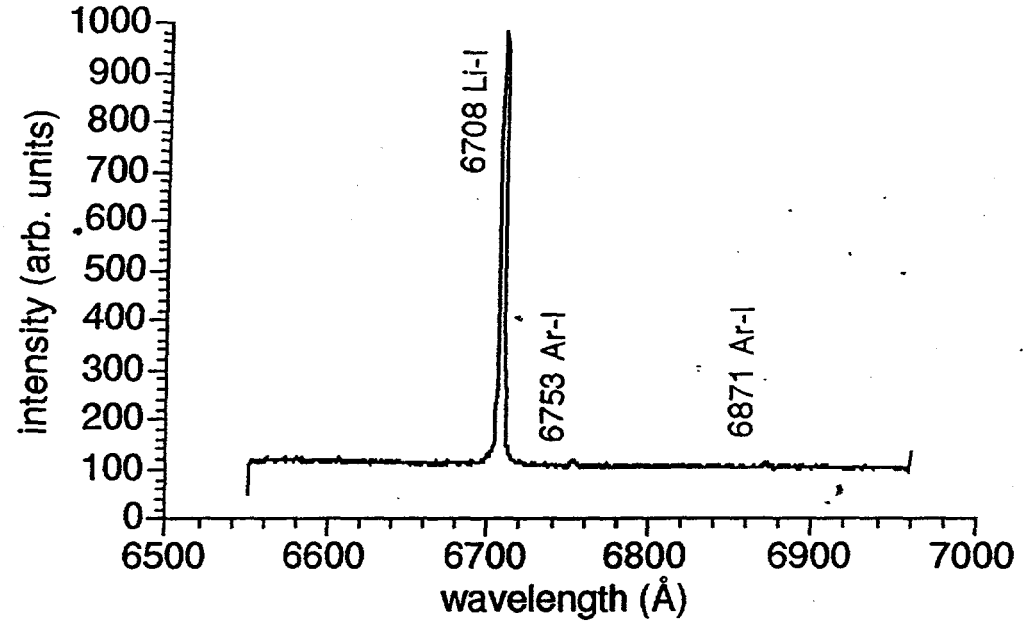

(a)

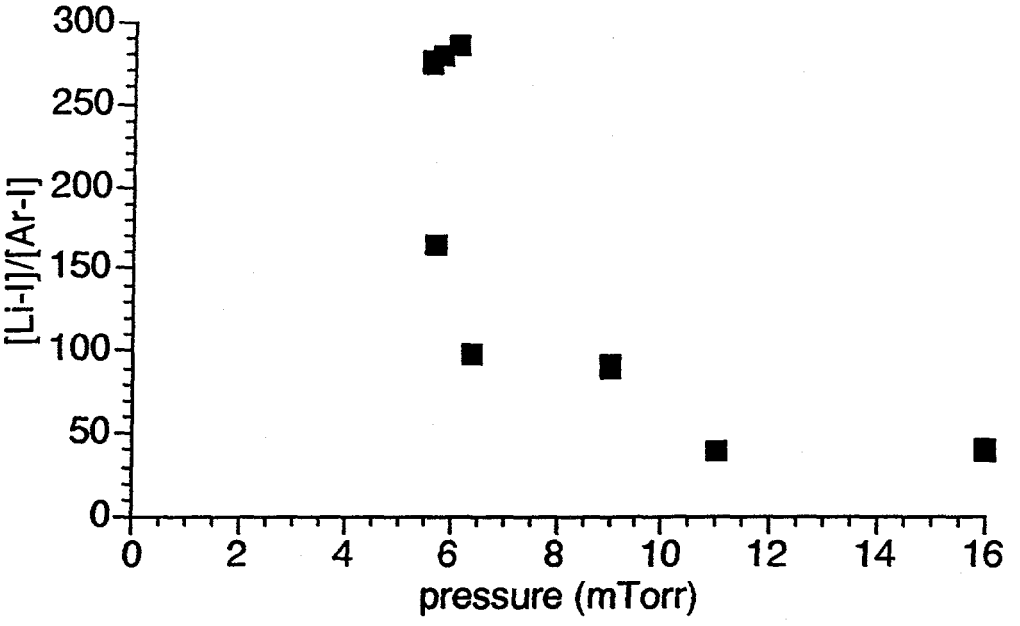

(b)

Figure 4.15. (a) Argon/LiCl spectrum of 6.4 mTorr discharge at 120 Watts input power. 10 mg LiCl had just been introduced in the system at the time of this spectrum. (b) Lithium/argon line intensity ratio as a function of pressure for the above conditions.

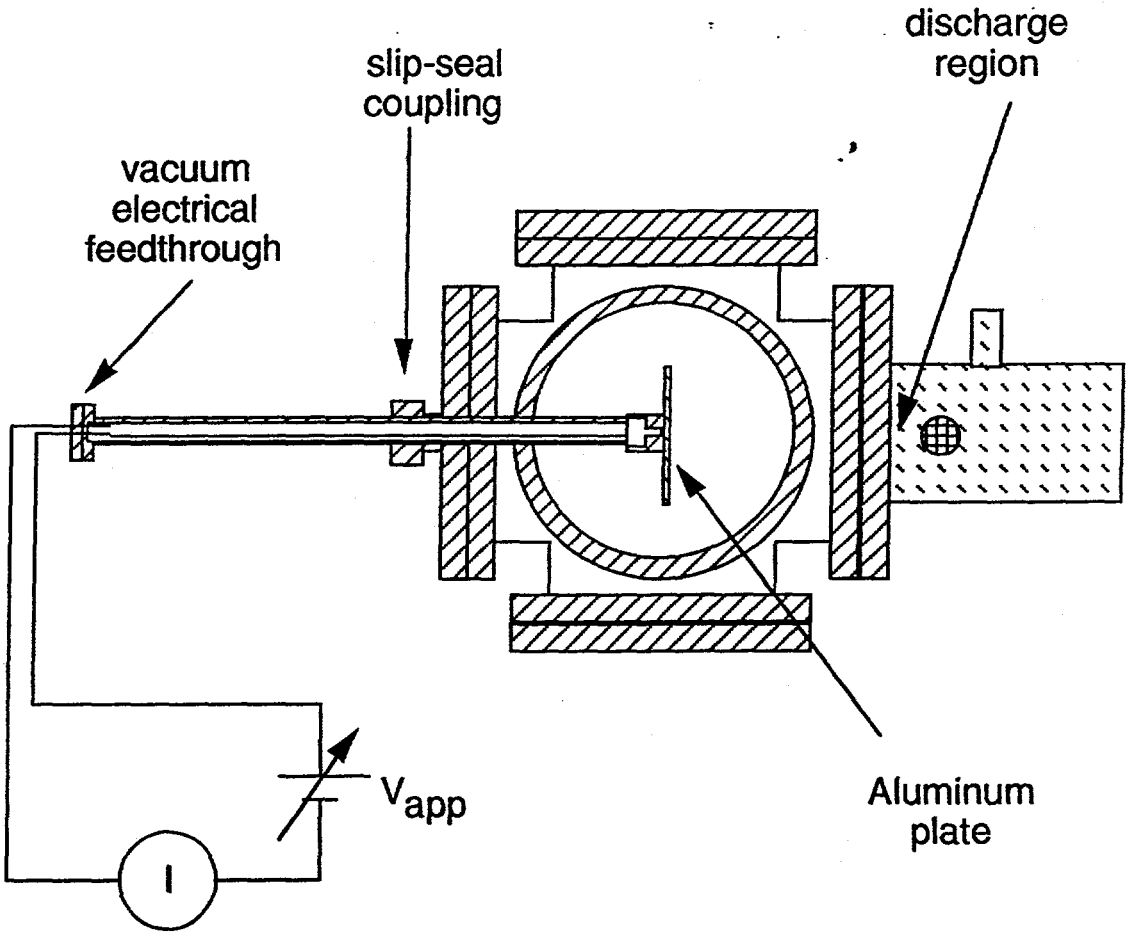

Figure 4.16. Biased collector plate experimental configuration.

increasing discharge pressure. Because the ion density increases with increasing discharge pressure, this region above 15 mTorr must be space charge limited. Space charge limited current is described by the Child-Langmuir law:

$$J_o = \frac{4}{9}\varepsilon_o \sqrt{\frac{2e}{m_e}} \frac{V_o^{3/2}}{s^2} \tag{4.6}$$

where V_o is the bias voltage, m_e is the mass of an electron and e is the electron charge. The sheath thickness, s, is given by[Lie95],

$$s = \frac{\sqrt{2}}{3}\lambda_{De}\left(\frac{2V_o}{T_e}\right)^{3/4} \tag{4.7}$$

where λ_{De} is the electron Debye length, which was found experimentally to vary linearly with the discharge pressure (recall section 3.3 and Figure 3.7). For a constant V_o, the current density will vary as $\frac{1}{(\alpha P + \beta)^2}$, where P is the discharge pressure and α and β are constants which must be fit to the data. This behavior with pressure is seen below 15 mTorr. Above 15 mTorr, the collected current begins a gradual rise corresponding to the increase in charged-particle density.

Figure 4.21 is a plot of saturation current density as a function of distance downstream from the cavity base. The saturation current density decreases exponentially with distance downstream beyond about 7 cm downstream. Closer to the cavity, at 5 cm and below, the saturation current density levels off. The plasma density does not level off in that region, as will be shown in Chapter 5, so this leveling in the current density is probably limited because of space-charge on the large collector plate.

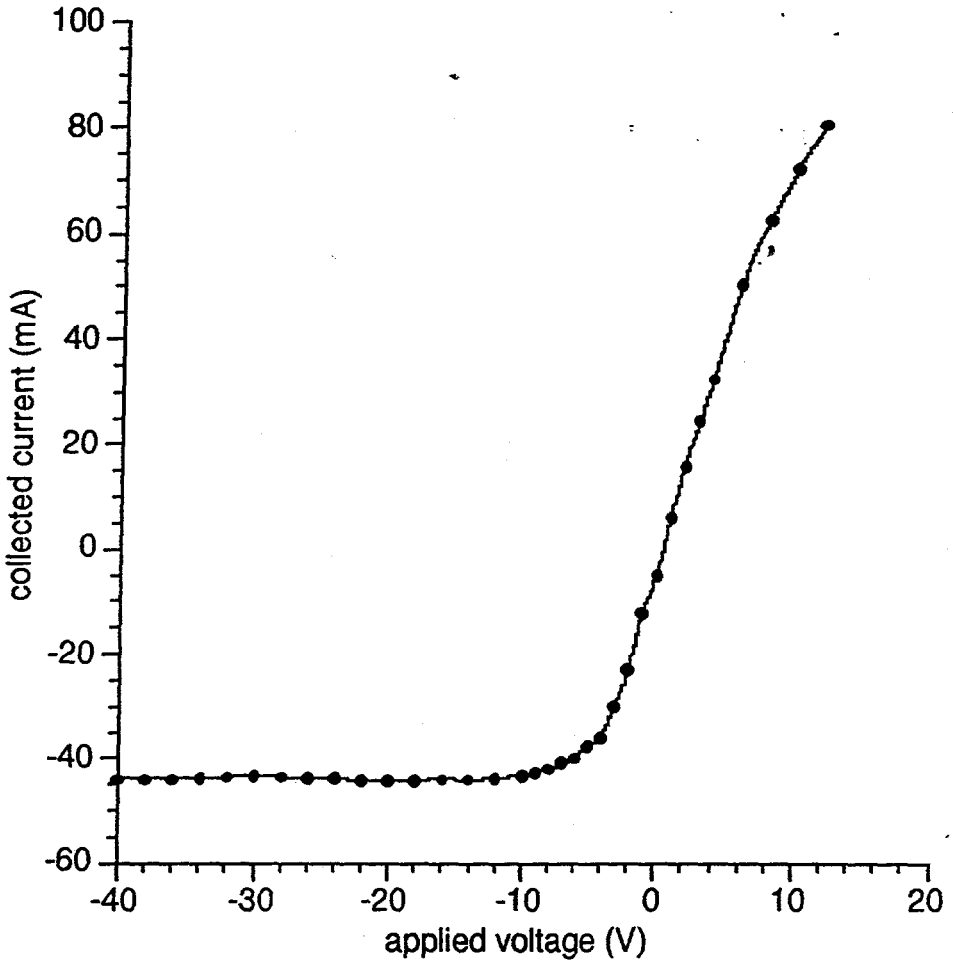

Figure 4.17. Biased collector plate collected current as a function of applied voltage for a discharge at 5.5 mTorr and 170 Watts input power. Plate is located 5.3 cm from base of cavity.

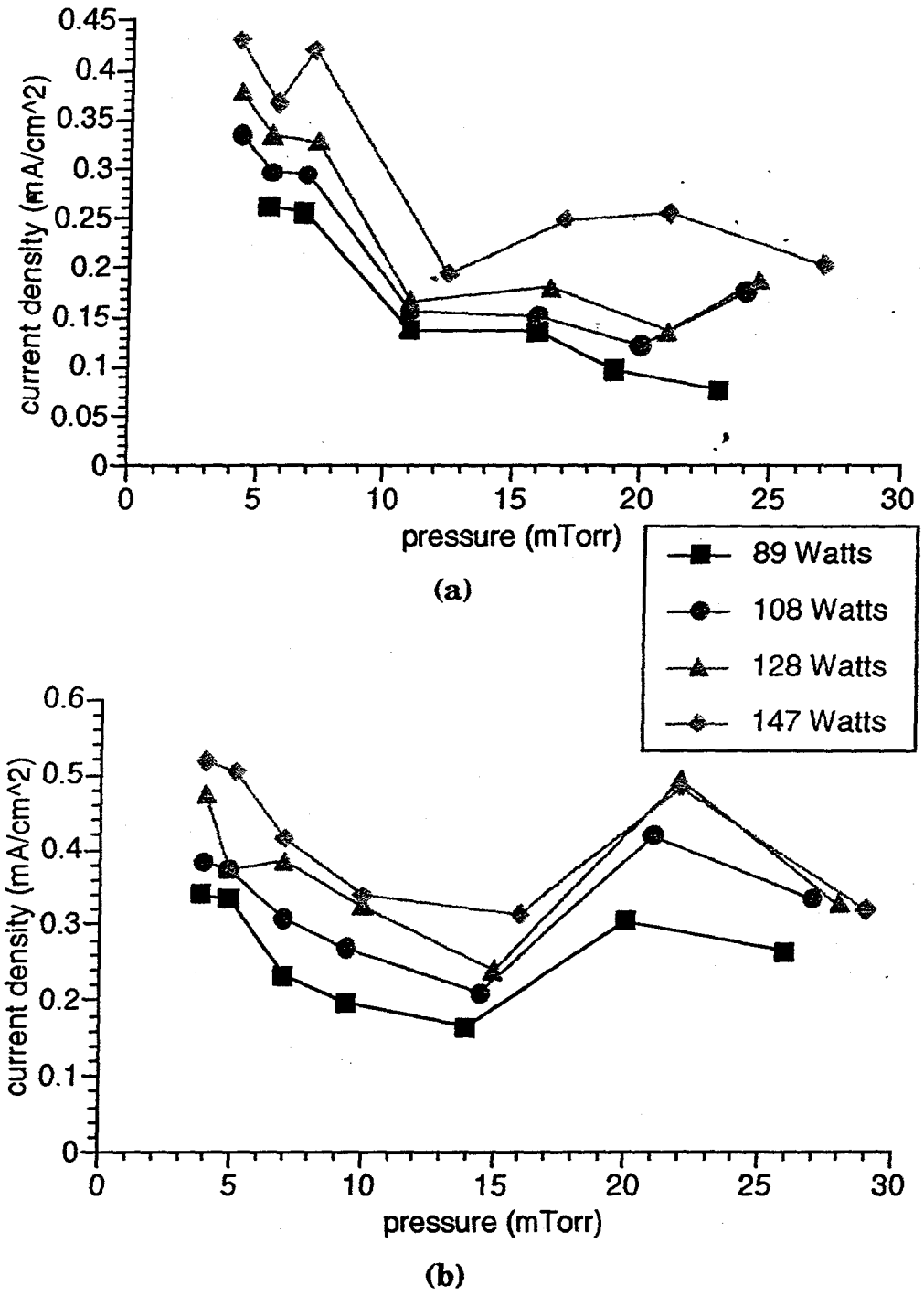

Figure 4.18. Saturation current density collected on a 7.5 cm diameter aluminum plate biased at 40 Volts as a function of discharge pressure. (a) 10.2 cm from base of cavity. (b) 8.4 cm from base of cavity.

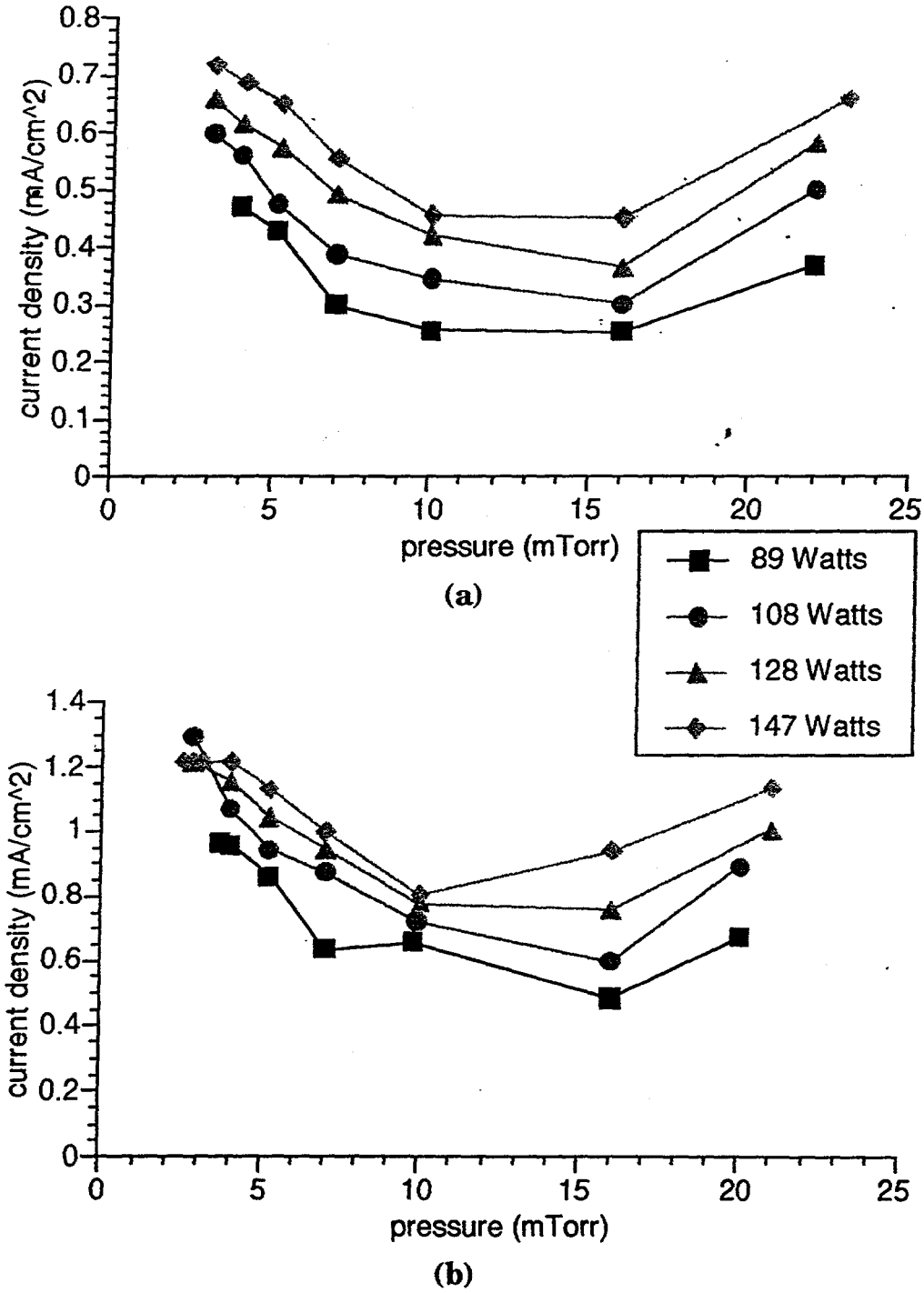

Figure 4.19. Saturation current density collected on a 7.5 cm diameter aluminum plate biased at 40 Volts as a function of discharge pressure. (a) 6.9 cm from base of cavity. (b) 5.4 cm from base of cavity.

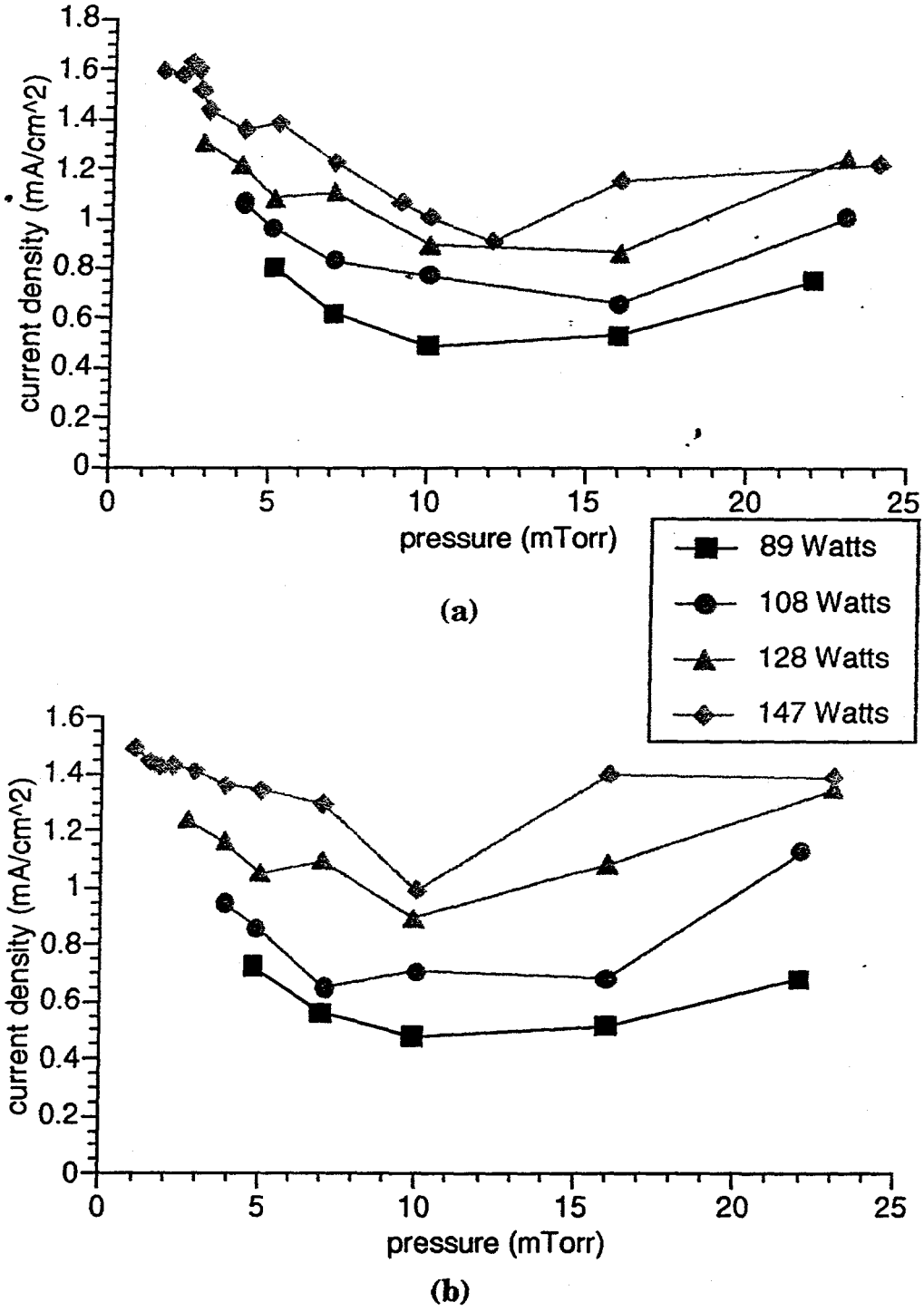

Figure 4.20. Saturation current density collected on a 7.5 cm diameter aluminum plate biased at 40 Volts as a function of discharge pressure. (a) 4.2 cm from base of cavity. (b) 3.5 cm from base of cavity.

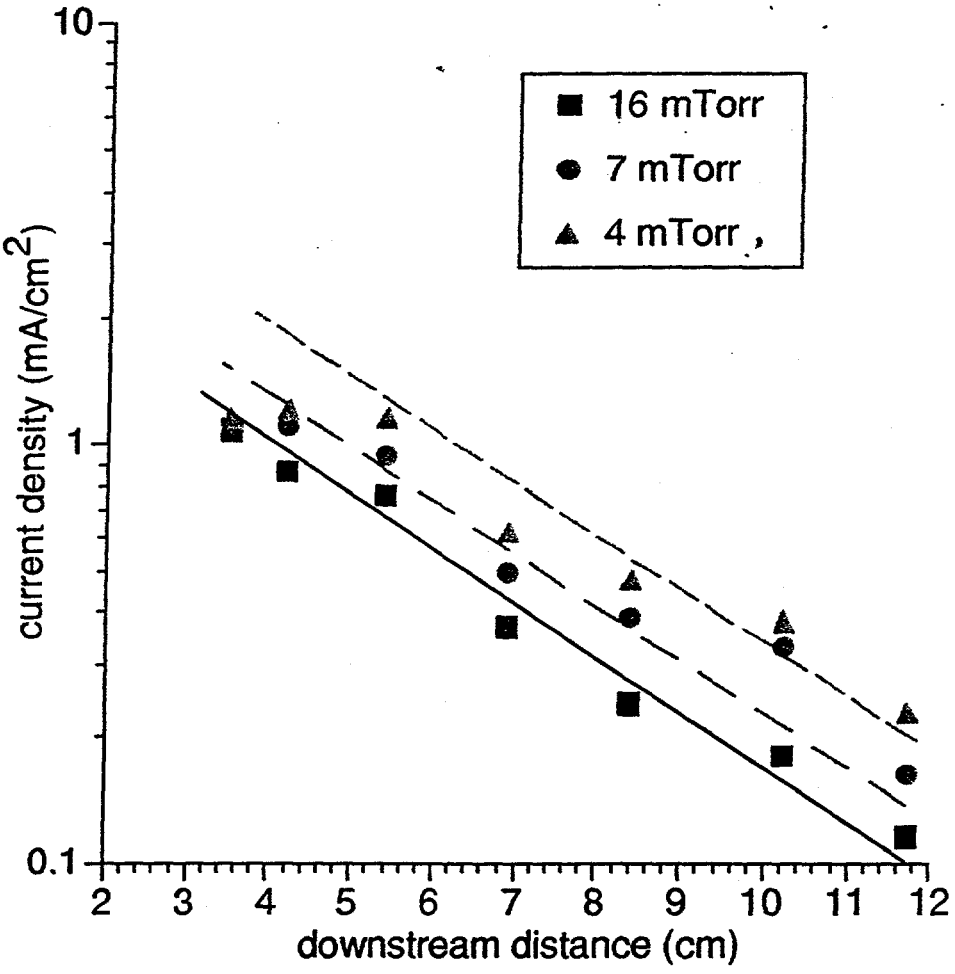

Figure 4.21. Saturation current as a function of downstream distance for a 128 Watt discharge and various discharge pressures. Lines correspond to exponential fits to the data.

CHAPTER 5

LANGMUIR PROBE II: EEDF MEASUREMENTS

A second set of Langmuir probe studies was performed to determine the electron energy distribution function (EEDF) and the density behavior of the discharge as one moves away from the base of the cavity. Because a floating Langmuir probe does not provide EEDFs, a single Langmuir probe setup was used for these measurements. The results of the single Langmuir probe experiments are presented in this chapter. The discharge behavior is also compared with similar plasma sources.

5.1 Single Langmuir probe theory

Biased probe measurements are discussed and equations pertinent to their use are derived in many papers and texts.[Che65,Hut87,Lie95,Sch68] The first author to present the method was Irving Langmuir[Lan23] who used probes to study low pressure, collisionless discharges. A brief outline of Langmuir's method is given below as is a method for determining the electron energy distribution function for an arbitrary electron distribution from a Langmuir probe trace. The EEDF determination method was first presented by Druyvesteyn[Dru30] and is also discussed in the texts cited above.

5.1.1 Electron temperature and plasma density measurements

Consider a small , biased probe immersed within a plasma such that $A_p >> s^2$, where A_p is the area of the probe and s is the sheath thickness.

Three distinct voltage regions can be identified in the current collected by such a probe. If the probe is biased sufficiently negative to collect only ion current, the current collected by the probe of surface area A_p is given by

$$I = - I_i = -en_s u_B A_p \tag{5.1}$$

where n_s is the density at the edge of the sheath formed about the probe. The Bohm velocity u_B is given by

$$u_B = \sqrt{\frac{eT_e}{M_i}} \tag{5.2}$$

for electron temperature T_e and ion mass M_i. Applying the Boltzmann relation, the bulk plasma density can be calculated from $n_s = n_o\, e^{-e\phi_p/k_B T_e} \approx 0.61\, n_o$, namely

$$n_o \approx \frac{0.61}{eA_p}\sqrt{\frac{M_i}{eT_e}}\, I_{si}. \tag{5.3}$$

If the electron temperature is known, then the plasma density can be measured from the ion saturation current, I_{si}.

The electron temperature can be measured by varying the probe voltage and collecting electron current. The density distribution of the electrons, if they are assumed to be Maxwellian, is governed by Boltzmann's relation. For $V_B - \Phi_p < 0$, where V_B is the probe bias voltage and Φ_p is the plasma potential,

$$I + I_i = I_e = I_{se} \exp\left(\frac{e(V_B - \Phi_p)}{k_B T_e}\right), \tag{5.4}$$

where the electron saturation current, I_{se}, is given by

$$I_{se} = \frac{1}{4} e\, n_o\, \bar{v}_e\, A_p = \frac{1}{4} e\, n_o \sqrt{\frac{8eT_e}{\pi m_e}}\, A_p\,. \tag{5.5}$$

Equation 5.4 can be used to determine the electron temperature. Equation 5.5 will also give density if T_e and I_{se} are known. Taking the derivative of the logarithm of equation (5.4), the electron temperature can be determined from:

$$\frac{d\ln(I_e)}{dV} = \frac{e}{k_B T_e}, \text{ for } V_B - \Phi_p < 0. \tag{5.6}$$

These equations make many assumptions about the plasma parameters. The ion density measurements are based on the assumption that the probe diameter is much greater than the sheath thickness ($A_p >> s^2$) so that edge effects can be ignored. The sheath thickness, in turn, is on the order of the Debye length. It was also assumed that the plasma is essentially collisionless. This assumption is met when the collision mean free path (mfp) is larger than the probe radius. These conditions may be summarized by $mfp >> r_p >> \lambda_D$. There is also the assumption that the plasma is infinite and homogeneous in the absence of the probe, and that the electrons and ions follow a Maxwellian distribution.

5.1.2 EEDF measurement

Druyvesteyn[Dru30,Lie95] has shown that an arbitrary electron energy distribution function can be measured using a single, biased, electrostatic probe. For an arbitrary distribution function $f_e(v)$, the electron current, I_e, collected by a probe in the region $(V - \Phi_p) < 0$ is given by the following velocity-space integral:

$$I_e = e A_p \int_{-\infty}^{\infty} dv_x \int_{-\infty}^{\infty} dv_y \int_{v_{min}}^{\infty} dv_z \, v_z \, f_e(v) \tag{5.7}$$

where the minimum electron velocity is given by the minimum electron energy required for an electron to cross the sheath potential. Thus

$$v_{min} = \sqrt{\frac{2e(\Phi_p - V_B)}{m_e}}, \tag{5.8}$$

where V_B is the voltage between the probe and ground. Transforming to spherical coordinates and integrating over ϕ and θ, the electron current is found to be the single integral

$$I_e = \pi e A_p \int_{v_{min}}^{\infty} dv\, v^3 \left(\frac{v_{min}^2}{v^2}\right) f_e(v). \tag{5.9}$$

Making a change of variables to $E = \frac{1}{2} m_e v^2/e$ and differentiating with respect to $V = \Phi_p - V_B$,

$$\frac{dI_e}{dV} = -\frac{2\pi e^3}{m_e^2} A_p \int_{V}^{\infty} dE\, f_e\left(\sqrt{\frac{2eE}{m_e}}\right). \tag{5.10}$$

Differentiating again,

$$\frac{d^2 I_e}{dV^2} = \frac{2\pi e^3}{m_e^2} A_p\, f_e\left(\sqrt{\frac{2eV}{m_e}}\right) \tag{5.11}$$

The electron energy distribution function, $g_e(E)$, is related to the electron velocity distribution function by $g_e(E)\, dE = 4\pi v^2 f_e(v)\, dv$, so that

$$g_e(E) = \frac{2m_e}{e^2 A_p} \sqrt{\frac{2e}{m_e}} \sqrt{V} \frac{d^2 I_e}{dV^2} \tag{5.12}$$

Thus the electron energy distribution function can be determined by taking the second derivative with respect to voltage of the current collected by a probe immersed in a plasma. The integration of equation (5.7) was made with the assumption that the plasma is isotropic. For this reason, this technique will not be valid within the ECR region, but will be useful below the cavity outside the magnetic field region.

5.2 Experimental technique

The experimental setup for the single Langmuir probe measurements is shown in Figure 5.1. The electron density, ion density, electron temperature, and EEDF measurements presented in this chapter were made using the Plasma Probe Data Acquisition System manufactured by the Plasma Physics Research Group at Dublin City University, Ireland.[PPR94] This computerized system sweeps the probe within the range -60 V to +60 V, and measures the current collected by the probe. A typical probe current-voltage characteristic is given in Figure 5.2. An interactive computer program calculates many plasma parameters from the collected data. The program first calculates the floating potential and electron saturation current. The electron temperature is then calculated from a least squares fit to the electron collection region described above. The electron energy distribution function is found by taking the second derivative of the data numerically. Further details about the Plasma Probe Data Acquisition System can be found in reference [PPR94].

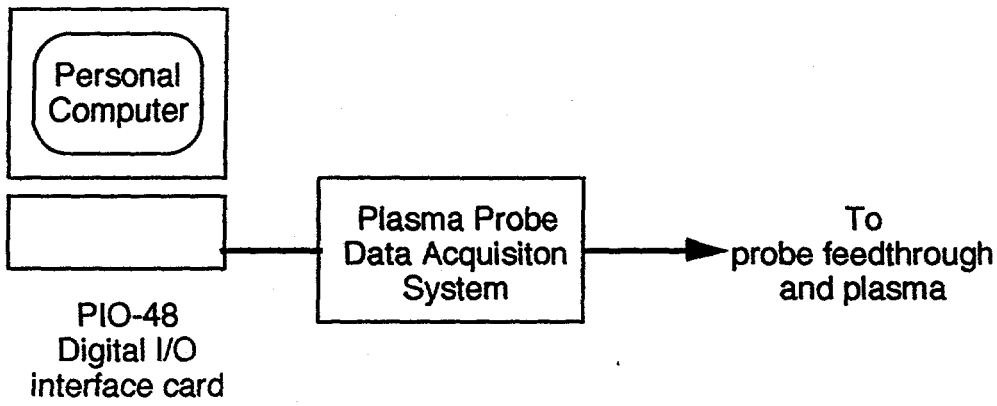

Figure 5.1. Experimental setup for the single Langmuir probe experiments.

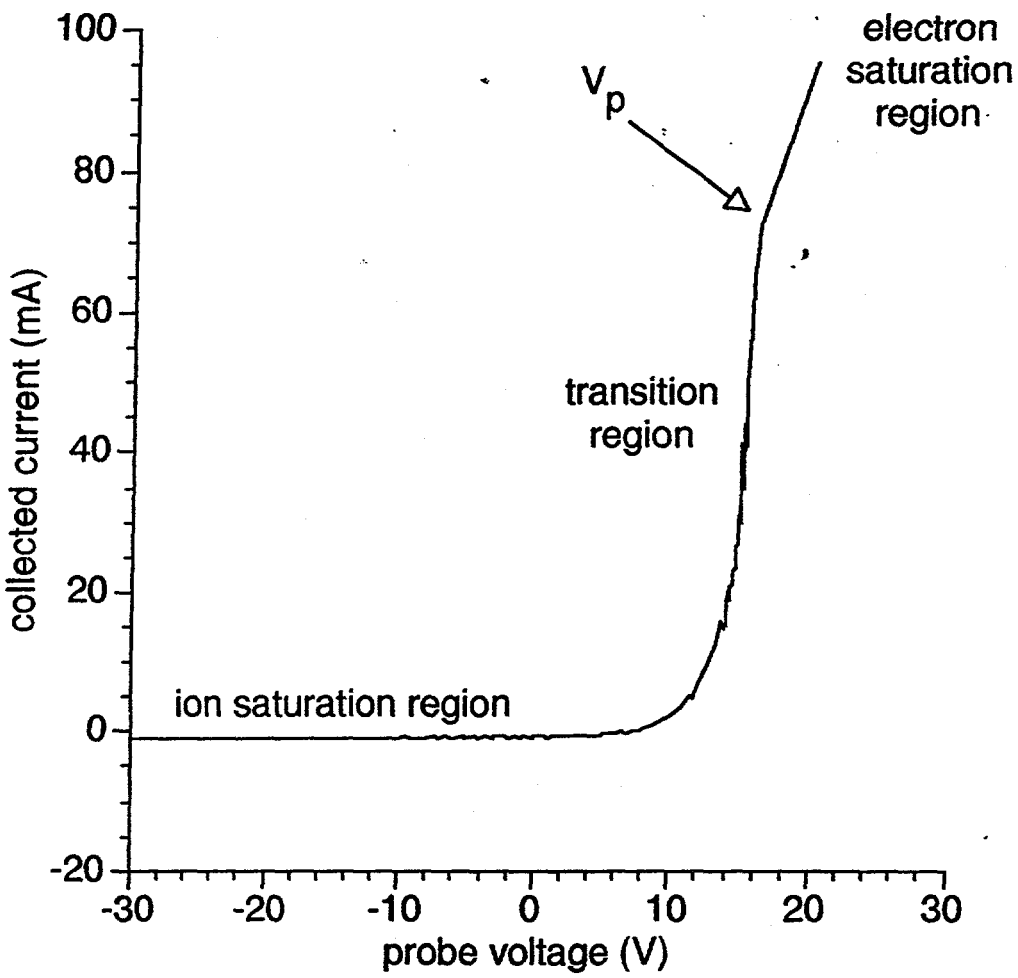

Figure 5.2. Typical probe current-voltage characteristic for the single Langmuir probe experiment. This 135 Watt, 21 mTorr discharge has an electron temperature of 1.5 eV and electron density of 2.3×10^{11} cm^{-3} at the base of the cavity.

The probe circuitry was connected to the plasma using the same feedthrough drawn in Figure 3.2. The probe tip was 0.38 mm diameter tungsten wire with length 7.9 mm extending into the plasma. The remainder of the wire is shielded from the plasma by alumina tubing. The total probe area is then 9.53 mm^2.

5.3 Density and temperature measurements

5.3.1 Decay of electron density

Ambipolar diffusion has been observed to account for the electron density decay in microwave resonant cavity discharges. Sanborn Brown[Bro59] reports decay by ambipolar diffusion in a helium microwave resonant cavity, as do Hopwood and Asmussen[Hop90] for argon resonant cavity discharges. For constant particle velocity, ambipolar diffusion is governed by[Che84]

$$n(x) = n_o e^{-x/x_o}, \tag{5.13}$$

where n_o is the plasma density at the source and x_o is a characteristic diffusion length. Thus, if a semi-logarithmic plot of the electron density is linear, diffusion dominates particle loss.

Another common mechanism for particle loss is recombination of electrons with ions. Under steady state electron-ion recombination, the plasma density n is governed by the following differential equation:

$$\frac{\partial n}{\partial t} = \nu_i n - \alpha n^2 - D \nabla^2 n = 0, \tag{5.14}$$

where ν_i is the ionization coefficient, α is the recombination coefficient, and D is the ambipolar diffusion constant. In one dimension, equation 5.14 can be rearranged to give the following equation for n:

$$\frac{d^2 n}{dx^2} + \frac{\alpha}{D} n^2 - \frac{\nu_i}{D} n = 0. \tag{5.15}$$

5.3.2 Experimental measurements

The electron and ion densities of the discharge as a function of distance downstream from the base of the cavity is plotted in Figure 5.3 for 20 mTorr and Figure 5.4 for 4.5 mTorr. Both discharges have an input power of 125 Watts. The electron density is observed to decrease exponentially with distance away from the cavity base from a maximum of 2.5×10^{11} cm^{-3} for the 19 mTorr discharge. This same density behavior with downstream distance was reported by Hopwood, et. al.,[Hop90] in a similar, but larger, source and is attributed to ambipolar diffusion. In a compact multipolar ECR ion source, Srivastava, et. al.,[Sri94] report the same exponential decay of plasma density away from the cavity base. Srivastava's source had a peak density of 4.5×10^{11} cm^{-3} for a 1.5 mTorr discharge in argon. This value is larger, but still comparable, with the peak density in this source at 4.5 mTorr.

In the lower pressure discharge shown in Figure 5.4, the density decays exponentially to a downstream distance of about 4 cm. After 4 cm downstream, the density strays from this exponential decline and begins to decrease inversely with distance. In this region, the density decay can be attributed partially to recombination rather than diffusion. Most likely, a combination of diffusion and recombination are causing the plasma decay away from the cavity base.

The ion densities determined from the single Langmuir probe experiments compare favorably with those reported in Chapter 3 from double Langmuir probe experiments. From Figure 3.4, with the probe 3.5 cm downstream from the base of the cavity, the ion density at 115 W input power and 20 mTorr discharge pressure was approximately 7×10^{10} cm^{-3}. At 4 mTorr discharge pressure and the same location, an ion density of

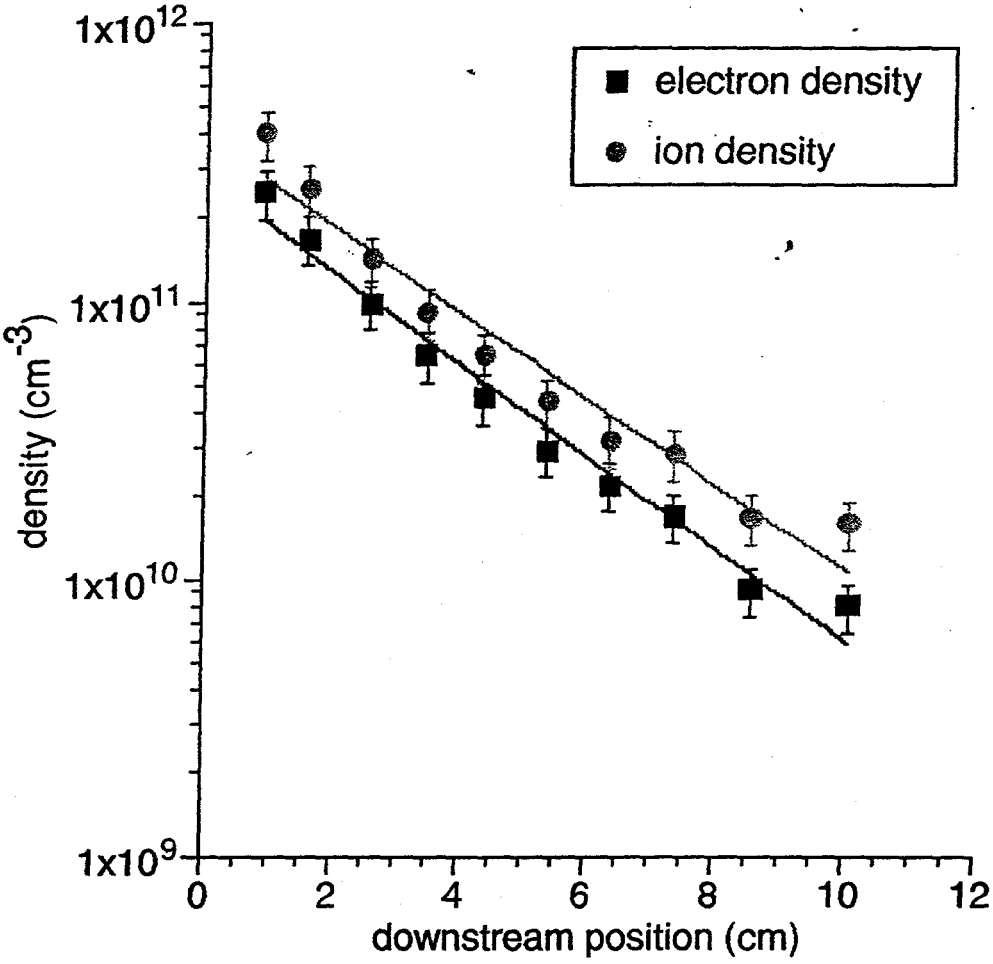

Figure 5.3. Electron and ion density as a function of downstream position for a 19 mTorr discharge with 125 Watts of input power. Lines are an exponential fit to the data.

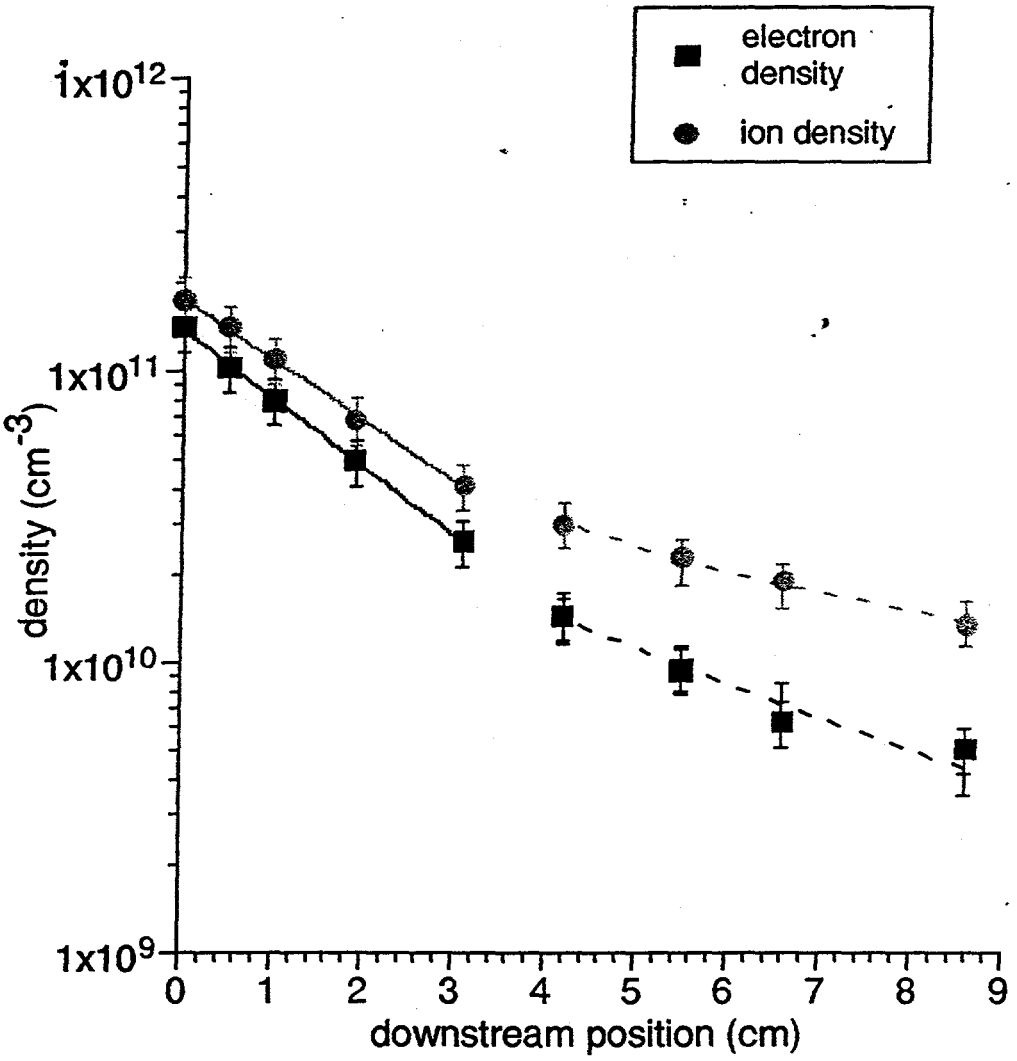

Figure 5.4. Electron and ion density as a function of downstream position for a 4.5 mTorr discharge with 125 Watts of input power. Solid lines represent an exponential fit of the data. Dashed lines are a fit to the function $n_e = a/x + b$.

3.5×10^{10} cm^{-3} was measured for 115 Watts input power. These are comparable to the values measured with the single probe with 125 Watts input power at 3.5 cm downstream, where the ion densities are 6.5-9.0 x 10^{10} cm^{-3} for 19 mTorr and 3-4 x 10^{10} cm^{-3} for 4.5 mTorr.

In Figure 5.5, the plasma potential is plotted as a function of downstream distance from the cavity for a (a) 19 mTorr and (b) 4.5 mTorr discharge with 125 Watts input power. The plasma potential decreases linearly with distance, behavior also reported by Hopwood, et. al.,[Hop90] in their similar source. At 20 mTorr, the plasma potential drops off from a peak of 17 Volts at the base of the cavity. The plasma potential at the base of the cavity is 23 Volts for the 4.5 mTorr discharge, but drops off much more rapidly with distance.

In Figure 5.6, the electron Debye length is plotted as a function of discharge pressure and is observed to decrease linearly with pressure as in Figure 3.7. The maximum Debye length observed, at 4.5 mTorr, was 0.004 cm which is much smaller than the probe radius of 0.02 cm, satisfying the condition discussed in section 5.2.1.

Also of interest is the collision mean free path (mfp), given by[Che84]

$$\lambda_{ei} \approx 3.4 \times 10^{13} \frac{T_e^{\,2}}{n \ln \Lambda} [cm] \qquad (5.13)$$

where the electron temperature, T_e, is in electron volts and the density, n, is in cm^{-3}. The term ln Λ, Spitzer's impact parameter, is taken to be 10.2 for this discharge.[Che84] The mean free path is a measure of the typical distance a particle must travel before encountering a collision. Also in Figure 5.6, the collision mean free path is plotted as a function of discharge pressure. These values were taken at the base of the cavity (downstream distance = 0) for a

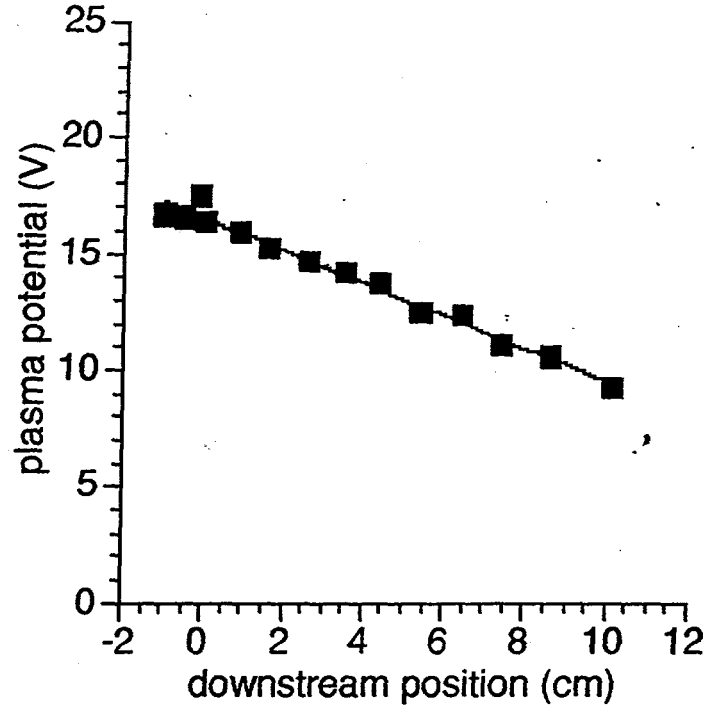

(a)

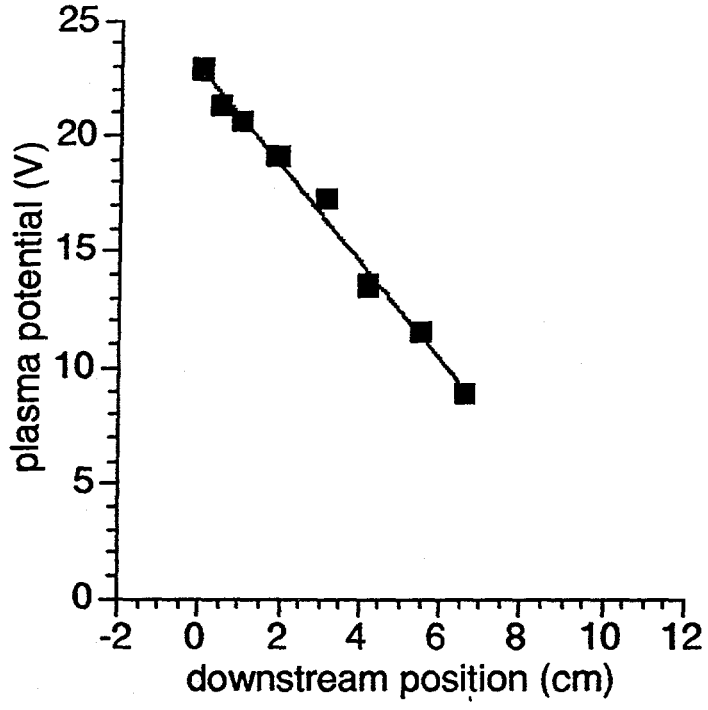

(b)

Figure 5.5. Plasma potential as a function of downstream position for (a) 20 mTorr and (b) 4.5 mTorr discharges at 125 Watts.

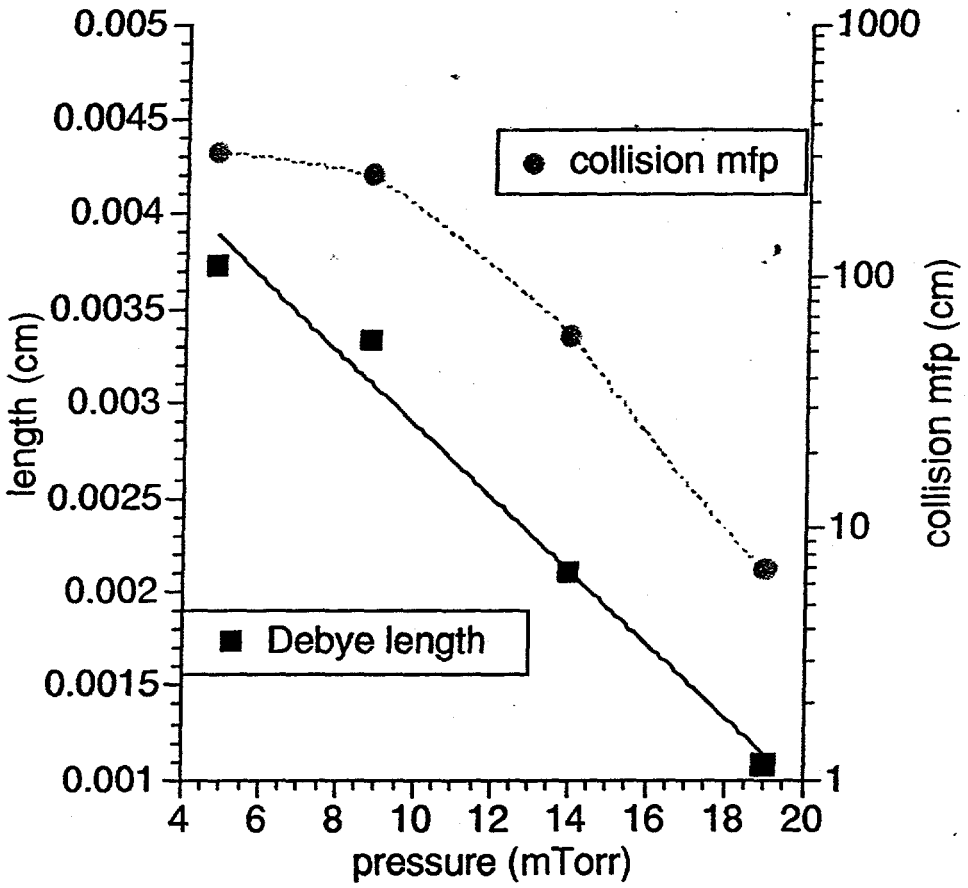

Figure 5.6. Electron Debye length and collision mean free path as a function of discharge pressure in a 125 Watt discharge.

discharge power of 125 Watts. As shown in the plot, the collision mean free path decreases rapidly with increasing discharge pressure, i.e., the discharge becomes more collision-dominated as the pressure is increased. The mfp at pressures below about 12 mTorr is on the order of hundreds of centimeters. At a pressure of about 20 mTorr, the mean free path is on the order of a few centimeters, closer to the dimensions of the discharge chamber. As required by the assumptions for Langmuir probe theory, the collision mean free path remains much larger than the probe size.

5.4 Electron energy distribution functions

The electron energy distribution function (EEDF) is often assumed to be Maxwellian for both experimental measurements (such as Langmuir probe) and plasma modeling. Many sources[Mah89,Hop90,Ged92] have indicated that ECR discharges do not, indeed, follow a Maxwellian electron distribution. Hopwood, et al.,[Hop90] report a distribution which falls below a Maxwellian distribution in the high energy region. Heidenreich, et al. [Hei88] found the EEDFs of oxygen microwave plasmas to fall between the Maxwellian and Druyvesteyn distributions, which are defined below. Moisan and Wertheimer[Moi93] have modeled the effect of high-frequency fields on the EEDF of argon discharges and have found that electrons fall below the Maxwellian distribution in the high energy region and have a lower average electron energy than dc discharges under the same pressure-discharge size conditions.

The Maxwellian distribution is given analytically by

$$f_{e,M}(E) = a\sqrt{E}\, e^{-E/T_{eff}} \qquad (5.14)$$

and the Druyvesteyn by

$$f_{e,D}(E) = a\sqrt{E}\, e^{-(\beta E/T_{eff})^2}. \tag{5.16}$$

For the same average temperature, the Maxwellian distribution has more high energy particles than does a Druyvesteyn distribution. The effective temperature, T_{eff} is defined to by $\langle E \rangle = \frac{3}{2} k_B T_e$ where

$$\langle E \rangle = \int_0^\infty E\, f_e(E)\, dE \tag{5.17}$$

is the average energy. The distribution functions must also be normalized to one. If these normalizations are performed, β in equation (5.16) is calculated to be[Hei88] $\beta \approx 0.54$.

In the EEDFs to follow, distributions are shown which have been fitted to the experimental data. The curve fits were performed by the curve fitting routine within the DeltaGraph Pro® software package by Deltapoint, Inc. This package allows the user to define a functional model with variable parameters, which are calculated in an iterative least squares fit. For more details about the curve fitting package, see reference [Del93].

5.5 Experimental EEDFs

Figure 5.7 contains the electron energy distribution function at the base of the cavity for a 14 mTorr discharge. Several theoretical distributions are shown along with the experimental data. The best fit, as determined by the curve fitting routine described above, occurs for a Druyvesteyn distribution with an average energy $\langle E \rangle = 5.3$ eV. A Maxwellian fit of the data with average energy as a parameter received the best fit for $\langle E \rangle = 4.3$ eV. This fit gave more high energy electrons than were measured by the experiment. A Maxwellian with $\langle E \rangle = 5.3$ eV is shown as well for comparison to the Druyvesteyn distribution. This distribution greatly exceeds the number of high energy electrons.

One explanation for the absence of high energy electrons outside the ECR region is that they may be trapped by the magnetic multicusp. The magnetic field cusps (recall Figure 2.3) act as curved magnetic mirrors, trapping those electrons moving parallel to the field lines. As with any magnetic mirror, those particles with lower energy are lost more rapidly from the mirror than those with higher energies, resulting in an EEDF which falls below the Maxwellian distribution for energetic particles. In addition to the ECR region, the presence of the strong high-frequency microwave field affects the EEDF.

If the high energy electrons are indeed trapped in the magnetic multicusp, the EEDF should become more Maxwellian as the collision frequency increases. That does occur in this discharge as illustrated by Figures 5.8 and 5.9. Recall from Figure 5.6 that the mean free path for collisions approaches the scale size of the chamber near 20 mTorr. Figure 5.8 is an EEDF for a discharge at 4.5 mTorr pressure and Figure 5.9 is an EEDF for a discharge at 19 mTorr pressure. The 4.5 mTorr discharge has an EEDF which falls well below the Maxwellian distribution for high energy electrons. However, the 19 mTorr discharge very closely approximates a Maxwellian distribution. In the higher-pressure, collisional discharge, the high energy electrons are not preferentially confined by the magnetic cusp and are able to fill a Maxwellian distribution. Note also that the average electron energy increases with decreasing pressure. This behavior, noted also by Hopwood, is required to maintain the discharge as diffusion losses increase.

Figure 5.10 shows the EEDF for 0 cm, 1 cm and 2 cm downstream of the cavity base. The EEDF retains the same shape and the average electron energy decreases slightly as the probe is moved away from the cavity.

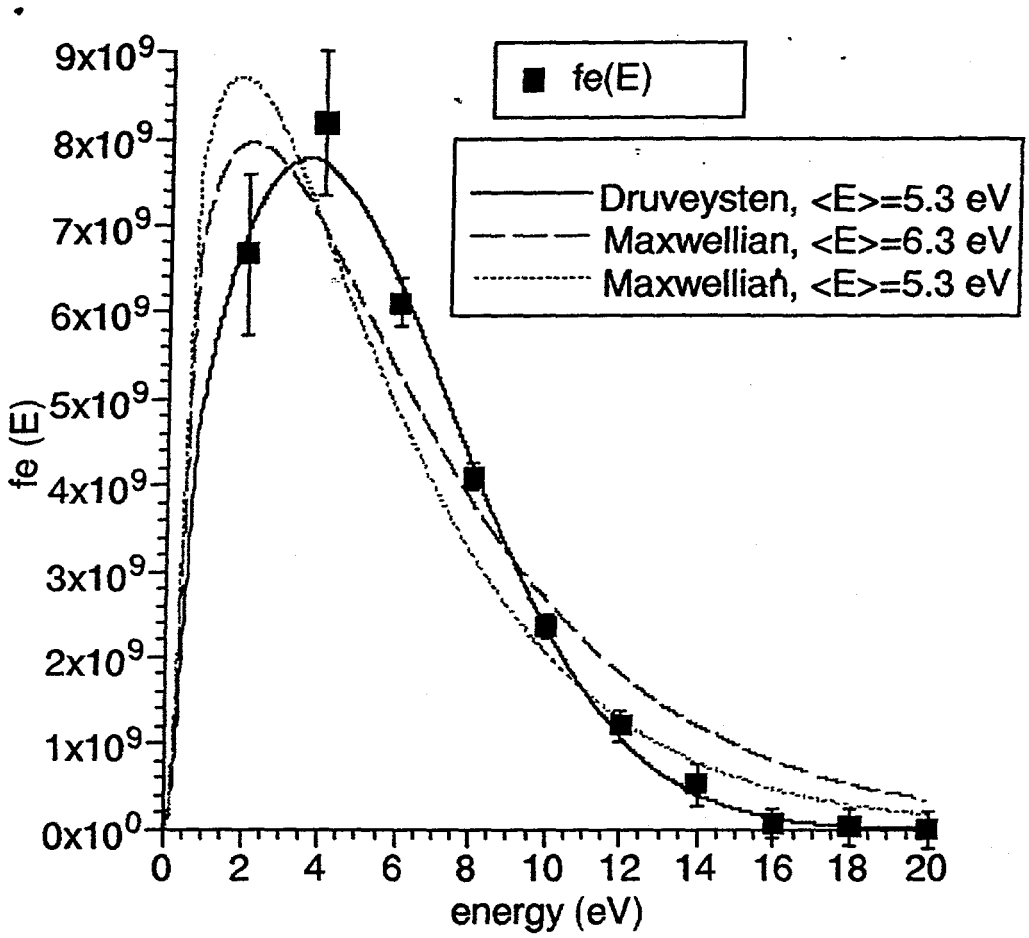

Figure 5.7. EEDF of a 14 mTorr discharge with 125 Watts input power. The probe was located at the base of the cavity (downstream distance = 0 cm).

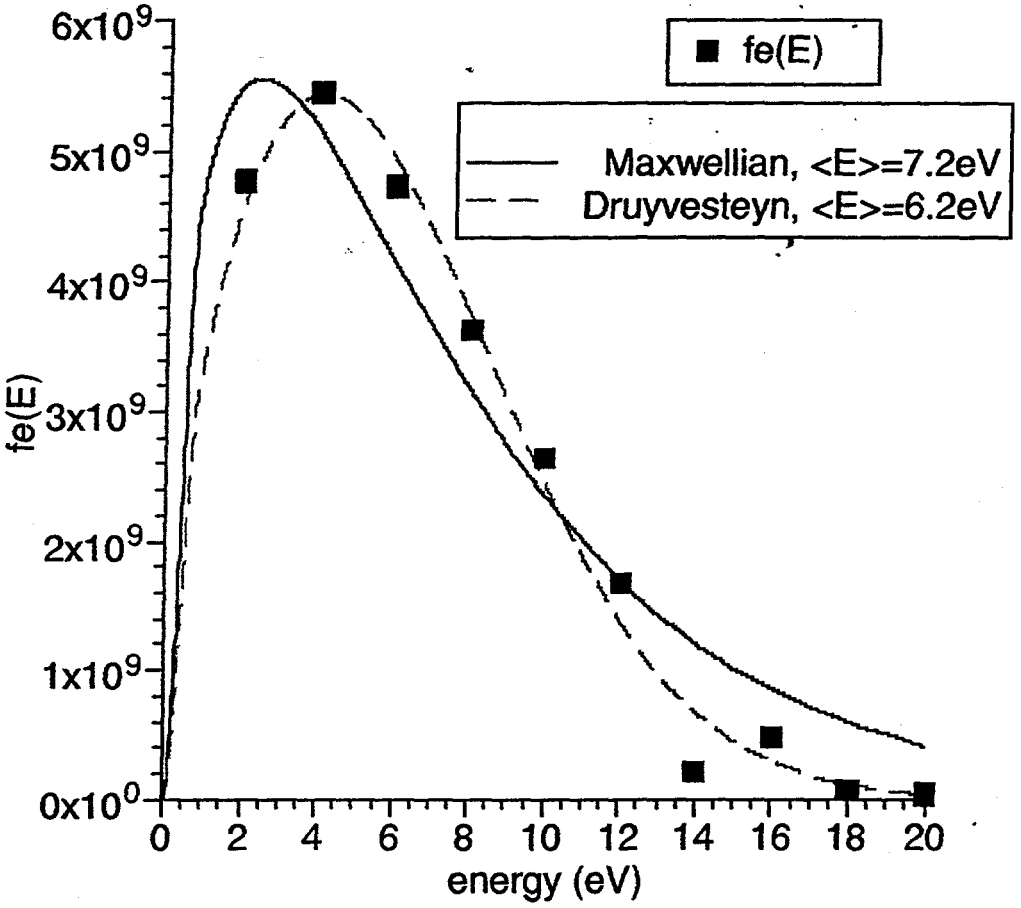

Figure 5.8. EEDF at the base of the cavity for a 4.5 mTorr, 125 Watt discharge. The solid line is a Maxwellian distribution of average energy 7.22 eV and the dashed line is a Druyvesteyn distribution of average energy 6.15 eV.

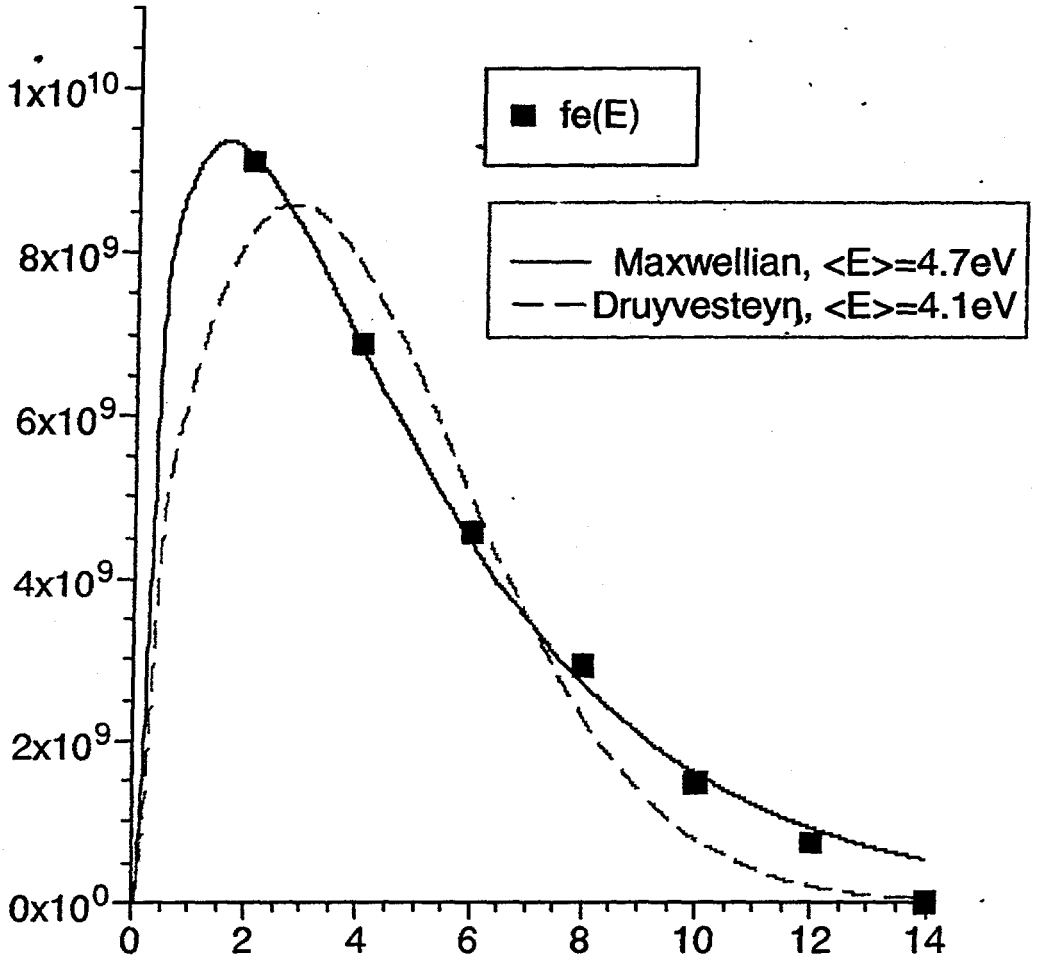

Figure 5.9. EEDF at the base of the cavity for a 19 mTorr, 125 Watt discharge. The solid line is a Maxwellian distribution of average energy 4.68 eV and the dashed line is a Druyvesteyn distribution of average energy 4.14 eV.

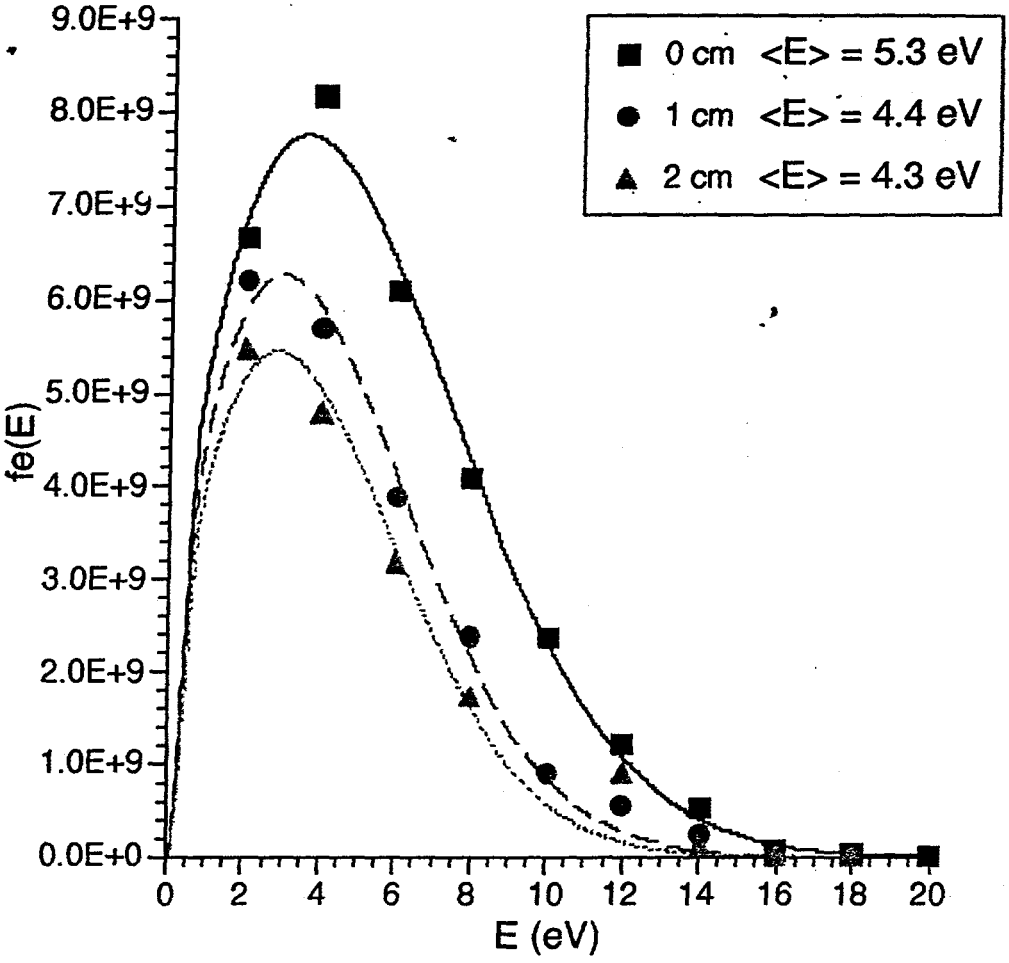

Figure 5.10. EEDF at three different downstream locations for a 14 mTorr, 125 Watt discharge. Curves are fit to a Druyvesteyn distribution.

CHAPTER 6

IMAGING OF ECR REGION

The spatial intensity distribution of the optical emission reveals information about uniformity of heating in a plasma. In this experiment, a charge-coupled device (CCD) camera is used to image the discharge in the ECR region of the microwave resonant cavity.

6.1 Experimental Setup

Figure 6.1 shows the experimental setup for the CCD imaging experiments. The CCD camera is model 1530-P/PUV manufactured by EG&G/PARC. The camera is powered and cryogenically cooled by the model 1534 Cryo Power Block. The CCD camera consists of an array of 512 x 512 photodiodes covering an area 7.9 mm square. The data were collected using a personal computer with fiber optic links to the camera, allowing both camera control and data acquisition through the computer. Data were acquired by the OMA4000 software supplied by EG&G/PARC. Images were displayed as they were taken, then stored to disk. The data was then converted to ASCII and contour plotted using DeltaGraph Pro® software[Del93]. In most of the experiments, the diodes were binned in groups of 8 x 8 resulting in a 64 x 64 array output to allow for faster data manipulation on a personal computer.

The plasma source was bolted to one port of a six-way cross and a glass viewport was directly across from it to allow viewing of the discharge region along the axis of the cavity. The CCD camera was placed in the line of sight of

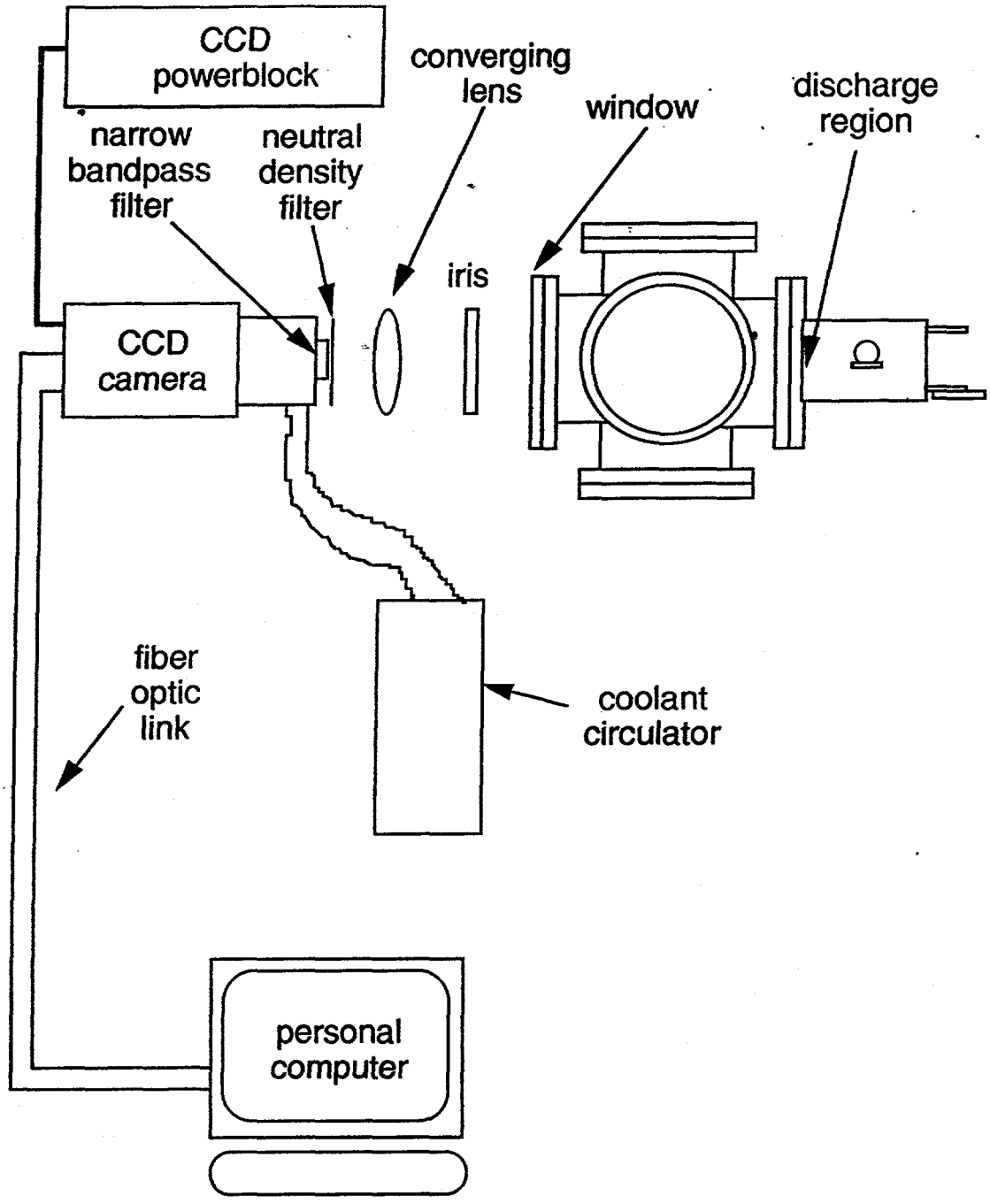

Figure 6.1. Experimental setup for CCD imaging experiments.

the discharge. Optics preceding the camera included a 5 mm focal length converging lens and an adjustable aperture. Because the detector is very light-sensitive (10 photon/count), much attenuation of the light is needed. A low-bandpass filter Model S10-671 (670.8 ± 11 nm) manufactured by Corion was used as well as neutral density filters to protect the very light-sensitive CCD array. The bandpass filter was chosen to center around the strongest Li-I line. The exposure time was set to maximize exposure and thus retain detail without saturating the detector. Exposure time varied from 10 to 100 ms, depending upon the intensity of the emission.

6.2 CCD Imaging Results

Figure 6.2 is a typical image of the ECR region taken by the CCD camera, with light intensity corresponding to increased signal in the legend below the figure. Superimposed on the image are the TE111 mode electric field lines and the multicusp magnetic field lines. Plasma emission is strongest at the top and bottom ECR zones. These correspond to the regions where the resonant cavity electric field is perpendicular the magnetic field lines allowing for the most efficient coupling of microwave energy to the electrons. Three ECR regions to the right of the antenna are clearly visible as is one ECR zone to the left of the antenna. However, the emission intensity from the left side of the discharge is about 85% of the emission intensity from the right side of the discharge. Two factors could be contributing to this asymmetry. First, and most likely, is that the microwave input antenna is not centered in the cavity. This would perturb the electric field mode causing an asymmetry in the discharge. Another possible contributor to the asymmetry is the argon gas flow which is from the right side (see Figure 2.2). If this were the case, the asymmetry should decrease with gas flow (i.e., lower

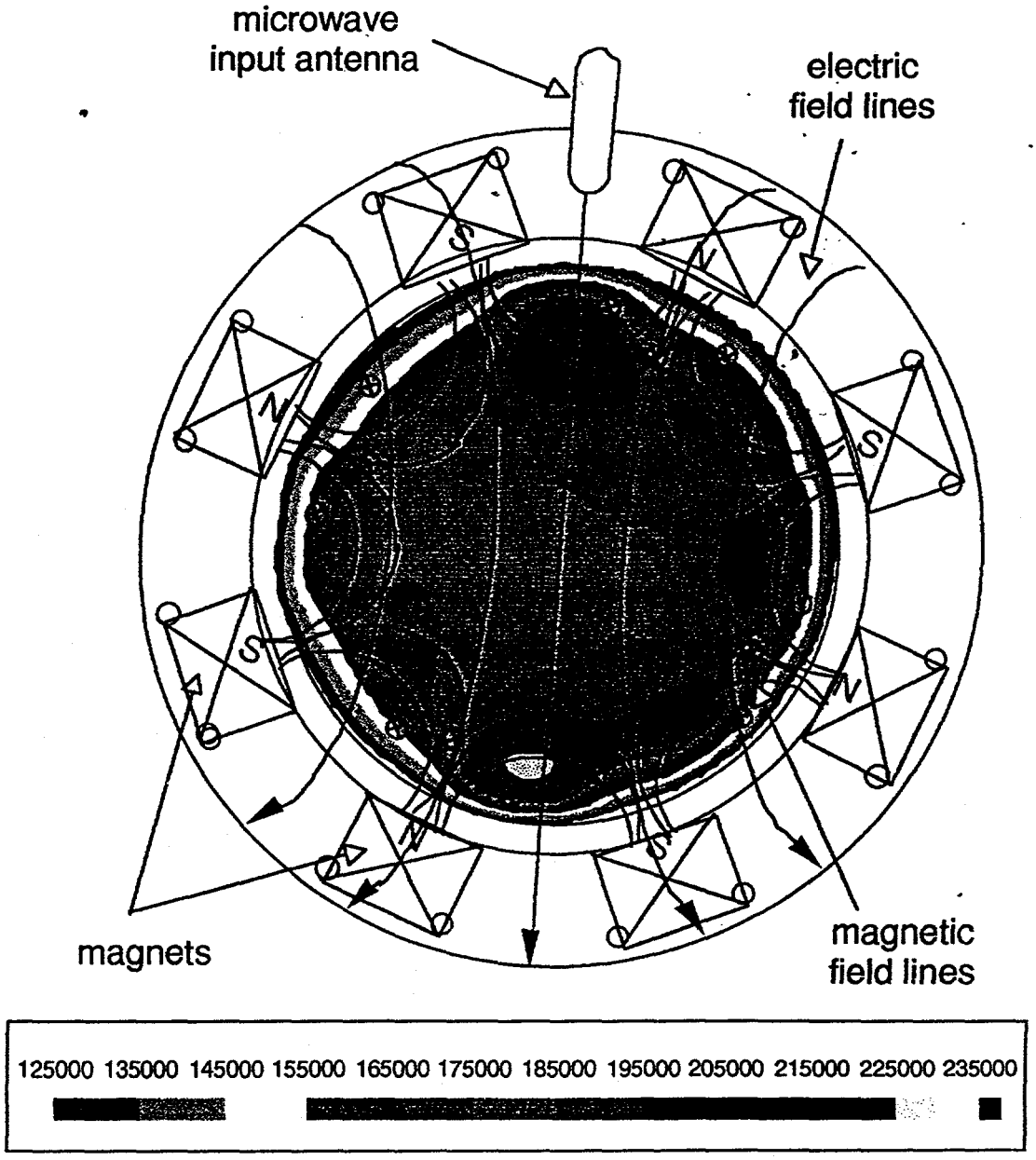

Figure 6.2. CCD camera image of ECR zone of an argon discharge at 22 mTorr and 124 Watts. The TE111 electric field lines and multicusp magnetic field lines are superimposed on the image.

pressure). As Figure 6.3 indicates, an asymmetry is visible even at 5.9 mTorr and 3.7 mTorr.

Figure 6.3 contains images of discharges at four different operating pressures: (a) 22 mTorr, (b) 16 mTorr, (c) 5.9 mTorr, and (d) 3.7 mTorr, each with an input power of 124 Watts. As illustrated by these images, the discharge becomes more uniform as the pressure decreases. This can be explained by considering the collision mean free path as discussed in Chapter 5. Recall that the mean free path is on the order of the discharge chamber for pressures near 20 mTorr and hundreds of centimeters for pressures below about 12 mTorr (see Figure 5.6). In the collisionless discharge, particles diffuse to the center of the discharge chamber much more readily resulting in a more uniform discharge.

Figure 6.4 contains spectra taken with the spectrograph described in section 4.2. These spectra were taken at the same time as the CCD images were taken but without the low bandpass filter using the same setup shown in Figure 4.1. For reference, the brackets indicate the wavelength region of the full width of half maximum of the optical filter used with the CCD camera. In Figure 6.4 (a), about half of the light corresponds to Li-I and the other half to Ar-I. This spectrum corresponds to Figures 6.2 and 6.3. The second spectrum, and the CCD image in Figure 6.5, were taken after approximately 30 mg of LiCl were added to the system. The lithium emission is strongest near the bottom of the ECR region. This is expected because the LiCl is deposited in that region of the discharge chamber. A continuous flow or spray of lithium is needed to fill the chamber more evenly.

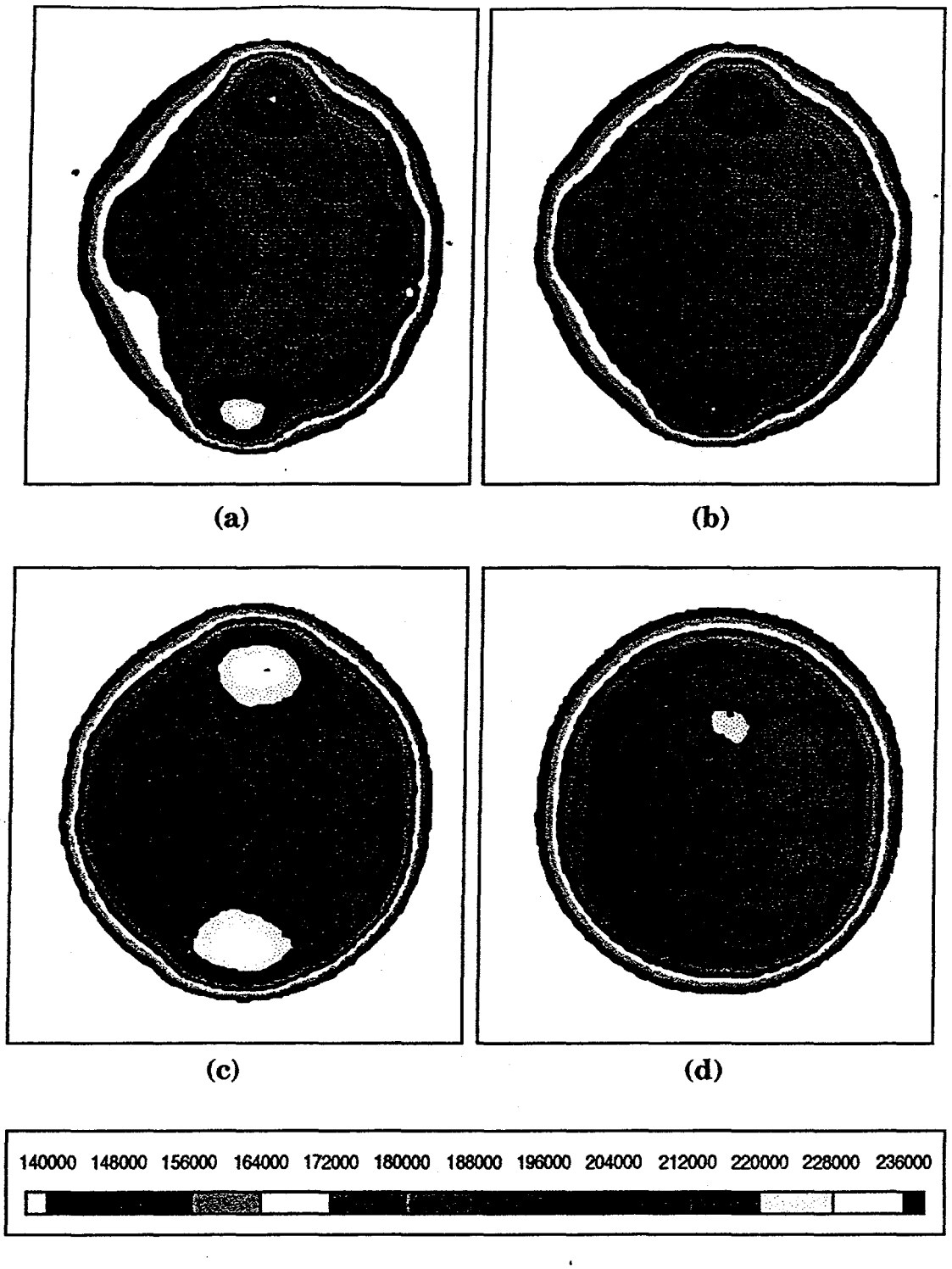

Figure 6.3. CCD camera images for argon discharges at (a) 22 mTorr, (b) 16 mTorr, (c) 5.9 mTorr, and (d) 3.7 mTorr. Input power is 124 Watts.

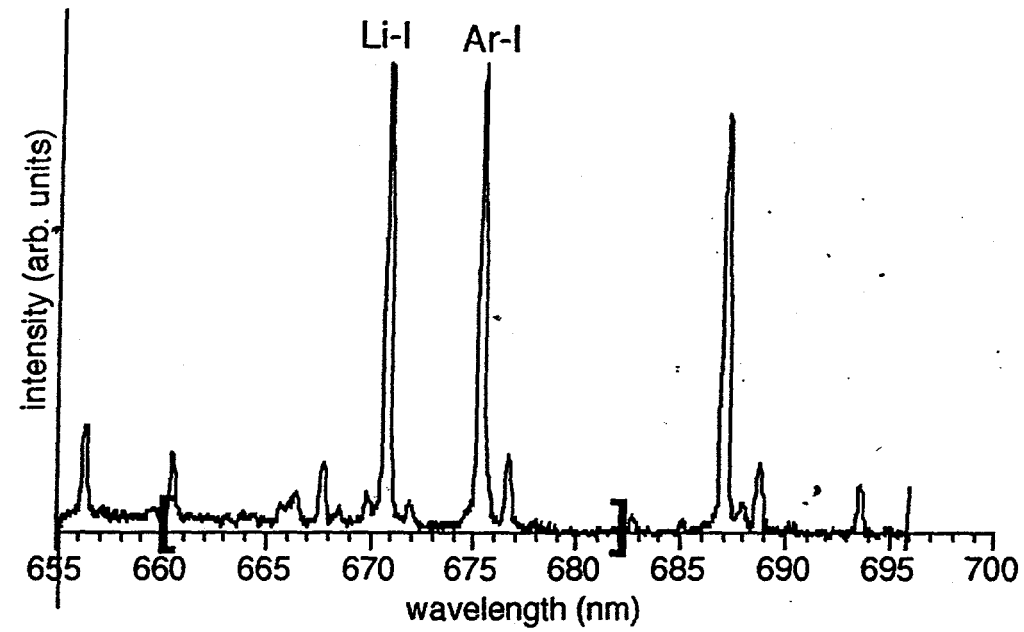

(a)

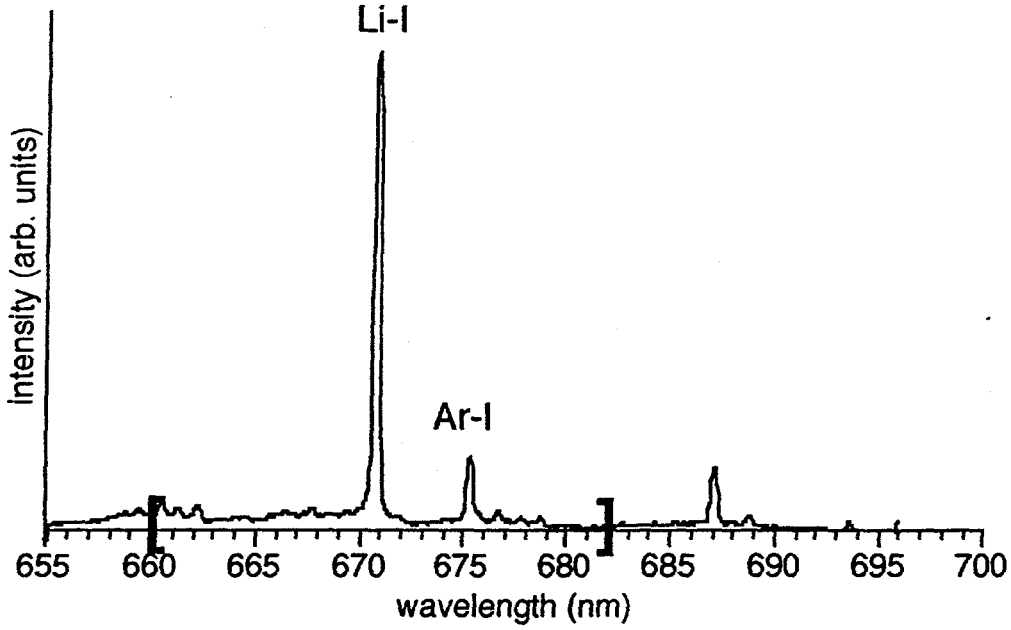

(b)

Figure 6.4. Optical emission spectra for an argon/LiCl discharges. Brackets on the axis indicate region within full width at half maximum of line filter. (a) is before and (b) is after new LiCl addition.

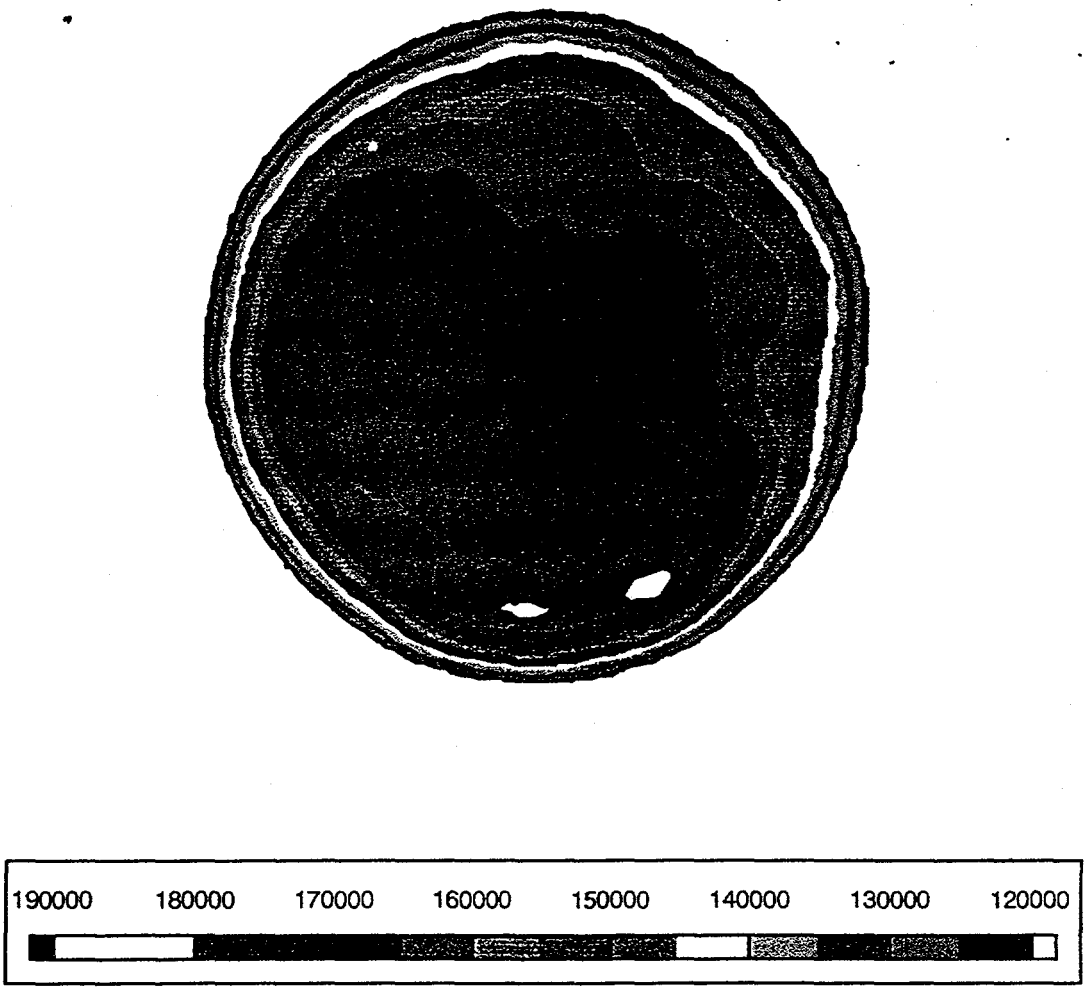

Figure 6.5. CCD camera image for a high-lithium discharge at 8.3 mTorr and 132 Watts input power.

CHAPTER 7
CONCLUSIONS AND FUTURE WORK

7.1 Conclusions

A multicusp, electron cyclotron resonant, microwave resonant cavity lithium plasma source has been constructed and tested. This source will provide a lithium plasma for laser enhanced isotope separation studies. Four plasma diagnostic techniques have been implemented to measure the operating characteristics of this lithium plasma source. These diagnostic techniques include: double Langmuir probe measurements of ion density and electron temperature; optical emission spectroscopy of lithium-argon discharges; single Langmuir probe measurements of the electron energy distribution function, electron temperature and electron density; and two dimensional charge-coupled device camera imaging of the electron cyclotron region.

Initial operation and characterization of the source was performed with argon-only discharges. Ion densities were measured to be 4-16 x 10^{10} cm^{-3} for argon discharges at typical operating pressures of 4-20 mTorr and input powers of 100-250 Watts at a location of 3 cm downstream of the cavity. The electron Debye length was measured to be 0.004-0.007 cm for those same operating conditions.

Lithium was introduced to the system by placing lithium containing compounds directly into the discharge region of the cavity. Lithium chloride

and lithium carbonate were both tested as sources of lithium. About 10 mg of LiCl was initially tried in the system, and no change in the resonant cavity behavior was seen. This amount of LiCl was "used up" very quickly (in about 15 minutes of discharge time) so the LiCl was then increased to extend the lithium discharge time. It was found, however, that as the LiCl was increased a higher background argon pressure was needed to ignite the discharge. The pressure could then be decreased and the discharge maintained. Li_2CO_3 was also introduced in the same manner and was found to have less of an impact on plasma start-up. The latter lithium compound was used up much more slowly but deposited much less lithium into the discharge. It was also observed that very little lithium was detected downstream of the cavity when Li_2CO_3 was used while LiCl produced a large Li-I optical signal as far as 5 cm downstream. After several months of continuous LiCl use, the discharge chamber became "conditioned" and a more constant amount of lithium could be maintained in the discharge.

Electron energy distribution measurements indicate that the electrons have a Druyvesteyn distribution function at pressures below 16 mTorr. At 20 mTorr, the discharge becomes collisional and the EEDF is Maxwellian. The average electron energy decreased with increasing discharge pressure. At 4.5 mTorr an average electron energy of 6 eV is measured. This number decreases to about 4.7 eV for a 19 mTorr discharge. The electron and ion densities fall off exponentially with distance downstream from the cavity base. Peak electron densities of 1.5×10^{11} cm^{-3} were measured near the cavity base, and these densities dropped to 1×10^{10} cm^{-3} at 10 cm downstream of the cavity.

A two-dimensional imaging system utilizing a charge-coupled device camera was successfully designed and used to image the electron cyclotron

resonant region of the discharge. A left-right asymmetry in the plasma emission was noted, particularly at higher operating pressures of 16-22 mTorr. This asymmetry is most likely caused by misplacement of the microwave input antenna. Plasma uniformity in the center of the discharge was observed to increase with decreasing discharge pressure. At 16-22 mTorr, clearly distinguishable ECR regions were observed. At an operating pressure of 3.7 mTorr, the emission was very uniform in the center of the discharge region.

7.2 Suggestions for future research

Some modifications and improvements of this source would make it more useful for lithium plasma production. A method to control the flow of lithium into the discharge region would improve reproducibility and perhaps eliminate the need for a buffer gas. Such a system would need to be designed carefully to avoid problems mentioned earlier such as condensation of solids on the input line. The use of elemental lithium should be considered to avoid the damage to the vacuum system components and the quartz discharge chamber cause by the presence of free chlorine. However, lithium must be handled carefully because it oxidizes very rapidly in air and is also quite flammable and toxic.

Continued study of the electron energy distribution function is warranted. Recall that the ionization of the species to be enriched is provided by electron impact of the excited atom. Modeling of the EEDF's effect on isotope separation efficiency should be performed. Such a model may be used to determine the best operating parameters (power, discharge pressure) for isotope separation studies. A detailed model of the downstream chemical

kinetics is needed as well to fully understand the plasma behavior away from the cavity.

It is the hope of the author that this lithium plasma source will be successfully used as a means for laser isotope enrichment. The source has been designed with that end in sight. It has been shown for the first time that microwave discharges can successfully dissociate lithium compounds and integrate free lithium into a background argon discharge. Care has been taken to provide laser access to the discharge created by the source.

APPENDICES

APPENDIX A

VACUUM RESONANT CAVITY FIELD MODES

The vacuum resonant cavity field modes are derived in this appendix. Introduction of such perturbations as the quartz cup and the discharge will, of course, change the resonant field modes. The vacuum modes, however, provide a good reference or "starting point" for igniting the discharge and understanding the cavity behavior.

The derivation begins with the sourceless Maxwell's equations with periodic time dependence:

$$\nabla \times \mathbf{E} = -\frac{1}{c}\frac{\partial \mathbf{B}}{\partial t} = j\,\omega\,\mathbf{B} \tag{A.1}$$

$$\nabla \times \mathbf{B} = \mu\varepsilon\frac{\partial \mathbf{E}}{\partial t} = -j\mu\varepsilon\,\omega\,\mathbf{E} \tag{A.2}$$

$$\nabla \cdot \mathbf{E} = 0 \tag{A.3}$$

$$\nabla \cdot \mathbf{B} = 0 \tag{A.4}$$

By combining the two curl equations and with $\mu\varepsilon = \frac{1}{c^2}$, these lead to

$$\nabla^2 \begin{Bmatrix}\mathbf{B}\\ \mathbf{E}\end{Bmatrix} - \frac{\omega^2}{c^2}\begin{Bmatrix}\mathbf{B}\\ \mathbf{E}\end{Bmatrix} = 0. \tag{A.5}$$

Assuming propagation in the z-direction and dependence such as

$$\begin{Bmatrix}\mathbf{E}(x,y,z,t)\\ \mathbf{B}(x,y,z,t)\end{Bmatrix} = \begin{Bmatrix}\mathbf{E}(x,y)\\ \mathbf{B}(x,y)\end{Bmatrix} e^{\pm jkz - j\omega t}. \tag{A.6}$$

The wave equation becomes

$$\left[\nabla_t^2 + \left(\frac{\omega^2}{c^2} - k^2\right)\right]\begin{Bmatrix}\mathbf{E}\\ \mathbf{B}\end{Bmatrix} = 0 \tag{A.7}$$

where ∇_t^2 is the transverse part of the Laplacian, $\nabla^2 - \frac{\partial^2}{\partial z^2}$.

In a cylindrical resonant cavity, reflection at the end faces requires a standing wave solution in the z-direction. The standing wave has the form

$$A \sin kz + B \cos kz. \tag{A.8}$$

To satisfy boundary conditions, k must be given by

$$k = \frac{p\pi}{h} \tag{A.9}$$

where p is an integer and h is the cavity height. For *transverse magnetic* fields, $\mathbf{E}_t = 0$ at 0,h. So

$$E_{z,TM} = \Psi(x,y) \cos\left(\frac{p\pi z}{h}\right), p = 0,1,2,... \tag{A.10}$$

For *transverse electric* fields, $\mathbf{B}_z = 0$ at z = 0,h. This gives

$$B_{z,TE} = \Psi(x,y) \sin\left(\frac{p\pi z}{h}\right), p = 1,2,... \tag{A.11}$$

In cylindrical geometry

$$\nabla_t^2 = \frac{1}{r}\frac{\partial}{\partial r}\left(r\frac{\partial}{\partial r}\right) + \frac{1}{r^2}\frac{\partial^2}{\partial \phi^2}$$

so the transverse wave equation becomes

$$\frac{1}{r}\frac{\partial}{\partial r}\left(r\frac{\partial \Psi}{\partial r}\right) + \frac{1}{r^2}\frac{\partial^2 \Psi}{\partial \phi^2} + \left(\frac{\omega^2}{c^2} - k^2\right)\Psi = 0 \tag{A.12}$$

The solutions to this equation can be found by separation of variables: $\Psi(r,\phi) = R(r)\Phi(\phi)$. Thus

$$\Psi(r,\phi) = J_m(\gamma_{mn} r)\, e^{\pm jm\phi}, \text{ where } \gamma^2 = \frac{\omega^2}{c^2} - k^2. \tag{A.13}$$

The *transverse electric* boundary conditions are $\hat{n} \cdot \nabla B_z |_{surface} = 0$. Thus

$$\frac{\partial \Psi}{\partial r}\Big|_a = 0 = J_m'(\gamma_{mn} a) \Rightarrow \gamma_{mn} a = x_{mn}', \tag{A.14}$$

where a is the cavity radius and x_{mn}' is the n^{th} zero of the derivative of the m^{th} order Bessel function. Putting this contraint along with the constraint on k into the definition of γ one obtains

$$\left(\frac{x_{mn}'}{a}\right)^2 = \frac{\omega^2}{c^2} - \left(\frac{p\pi}{h}\right)^2$$

thus

$$\omega_{mnp}^2 = c^2\left[\left(\frac{x_{mn}'}{a}\right)^2 + \left(\frac{p\pi}{h}\right)^2\right] \qquad (A.15)$$

For $f_r = \frac{\omega}{2\pi c}$, the resonant frequency is given by:

$$(f_r)_{mnp}^{TE} = \frac{1}{2\pi\sqrt{\varepsilon\mu}}\sqrt{\left(\frac{x_{mn}'}{a}\right)^2 + \left(\frac{p\pi}{h}\right)^2} \qquad (A.16)$$

A similar derivtion gives the *transverse magnetic* resonant frequencies. The boundary condition is $E_z\,(r=a) = 0$. We get $\gamma_{mn}\,a = x_{mn}$, where x_{mn} is the n^{th} zero of the m^{th} Bessel function. Then

$$\omega_{mnp}^2 = c^2\left[\left(\frac{x_{mn}}{a}\right)^2 + \left(\frac{p\pi}{h}\right)^2\right] \qquad (A.17)$$

and

$$(f_r)_{mnp}^{TM} = \frac{1}{2\pi\sqrt{\varepsilon\mu}}\sqrt{\left(\frac{x_{mn}}{a}\right)^2 + \left(\frac{p\pi}{h}\right)^2}. \qquad (A.18)$$

For the compact resonant cavity, the cavity radius was chosen to be fixed at a = 4.45 cm and the microwave frequency is fixed at 2.45 GHz. Equations A.16 and A.18 can be solved for the cavity height. Thus one obtains for the transverse electric mode

$$h_{TE} = p\pi\left[(2\pi f)^2\,\varepsilon_0\mu_0 - \left(\frac{x_{mn}'}{a}\right)^2\right]^{-1/2} \qquad (A.19)$$

and for the transverse magnetic mode

$$h_{TM} = p\pi\left[(2\pi f)^2\,\varepsilon_0\mu_0 - \left(\frac{x_{mn}}{a}\right)^2\right]^{-1/2}. \qquad (A.20)$$

Table A.1 contains the first few zeros of the Bessel functions. The lowest order mode supported is the TE_{011} mode corresponding to a cavity height of 6.1 cm. The first non-zero value corresponds to $x_{11}' = 1.841$ and this results in a cavity height of h=10.4 cm. No other modes can be supported by this cavity at 2.45 GHz if the radius is to remain fixed at 4.45 cm. Figure A.1 shows the probable electromagnetic mode relative to the cavity walls.

Table A.1. Zeros of the Bessel functions.

$J_n(x_{nm}) = 0$	$J_n'(x_{nm}') = 0$
$x_{01} = 2.4048$	$x_{01}' = 0.0000$
$x_{11} = 3.8317$	$x_{11}' = 1.8412$
$x_{21} = 5.1356$	$x_{12}' = 3.0542$
$x_{02} = 5.5201$	$x_{02}' = 3.8317$

Introducing a plasma into the cavity changes the effective dielectric constant. In a plasma,

$$\varepsilon(\omega) = \varepsilon_o\left(1 - \frac{\omega_p^2}{\omega^2}\right).$$

Thus ε is effectively reduced inside the discharge. The cavity height h goes as $\frac{1}{\sqrt{\varepsilon}}$, so for a constant cavity width and resonant frequency, the cavity height must be increased with the plasma present.

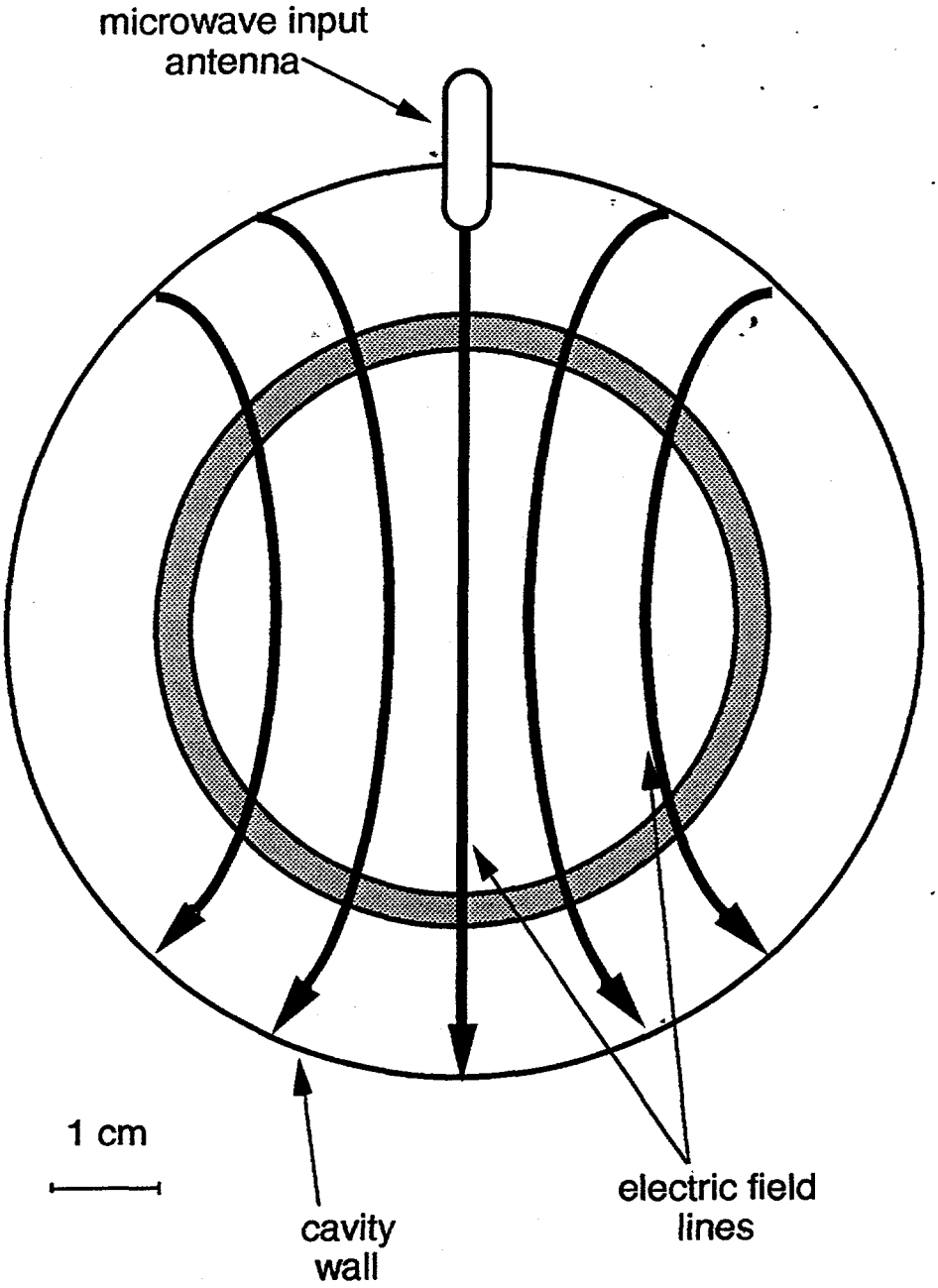

Figure A.1. TE111 electric field mode observed in resonant cavity.

APPENDIX B

MODIFICATIONS AND MAINTENANCE OF COPPER VAPOR LASER

Modifications and maintenance were performed on the Oxford copper vapor laser on June 27 and June 28, 1994 to prepare it for use as a pump laser for the Lambda Physik dye laser in the lithium isotope separation experiment.* To be used as a pump laser, low divergence optics and a polarizing filter were required in the copper vapor laser. Additionally, to improve power output, excess copper buildup around the edges of the laser cavity had to be removed and a fresh copper charge needed to be added to the tube. Before maintenance and modifications, the output power of the laser was 6 Watts.

To prepare for cleaning the excess copper out of the laser tube, the tube was removed from the case by disconnecting electrical and gas connections and removing the bolts on the grounded end of the tube connecting it to the case. The glass laser tube and connected flanges (which contain the electrodes) were lifted out of the case and placed on the laboratory bench. The end window on the grounded end of the tube was first removed by removing the four bolts on the retaining ring. The end flange was then removed by loosening the recessed bolts on the end of the flange. The electrode was inspected and found to be in good repair. The end window was cleaned using a lint-free tissue and the cleaning fluid found in the laser maintenance kit

---

*After modifications, the copper vapor laser was found to have insufficient power to act as a pump source for the dye laser. This appendix has been included as a reference for those who might use the copper vapor laser in the future for other applications.

provided with the laser. Only the non-coated, inside of the window may be cleaned. The window was held in the retaining ring and few drops of cleaning fluid dropped onto the window. The window was then scrubbed gently using circular motions with a lint-free tissue. The window was removed from the retaining ring holding only the edges and rinsed thoroughly with methanol. The window was then returned to the retaining ring, taking care that the coated side was facing outward. The viton o-ring providing the vacuum seal at the window was replaced with the spare found in the maintenance kit. The size of this o-ring is 40.87 mm i.d. x 3.53 mm and the o-ring was first coated with a thin layer of vacuum grease before use. The o-ring on the flange was also replaced with the spare from the kit; its size is 113.67 mm i.d. x 6.99 mm. The uneven copper buildup around the inner edge of the laser tube was loosened using a round bottle brush of 1 1/2" diameter. The excess copper was then removed using the shop vacuum. This procedure was repeated until all of the copper buildup had been removed. The end flange was then replaced, taking care to tighten the recessed bolts evenly around the tube until resistance is just felt. To complete the maintenance on the grounded end of the tube, the window and retaining ring were replaced again tightening the bolts evenly and until resistance is just felt.

The same maintenance was performed on the high-voltage end of the laser tube. First the retaining ring and window were removed and cleaned using the above procedure. To remove the end flange, two bolts were removed from each of the plates connecting the two end flanges. The gas in and gas out lines and the pressure gauges were disconnected as well. The high voltage end flange was then be unbolted and pulled away from the laser tube. The high voltage electrode was found to have sustained some minor damage but was determined to be still usable by the Oxford Lasers service engineer. The

damage consisted of a hole in the lower portion of the electrode semicircular in shape with a diameter of approximately 1 cm. Again, the excess copper was loosened and removed from the laser tube and the high voltage electrode, flange, and gas lines reassembled, again replacing the o-ring. The tube was returned to the laser case and bolted to the case with the rear optical assembly still removed.

After returning the tube to the case, new copper was loaded into the laser cavity through the open rear end of the tube. Ten (average) 1.1 gram pieces of copper were cut from a used eight inch high vacuum copper gasket. The copper in high vacuum gaskets is of very high quality, more so than typical electrical wire. The ten pieces of copper were placed evenly on the recharging holder and pushed into the tube to the line marked on the holder. The line which was used is marked "CB'94" and is farther back than the line originally on the holder to allow more even distribution within the tube. The holder was rotated 180° and withdrawn from the tube, taking care to hold it against the upper edge so as not to disturb the copper pieces. The rear mirror was then reattached again replacing the o-ring seal.

The laser was then reconditioned by allowing the tube to be pumped out for about 45 minutes. To do this, the GAS OUT switch was opened (down position) and the GAS IN valve was closed. A pressure gauge located in the gas out line was used to monitor the pressure and check for leaks. The laser was then aligned with the planer mirrors still in place and the output power checked. To align the laser, it was run until the green laser light was produced. The rear mirror was then aligned by maximizing the output power by adjusting the two screws on the rear mirror optical mount. The rear mirror may also be aligned by using a neutral density filter to protect the eyes and viewing it through the front mirror and tube with the laser turned off after it

has been allowed to run for 45 minutes. To align the mirror, use the rear screws to center the mirror in the tube. Then the laser was turned back on and allowed to run until laser light is produced. The front mirror was then adjusted until well focused and the power maximized. To facilitate cleaning of the laser with the new copper charge, the fast gas in/out were turned on for 10 second intervals and allowing the pressure to stabilize between the intervals. The maximum power after alignment and running for approximately 60 minutes was 8.0 Watts.

Next, the unstable optics set was installed into the laser. With the laser again turned off, the planer front and rear mirrors were removed, wrapped in lint-free tissues, and stored for future use. The rear beam dump was removed from the laser case to facilitate alignment of the new front mirror. The front mirror, which is a 4 mm diameter convex mirror mounted onto a plate, was installed using the planer mirror mounting screws. The front mirror is at a 45° angle with respect to the vertical and is mounted such that the outer edge of the mirror can just be seen when viewed down the rear of the tube. The laser head cover was then replaced and the laser turned on and allowed to heat up until laser light was seen. The front mirror was then adjusted by dumping the beam on the front wall of the laboratory, approximately 2 meters from the laser. The laser head cover must be opened to adjust the mirror. Normally, this would require that the laser be warmed up again for approximately 30 minutes between adjustments. To avoid such long delays, the head panels override was switched and the case opened. Adjustments were then made quickly, taking less than one minute for each adjustment; the cover was closed and the override switch turned off. This allowed for quicker adjustment, but care must be taken to make adjustments as speedily as possible. Laser light could then be seen again within a few

minutes after adjustment. This procedure was then repeated until the beam emerging from the open end of the laser was fully circular. The laser was then turned off and the 50 mm diameter concave rear mirror mounted in place in front of the rear beam dump. After the laser was turned on and allowed to warm up again, the rear mirror was aligned by viewing the beam through goggles and focusing the beam on the front beam dump. The beam retains a missing small semicircle due to the front mirror in the unstable optics setup. Final adjustments were made by maximizing the output power with the power meter. The final output power was measured to be 7.1 Watts.

APPENDIX C

INSTALLATION AND ALIGNMENT OF DYE LASER

In this appendix are notes on the installation and alignment of the Lambda-Physic Scanmate dye laser which will provide the light for laser enhanced isotope enrichment studies. This is a transcript of notes taken by the author during installation of the laser and provides some information not included in the laser manual.

C.1 Mixing Dye and using Dye Circulator

(1) Measure dye weight and put dye into container, then pour solvent over dye. Dyes which do not dissolve easily may be assisted by using an ultrasonic mixer. *Be sure to use a new filter with a new dye/solvent mixture.* When attaching dye container to circulator, it is helpful to turn circulator pump on as the container is lifted into place.

(2) **Changing dyes:** The circulator needs to be rinsed thoroughly rinsed with solvent only prior to introducing a new dye.

(a) Carefully unscrew dye container and lower slightly. With right hand, press reverse flow button. Continue lowering dye container with left hand until it is completely free of the circulator. When most of dye has been returned to container, unplug circulator with right hand while still holding the reverse button down. It is helpful to have the circulator plug resting on the receptacle as lightly as possible.

(b) Pour the used dye into an amber container (to protect from light) if it will be used again, or dispose properly if it will not. Dyes can be saved for later use and will be better preserved under refrigeration. Remove filter from circulator and store in a zip-lock bag with dye.

(c) Rinse the circulator with solvent only by circulating solvent both forward and reverse using about 2/3 liter. This must be repeated with clean solvent at

least three time, or more until solvent is clear. Again to clear circulator of solvent, use the reverse button and lower the container away from the circulator.

(3) If the efficiency of the dye laser drops and all other reasons are eliminated, a fresh dye may be needed: A typical dye lifetime is 1-2 years.

(4) The dye used in the original installation of this laser was DCM. The concentration was 0.71g DCM in 1 liter DMSO (dimethyl sulfoxide). At the dye peak of 658 nm, the maximum output energy was 7.2 mJ with 100 mJ of input from the XeCl excimer at 308 nm. The output energy at 671 nm, the wavelength to be used in the first experiments, was 6.3 mJ.

C.2 Alignment of Dye Laser

(1) *The maximum input power from the excimer laser into the dye laser is 100 mJ.* The optics in the dye laser cannot withstand more than 100 mJ for an extended time.

(2) When the cover is open on the dye laser, the input shutter is opened by pulling up on the red knob above the shutter.

(3) Begin dye laser program by typing "scanmate" at the DOS prompt of the controller (notebook computer). Inside the laser case is a switch which turns on the microelectronics which control the grating. Each time that switch is turned on the grating is driven to its calibrated (zero) position, written near the grating inside the laser (1058.612 nm). The endstop must be calibrated on the computer. The program will save this setting, but if the software is reinstalled this setting must be checked and possibly changed. To do so go through the following menu:
   (a) set grating
   (b) cal endstop: enter calibration number (1058.612)

(4) Set grating to peak of dye while making alignment adjustments. To set grating position:
   (a) grating
   (b) set (type in endstop wavelength: 1058.612)

(c) execute
All actions done by the controller must be followed by the command execute for them to be done.

(5) Note micrometer setting (3.12) written near micrometer on laser. Begin alignment by setting micrometer to this factory setting. The nearby thumbscrew may then be used to move beam such that it is aligned with aperture in beam alignment tool.

(6) Determine that mirrors are at the proper position for the wavelength region being used. There are three possible regions: red, visible, and violet.

(7) Inside the laser, all vertical adjustments have green knobs, whereas horizontal adjustments have yellow knobs.

(8) **Checking alignment**
- (a) Block preamp beam with beam block. This is a long steel rectangle with a black lip which rests on the optical rail at the preamp beam entrance.
- (b) The line on the grating should be homogenous. If not adjust OSCILLATOR vertical position. This can be best checked at the edge of the dye emission by carefully lifting the grating.
- (c) Rotate cuvette and look for "shadow" on grating. Align on top of oscillator beam by rotating cuvette.
- (d) Check that small pin below cover with three apertures is slightly off center and recheck rotation.
- (e) Maximize beam intensity by moving small pin below apertures. Check to see that beam is homogenous.
- (f) Readjust micrometer to maximize intensity. It should not be necessary to move micrometer far from factory determined position.

(9) **Adjust depth of focus**
- (a) Loosen screw on vertical oscillator adjustment bracket. Pull bracket all the way forward. Push back slowly to maximize beam intensity. This adjustment should not go all the way back; to do so could cause damage to the cuvette.
- (b) Use a small corner of paper to ensure that the amplified stimulated emission (ASE--full range of color of the dye, not the lasing color) extends

approximately 1 mm below the laser beam. If not, adjust screw in hole on oscillator. *This will probably need to be adjusted only if a major change is made in the laser setup such as moving from side by side setup to end to end setup.*

(c) Readjust thumbscrew for alignment with aperture on beam alignment tool.

(10) **Adjust preamp beam**

(a) Remove preamp beam block.

(b) Adjust PREAMP vertical position to superimpose on oscillator beam.

(c) Adjust depth of focus on preamp beam to maximize intensity. Beware of a color shift, and adjust accordingly.

(11) **Telescoping lenses**

Two telescoping lenses can be used to obtain a larger output beam.

(a) The f=-50 lens goes in the first lens holder. Place the beam alignment tool between the two lens holders and adjust the vertical and horizontal knobs on lens holder to center beam.

(b) The f=150 lens goes in the second lens holder. Place the beam alignment tool at the end of the beam and adjust the vertical and horizontal knobs on lens holder to center beam.

(c) If any shift in wavelength occurs when telescoping lenses are used, check two mirror positions.

C.3 Using Etalon

(1) Check wavelength range on etalon. This is a dial which must be aligned with a white ball.

(2) Insert etalon by sliding it onto two pins just above the grating. Be sure not to touch the surfaces of the grating.

(3) **Initialize etalon**

(a) In the controller program, type etalon then init. The two keys → and ← are used to move the etalon motor.

(b) Go above normal position using arrow key (above ≈2500). Look for fringes on the grating. Adjust horizontal (yellow) know of etalon until fringes are straight, not curved.

(c) Pull etalon out of beam. Note position of dot of light on circular piece below words "oscillator cavity endmirror." This dot will not be seen with etalon in place, so make careful mental note of the position.

(d) Push etalon back into place. Move arrow keys to put leftmost line coincident to where dot was with etalon out.

(e) Note this position, designated as normal position. (2077 in initial adjustments. Should be within ±5 of this.)

(f) Normalize at central wavelength where etalon will be used.

(g) Sync position of etalon. Another etalon will be needed to do this part. Using another etalon, either in the beam path or with a view-through etalon, note fringes. Beginning with position 0, press right arrow key until double fringes are seen. Note position (+60 in initial setup). Return to 0 and press left arrow key until double fringes are then seen (-85 in initial setup). Set position to arithmetic mean (-7). Quit.

(h) Adjust diode detectors vertically until sensors A and B are equal. A thumbscrew located above the diode detectors makes the adjustment. Note that 255 is the saturation level of the diodes. A neutral density filter in front to the diodes can be rotated until the diode read about 180-200.

(i) Quit initialization.

(4) Press scan to setup scan with etalon. Index refers to the index of refraction of the environment of the laser, usually 1 for air. The grating chamber can be filled with a different atmosphere for certain applications. The minimum scan step is 0.001 nm. Counts refers to the number of pulses at each scan position.

(5) The excimer laser can be triggered from the dye laser controller. Connect the SYNC OUT on the LAN to the EXT TRIG on the minicontroller of the excimer. Be sure the trigger is in external mode on the excimer laser.

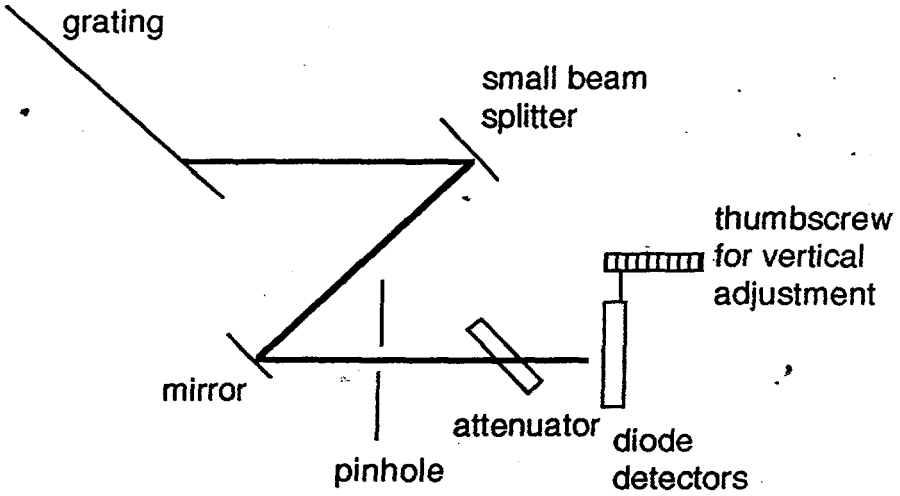

Figure C.1. Alignment of laser beam on diode detectors.

C.4 Moving and Realigning Dye Laser

Any time the dye laser is moved, the grating must be locked. The transportation lock is in place in the **up** position. It is located behind the grating cover. Before moving the dye laser, be sure it is well aligned and power is maximized in the present position. Note the output power. Move the dye laser and pump laser to their new positions, and simply move the entire box containing the laser until output is once again maximized. Then begin making fine adjustments within the laser itself as described above in "Alignment of Dye Laser."

APPENDIX D

EXCIMER LASER INSTALLATION

D.1 Installation of Excimer Laser

The following procedure was followed when installing the excimer laser and should be used when moving the laser from one location to another:

(1) Evacuate all of the gas lines and backfill the halogen line with an inert gas. *Note: The halogen line should be backfilled with inert gas any time the line is opened, whether to move the system or when simply changing the bottle.*
   (a) Insure that the halogen gas bottle is closed and the inert gas bottle (usually He) is opened.
   (b) Turn on laser mini controller, press F1 to bypass thyrotron warm-up, and press [VALVE CONTROL].
   (c) Fill block and halogen line by pressing [INERT] then [HALOGEN] about four times until the pressure on the block is about 30-35 psi. This pressure is displayed on the mini controller.
   (d) Check for leaks in the halogen line using soapy water *(Snoop)*.
   (e) Evacuate the halogen line by pressing [PUMP], [VACUUM], [HALOGEN].
   (f) Repeat steps (c) and (e) three times.

(2) Ensure that all valves in the laser are closed. Carefully open halogen bottle and set regulator to 45 psi. Fill line with halogen by pressing [PUMP], [VACUUM], then toggle [HALOGEN]. Press [PUMP] again to turn pump off.

(3) Evacuate rare gas (xenon) and buffer gas (neon) lines by pressing [PUMP], [VACUUM] and [RARE] for xenon and [BUFFER] for neon.

(4) Press [ENTER] to leave valve control mode. Usually a NEW FILL will follow this procedure.

D.2 Cleaning and Changing End Mirrors

The end mirrors should be cleaned every few months, or about every three gas fills. The following procedure should be used whenever cleaning or replacing the mirrors.

(1) Flush and fill cavity with inert gas:
   (a) In [VALVE CONTROL] mode, pump out the laser head to 30 mbar. *Do not go below about 30 mbar at any time when evacuating the laser head.* To do this, press [PUMP], [VACUUM], [LASER HEAD].
   (b) Fill laser head to 500 mbar with inert gas (helium) by pressing [INERT] and [LASER HEAD]. The inert gas valve stays open only 10 seconds, so it may have to be toggled more than once.
   (c) Pump out laser head again to 30 mbar.
   (d) Repeat steps (2) and (3) three times.
   (e) Fill laser head to 1000 mbar with inert gas before opening.

(2) Have the optics rubber stopper ready for removal of premount. Remove all six of the 3 mm screws which hold the premount against the cavity. Pull end mirror and holder off and put rubber stopper in premount opening to maintain helium environment in laser head.

(3) Carefully disassemble end mirror premount and clean *noncoated* side of mirror. Reassemble and replace onto laser head cavity. The o-ring may be wiped, but *never use vacuum grease in an excimer laser!*

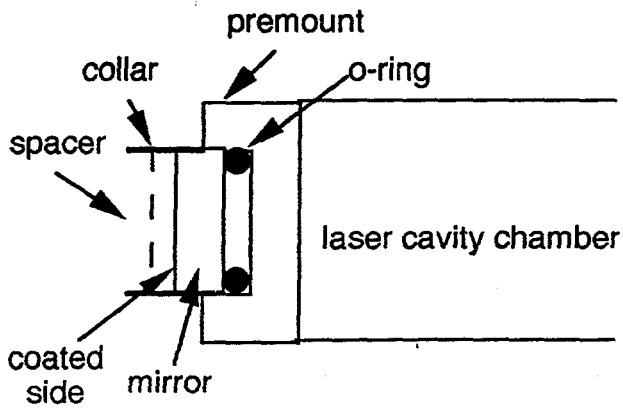

Figure D.1 Mounting of end mirrors in excimer laser.

(4) Repeat step (1), flushing and filling cavity with inert gas three times. Leave cavity in evacuated state (30 mbar) in preparation for next step, passivation fill.

D.3 Passivation Fill:

After the cavity has been opened to air, it must be passivated. If the laser has been unused for some time, or moved, this step is necessary as well.

(1) Starting at 30 mbar, add 200 mbar of halogen gas by pressing [HALOGEN] then [LASER HEAD]. Again, the halogen valve will remain open only 10 seconds, so it may have to be toggled more than once.

(2) Add enough inert gas (helium) to bring the laser head pressure up to 2000 mbar, again by pressing [INERT] and [LASER HEAD], toggling as many 10 second intervals as necessary.

(3) The passivation gas mixture can be held from 2 hours or overnight, depending upon how long the laser has been opened or not operated.

D.4 New Fill:

Begin with laser cavity evacuated to 30 mbar. Press [NEW FILL] and hit [ENTER] when XeCl Ne shows up on menu to check program. If gas fill amounts are not correct, the values in the following table should be entered. To begin new gas fill, press [EXE]cute when XeCl Ne is displayed in the controller register. The new fill will proceed automatically in the order HCl then Xe then Ne.

Table D.1 Partial pressure of gases used in XeCl excimer laser.

Gas	Partial Pressure
HCl	90 mbar
Xe	110 mbar
Ne	3100 mbar

D.5 Maintenance

To retain maximum lifetime, the following maintenance schedule is proposed:

(1) **New fill** should be done every three weeks of running time. If the laser will be unused for an extended period of time, a **passivation fill** is recommended. Any time the laser is moved, an **inert fill** is required, followed by a **passivation fill** in the new location.

(2) **Cleaning end mirrors** is recommended every three gas fills. Remember, do **not** use vacuum grease on the o-rings or anywhere else in the excimer laser.

(3) The **halogen filter** should be replaced every year.

(4) The halogen-containing gas should not be used indefinitely. HCl is very corrosive and unstable in the presence of atmospheric moisture. Any time the halogen bottle is removed or replaced, the halogen line should be flushed and filled several times with an inert gas. This is described in step (1) under "Installation of Excimer Laser" above. Also note that *refrigeration grade* copper tubing is used in the halogen gas line.

BIBLIOGRAPHY

BIBLIOGRAPHY

[Ari82] T. Arisawa, Y. Suzuki, Y. Maruyama, and K. Shiba, "Extraction of selectively ionized atomic isotopes from a laser-induced plasma," *J. Phys. D: Appl. Phys.*, Vol. 15, pp. 1955-1962, 1982.

[Atu93] S. N. Atutov, P. V. Kolinko, and A. M. Shalagin, "Separation of lithium isotopes by light-induced drift," *Laser Physics*, vol. 3, no. 4, 885-859, 1993.

[Bar85] N. C. Barford, *Experimental Measurements: Precision, Error and Truth*, John Wiley & Sons, New York, 1985.

[Bri85] W. B. Bridges, "Method and apparatus for separating isotopes using electrophoresis in a discharge," *U.S. Patent Number 4,545,878,* Oct. 8, 1985.

[Bri86] W. B. Bridges, "Method and apparatus for separating isotopes using electrophoresis in a discharge," *U. S. Patent Number 4,563,258*, Jan. 7, 1986.

[Bro59] S. Brown, *Basic Data of Plasma Physics*, reprinted by AIP Press, Woodbury, NY, 1959/1994.

[Bro95a] C.B. Brooks and M.L. Brake, "Lithium-Argon discharges in a multicusp-ECR microwave resonant cavity," submitted for publication to IEEE Transactions in Plasma Science.

[Bro95b] C.B. Brooks and M.L. Brake, "Two-dimensional imaging of optical emission in a multicusp ECR microwave resonant cavity," submitted for putblication to IEEE Transactions in Plasma Science special issue on Plasma Imaging.

[But95] S. J. Butler, H. H. Goss, W. P. Lapatovich, "Microwave power spectral density and its effects on exciting electrodeless high intensity discharge lamps," in *1995 IEEE International Conference on Plasma Science,* IEEE, Piscataway, NJ, 1995, pg. 186.

[Che65] F. F. Chen, "Electric Probes," in *Plasma Diagnostic Techniques*, R. M. Huddlestone and S. L. Leonard, ed., Academic Press, New York, pp. 113-200, 1965.

[Che84] F. F. Chen, *Plasma Physica and Controlled Fusion*, Plenum Press, New York, 1984.

[CRC81] R. C. Weast, Ed., *CRC Handbook of Chemistry and Physics*, Boca Raton, FL: CRC Press, Inc., 1981.

[Del93] *Deltagraph Pro 3 User's Guide*, DeltaPoint, Inc., Monterey, CA, 1993.

[Dru30] M. J. Druyvesteyn, "Low-Voltage Arc",*Z. Phys.*, vol. 64, pg. 781-798, 1930 (in German).

[Ged92] J. B. Geddes, *EEDF Measurements in an Argon ECR Plasma*, M.S. Thesis, University of Michigan, 1992.

[Gri64] H. R. Griem, *Plasma Spectroscopy*, McGraw-Hill , New York, 1964.

[Gro91] M. Grossman and T. Shepp, "Plasma isotope separation methods," *IEEE Transactions on Plasma Science*, vol. 19, no. 6, 1114-1122, 1991.

[Haz80] G. Hazak, Y. Gell, Y. Boneh, and S. Goshen, "Fast ion extraction in laser isotope separation," *J. Appl. Phys.*, vol. 51, no. 10, pp. 5207-5211, 1980.

[Hei88] J. E. Heidenreich III,J. R. Paraszczak, M. Moisan and G. Sauve, "Electron energy distributions in oxygen microwave plasmas," *J. Vac. Sci. Technol. B,* vol. 6, no. 1, pp. 288-292, 1988.

[Hop90] J. Hopwood, D. K. Reinhard, and J. Asmussen, "Charged particle densities and energy distributions in a multipolar electron cyclotron resonant plasma etching source," *J. Vac. Sci. Technol. A*, vol. 8, no. 4, pp. 2903-2912, 1990.

[Hut87] I. H. Hutchinson, *Principles of Plasma Diagnostics*, Cambrige University Press, Cambridge, 1987.

[Jia94] S. F. Jiang and G. J. Wang, "Development of ion sources for fusion research at SWIP," *Rev. Sci. Instrum.*, vol. 65, no. 4, pp. 1162-1164, 1994.

[Joh50] E. O. Johnson and L. Malter, "A floating double probe method for measurements in gas discharges," *Physical Review*, vol. 80, no. 1, pp. 58-68, 1950.

[Kar82] A. I. Karchevskii and E. P. Potanin, "Isotope separation in dc discharges," *Sov. J. Plasma Phys.*, vol. 8, no. 11, pg. 553, 1982.

[Lie95] M. A. Lieberman and A. J. Lichtenberg, *Principles of Plasma Discharges and Processing*, John Wiley & Sons, Inc., New York, 1995.

[Loc68] W. Lochte-Holtgreven, "Evaluation of plasma parameters," in *Plasma Diagnostics*, W. Lochte-Holtgreven, ed., North-Holland, Amsterdam, 1968. (reprinted by AIP Press, Woodbury, NY, pp. 1-65, 1995.)

[Mah89] L. Mahoney, *The Design and Testing of a Compact Electron Cyclotron Resonant Microwave-cavity Ion Source*, Master's Thesis, Michigan State University, 1989.

[Mah90] L. Mahoney and J. Asmussen, "A compact, resonant cavity, five centimeter, multicusp, ECR broad-beam ion source," *Rev. Sci. Instrum.*, vol. 61, no. 1, pp. 285- 287, 1990.

[Mak92] P. Mak, G. King, T. A. Grotjohn, and J. Asmussen, "Investigation of the influence of electromagnetic excitation on electron cyclotron resonance discharge properties," *J. Vac. Sci. Technol. A*, vol. 10, no. 4, pp. 1281-1287, 1992.

[Mar68] G. V. Marr, *Plasma Spectroscopy*, Elsevier Publishing Company, New York, 1968.

[McC93a] W. McColl, C. Brooks, and M. L. Brake, "Double Langmuir probe diagnostic of a resonant cavity microwave discharge," *J. Vac. Sci. Technol. A*, vol. 11, no. 4, pp. 1152-1155, 1993.

[McC93b] W. McColl, *Continuous Wave and Pulsed Microwave Resonant Cavity Produced Discharges*, Ph. D. dissertation, University of Michigan, 1993.

[Moi88] M. Moisan and M. R. Wertheimer, "Comparison of microwave and r.f. plasmas: fundamentals and applications," *Surface and Coatings Technology,* vol. 59, pp. 1-13, 1993.

[Moi92] M. Moisan and J. Pelletier, eds., *Microwave Excited Plasmas*, Elsevier Science Publishers, Amsterdam/New York, 1992.

[Mou85] C. Moutoulas, M. Moisan, L. Bertrand, J. Hubert, J. Lachambre, and A. Ricard, *Appl. Phys. Lett.*, vol. 46, no. 4, pg. 323, 1985.

[Off90] S. Offermanns, "Electrodeless high-pressure microwave discharges," *J. Appl. Phys.*, vol. 67, no. 1, pp. 115-123, 1991.

[Pas91] M. L. Passow, M. L. Brake, P. Lopwz, W. B. McColl, and T. E. Repetti, "Microwave resonant-cavity-produced air discharges," *IEEE Transactions on Plasma Science*, vol. 19, no. 2, 1991.

[Pea41] R. W. Pearse and A. G. Gaydon, *The Identification of Molecular Spectra*, Chapman and Hall, London, 1941.

[PPR94] *Plasma Probe Data Acquisition System* Manual, Plasma Physics Research Group, Dublin City University, Ireland, 1994.

[Rea80] J. Reader and C. H. Corliss, "Pt. 1: Wavelengths," in *Wavelengths and Transition Probabilities for Atoms and Atomic Ions*, U. S. Government Prining Office, Washington, D. C., 1980.

[Ric68] J. Richter, "Radiation of hot gases," in *Plasma Diagnostics*, W. Lochte-Holtgreven, ed., North-Holland, Amsterdam, 1968. (reprinted by AIP Press, Woodbury, NY, pp. 1-65, 1995.)

[Sch68] L. Schott, "Electrical Probes," in *Plasma Diagnostics*, W. Lochte-Holtgreven, ed., North-Holland, Amsterdam, 1968. (reprinted by AIP Press, Woodbury, NY, pp. 668-731, 1995.)

[Sri91] A. K. Srivastava, M. Dahimene, T. Grotjohn, and J. Asmussen, "Experimental characterization of a compact ECR ion source," *Rev. Sci. Instrum.*, vol. 63, no. 4, pp. 2556-2558, 1992.

[Sri94] A. K. Srivastava, F. C. Sze, and J. Asmussen, "Discharge characteristics of a 5 cm multipolar electron cyclotron resonance ion source," *Rev. Sci. Instrum.*, vol. 65, no. 5, pp. 1749-1751, 1994.

[Str93] C. K. Struckman and B. R. Kusse, "High-purity intense lithium-ion-beam sources using glow-discharge cleaning techniques," *J. Appl. Phys.*, vol. 74, no. 6, pp. 3658-3668, 1993.

[Suz94] T. Suzuki, K. Takahashi, M. Nomura, Y. Fujii, and M. Okomoto, "Contact ionization ion sources for ion cyclotron resonance separation," *Jpn. J. Appl. Phys.*, vol. 33, no. 7B, pp. 4247-4250, 1994.

[Swi69] J. D. Swift and M. J. R. Schwar, *Electrical Probes for Plasma Diagnostics*, Americal Elsevier, New York, 1969.

[Wad92] M. Wada, H. Tsuda, and M. Sasao, "Multicusp ion source for production of negative lithium ions," *Rev. Sci. Instrum.*, vol. 63, no. 4, pp. 2729-2731, 1992.

[Wie80] W. L. Wiese and G. A. Martin, "Pt. 2: Transition Probabilities," in *Wavelengths and Transition Probabilities for Atoms and Atomic Ions*, U. S. Government Printing Office, Washington, D. C., 1980.

[Win94] L. Windholtz and C. Umfer, "Measurement of the transition wavelengths of the lithium resonance lines," *Z. Phys. D*, vol. 29, pp. 121-123, 1994.

[Wut94] D. Wutte, M. Leitner, and H. P. Winter, "A 2.45-GHz electron cyclotron resonance multi-mA Li^+ ion gun for fusion plasma diagnostics," *Rev. Sci. Instrum.*, vol. 65, no. 4, pp. 1094-1096, 1994.

[Xiw92] Z. Xiwen, H. Guilong, M. Ganghua, and Y. Delin, "Laser isotope enrichment of lithium by magnetic deflection of a polarized atomic beam," *J. Phys. B*, vol. 25, pp. 3307-3314, 1992.

[Yam79] M. Yamashita and H. Kashiwagi, "Method for separation and enrichment of lithium isotopes by laser," *U. S. Patent Number 4,149,077*, April 10, 1979.

[Zha94] X. Zhang, Z. Wang, and L. Hu, "A neutral lithium beam source," *Rev. Sci. Instrum.*, vol. 65, no. 4, pp. 1231-1233, 1994.